SOLAR SAIL APPLICATIONS FOR MISSION DESIGN IN SUN-PLANET SYSTEMS FROM THE PERSPECTIVE OF THE CIRCULAR RESTRICTED THREE-BODY PROBLEM

A Thesis

Submitted to the Faculty

of

Purdue University

by

Rohan Sood

In Partial Fulfillment of the

Requirements for the Degree

of

Master of Science in Aeronautics and Astronautics

December 2012

Purdue University

West Lafayette, Indiana

To Nanaji & Naniji with love,
and to the Cottonian family.
"Overcome evil with good."

ACKNOWLEDGMENTS

As I stand here today, nothing would have been possible without the love and care of my family. You have always stood beside me and for that I will forever be grateful to you. I have been greatly inspired by your continuous hard work and I hope to emulate your work ethics. Though I am so far away, I can feel your presence as you were always there to support me in all my endeavors.

I would like to extend my utmost gratitude to Professor Kathleen C. Howell for her continuous guidance and belief in me. Interactions with her have always motivated me to work hard and achieve higher goals. Her time and effort devoted towards my work is highly commendable. Learning and working under her is a wonderful experience, and for that I consider myself very fortunate to have her not only as my advisor, but as my mentor. I have also had the opportunity to teach under her direct guidance-an invaluable experience. I have grown and developed under her supervision, and for that I wish to express my utmost gratitude.

I would like to express my sincere appreciation to Professor James M. Longuski and Professor Dengfeng Sun for serving as committee members and reviewing my thesis work. They have been wonderful help with their insightful discussions and views on various subject matters.

My research group at Purdue University has been great support for me. Every individual member, from past to present, has helped me to critically analyze a problem in one way or another. Their love and support, inside and outside the work environment, has always made me feel like part of another family, and for that I thank each and every one.

As I pave my way towards higher education, I will always remember the support and guidance of Professor John L. Crassidis and Professor Puneet Singla, who have both been of great motivation to me. I would also like to extend my sincere ap-

preciation to Mr. George S. Chander for his contribution towards my educational development. He always challenged me not only to work hard but also apply myself to the best of my ability.

I thank Purdue University, School of Aeronautics and Astronautics for funding my education. I am also grateful to NASA's Simulation and Graphics Branch at Johnson Space Center in Houston, Texas for providing financial support towards my education and research work at Purdue University under NASA Grant# NNX12AC08G.

TABLE OF CONTENTS

Page

LIST OF TABLES

LIST OF FIGURES

SYMBOLS

CR3BP	Circular Restricted Three-Body Problem
$\mathcal{N}$	number of bodies
P_i	ith primary in the CR3BP
m_i	mass of the ith primary in the CR3BP
I	Inertially fixed coordinate frame with destral, perpendicular set of unit vectors $\hat{X}, \hat{Y}, \hat{Z}$
R	Rotating coordinate frame with destral, perpendicular set of unit vectors $\hat{x}, \hat{y}, \hat{z}$
B	Barycenter
θ	Orientation angle of $\hat{x}$ with respect to $\hat{X}$
$\dot{\theta}$	Angular rate of $\hat{x}$ with respect to $\hat{X}$
$\vec{r}_i$	Position vector of ith body relative to the barycenter
$\vec{r}_{ij}$	Position vector of jth body relative to the ith body
l^*	Characteristic length
m^*	Characteristic mass
t^*	Characteristic time
$\tilde{G}$	Universal gravitational constant
N	Dimensional mean motion
n	Nondimemsional mean motion
μ	Nondimensional mass ratio
τ	Nondimensional time
$\vec{\rho}$	Nondimensional position vector of P_3 relative to the barycenter
$\vec{d}$	Nondimensional position vector of P_3 relative to P_1
$\vec{r}$	Nondimensional position vector of P_3 relative to P_2
x, y, z	Scalar position coordinates in terms of rotating unit vectors

t	Dimensional time
${}^{I}\vec{r}_i{}''$	Second derivative of position vector, r_i, relative to dimensional time, t evaluated as seen by an inertial observer, I
${}^{I}\ddot{\vec{\rho}}$	Second derivative of nondimensional position vector, ρ, relative to nondimensional time, τ evaluated as seen by an inertial observer, I
${}^{I}\vec{\omega}^{R}$	Nondimensional angular velocity of the rotating frame, R, with respect to the inertial frame, I
Ω^*	Pseudo-potential function
Ω_i^*	Partial of pseudo-potential function relative to the rotating coordinates
J^*	Constant of integration (Jacobi constant)
v	Magnitude of the relative velocity
L_i	ith Lagrangian point
γ_{L_i}	Distance of collinear Lagrange point, L_i, relative to the nearest primary
ξ, η, ζ	Variations relative to the Lagrangian points in x, y, z, respectively
Ω_{ij}^*	Second partial derivative of pseudo-potential function relative to the rotating coordinates
$\vec{x}$	Six-dimensional state vector
$\mathbf{A}$	System matrix
ω	Frequency associated with harmonic out-of-plane component, ζ
A_k, B_k	Interdependant constants of integration
λ_k	Eigenvalues of matrix $\mathbf{A}$ associated with the in-plane motion
$\vec{X}(\tau_0)$	Initial state vector
$\vec{X}(\tau_f)$	Final state vector
$\vec{X}^*(\tau_0)$	Converged initial state vector
$\vec{X}(\tau)$	Reference trajectory
$\vec{X}^*(\tau)$	Nearby converged trajecotry

ϕ	State transition matrix (STM)
$\vec{X}_i(\tau_{0_i})$	Multiple shooting reference initial state of ith arc
$\vec{X}_i(\tau_{f_i})$	Multiple shooting reference end state of ith arc
$SS-CR3BP$	Solar Sail Circular Restricted Three Body Problem
$\hat{n}$	Unit direction vector normal to the sail plane
$\hat{d}$	Unit direction vector along the Sun-sail line
$\hat{k}$	Reference unit direction vector
ϵ	Sail efficiency
a_{sail}	Sail acceleration due to solar radiation pressure (SRP)
a^*	Solar sail characteristic acceleration
σ	Sail load factor
σ^*	Characteristic mass-to-area ratio
α, γ	Sail orientation angles
$\hat{n}$	Unit direction vector parallel to the surface of the sail
$\vec{F}_{Sail}$	Total net force acting on sail due to SRP
$\vec{F}_I$	Force on sail due to incident photons
$\vec{F}_R$	Force on sail as a result of reflected photons
P_{sail}	Total solar radiation pressure
β	Sail lightness parameter
a_{Sail-i}	Components of solar sail acceleration in the rotating coordinate frame along the ith unit direction vector
a_{Sail-i_j}	Partial of solar sail acceleration component along the ith unit direction vector relative to the jth position coordinate
$\mathbf{A}_{Aug}$	Augmented system matrix as a result of inclusion of sail in the CR3BP

ABSTRACT

Sood, Rohan M.S.A.A., Purdue University, December 2012. Solar Sail Applications for Mission Design in Sun-Planet Systems from the Perspective of the Circular Restricted Three-Body Problem. Major Professor: Kathleen C. Howell.

As a consequence of the successful harnessing of solar radiation pressure demonstrated by JAXA's IKAROS mission, the interest and developments in the field of solar sails has gained a significant momentum. Sail-based spacecraft potentially offer indefinite maneuvering capability by exploiting photons from the Sun as a means of propulsion. Incorporating a solar sail model within the context of the circular restricted three-body problem extends trajectory design options. In the last few decades, the Lagrangian points, L_i, as defined in the restricted problem, have increasingly become a focus for scientific spacecraft mission applications. In this investigation, a hybrid model that incorporates a solar sail force into the circular restricted three-body problem (SS-CR3BP) is developed. As a result of the additional force, the displaced locations of artificial collinear Lagrangian points are determined and exploited for trajectory design. In fact, various trajectories are constructed that employ only sail orientation angles to move through this dynamical regime. In particular, periodic orbits are computed in the vicinity of the displaced artificial L_1 equilibrium point, located between the Sun and the Earth in this Sun-planet system. A sample offset periodic orbit is demonstrated that hovers over the displaced L_1 point. Trajectory modifications are performed in the vicinity of the L_1 equilibrium point using solar sail angles. Three-dimensional transfers between halos at three different sizes is also constructed to exhibit the capabilities of solar sails based on specific mission objectives. Thus, in this investigation, solar sail capabilities that widen the design space for mission design in the restricted three-body problem are explored.

1. INTRODUCTION

The interest in space exploration and the desire for a comprehensive analysis of objects moving through regions of space beyond the Earth has resulted in a long-term scientific effort to better understand the behavior of stars and planets as well as their mutual interactions. Technological advancements offer the opportunity to expand the number of worlds to be visited and the number of targets per mission. But new technology also offers alternative exploration strategies and mission scenarios to explore a wider range of bodies. The asteroid mission OSIRIS-RE$_x$ (to be launched in 2016), designed to examine and return a sample from asteroid 1999 RQ$_{36}$, exemplifies the shift to a broader focus. Consistent with the interest in alternative concepts, solar sails continue to intrigue scientists and engineers. Solar sails offer both unique opportunities as well as challenges.

Solar sails offer spacecraft maneuvering capabilities within a dynamical environment by using photons from the Sun as a means of propulsion. The orientation of the sail is adjusted to support a wide variety of activities. For example, sails can be employed to modify trajectories to enter new orbits, find new periodic orbits, as well as more general trajectory design. Based on a specific orientation, the pressure from the photons delivers a small but continuous acceleration to the sail and, thus, opens dynamical regimes that typically lie beyond the natural dynamical flow or may require significant propellant. The focus of this investigation is the solar radiation pressure acting on a solar sail that expands the dynamical boundaries leading to new new orbits that are significant from certain mission design perspectives.

1.1 Problem Definition

The classical three-body problem provides a dynamical framework to investigate and explore a wide range of space. Thus, a precise definition allows the development of an appropriate model.

1.1.1 The Circular Restricted Three-Body Problem

The $\mathcal{N}$-body problem was first studied by Sir Issac Newton in the 17th century [1]. Limiting the number of bodies to two ($\mathcal{N} = 2$) leads to an understanding of the relative behavior of one body under the gravitational influence of another body. To model the solar system, one body is frequently much larger than the other body. Thus, a complete model represented in terms of the equations of motion, yields a well known conic solution that is solvable analytically. To increase the complexity of the problem and better model the gravitational influence of additional bodies, the number of interacting bodies is increased to three, $\mathcal{N} = 3$. With additional assumptions, this resultant model is termed the Circular Restricted Three-Body Problem (CR3BP). The simplified CR3BP model still does not possess an analytical solution.

1.1.2 Lagrangian Point and Periodic Orbits

The differential equations in the CR3BP do admit five equilibrium solutions. The equilibrium solutions were first investigated in 1772 by Joseph-Louis Lagrange and, hence, are denoted the Lagrangian Points. Three of the Lagrangian points are collinear, i.e., they lie along the line connecting the two primary bodies. The remaining two Lagrangian points form equilateral triangles with the two primaries within the primary plane of the motion. The existence of the Lagrangian points offers an opportunity to explore the regions in the vicinity of a set of constant solutions.

Planar and three-dimensional periodic orbits are known to exist in the vicinity of Lagrangian points [2]. One such three-dimensional family of orbits have been of

particular interest and is identified as the 'halo' orbit family [3]. The Sun-Earth Lagrangian points, L_i, are significant from a mission design perspective. Thus, further examination of orbits in the vicinity of the collinear Lagrangian points will aid understanding of the dynamical region and create additional options for future scientific missions.

1.1.3 Solar Sails in Circular Restricted Three-Body Problem

The inclusion of solar sails expands the dynamical structures in the classical circular restricted three-body problem. The force due to Solar Radiation Pressure (SRP) modifies the dynamical force model, and, thus, the locations of the equilibrium points as well as the trajectories are governed by the new dynamical environment. Powered by the continuous flow of photons from the Sun, solar sails provide additional acceleration capabilities to the spacecraft. Thus, solar sails are equipped with the capability of a continuous thrusting force, a force that would otherwise require propellant. Though the level of the force is small, a continuous flow applied over a long duration can enable velocities beyond the capabilities of conventional propulsive systems. Recent studies from Cosmos-1 and Sun-Diver have projected velocities as high as $\approx$50 km/s [4].

The use of SRP can be extended to add maneuvering capabilities to a spacecraft, for example, trajectory design and new periodic orbits in the vicinity of an artificial equilibrium point. Such applications of a solar sail could decrease the reliability on conventional maneuvers requiring propellant but also potentially offer a nearly infinite maneuvering capability to the spacecraft. Thus, this investigation further explores such capabilities to exploit the Sun as a source of continuous propulsion with the aid of a solar sail based spacecraft.

1.2 Prior Contribution

History bears testimony to human curiosity that previously led to the investigation of planetary motion. From understanding the origins of solar system to a search for the origins of life, the exploration of space has forever offered intriguing problems.

1.2.1 Classical Circular Restricted Three-Body Problem

The formulation of the three-body problem dates back to Newton in the 17th century [1]. But later, in 1772, Euler introduced a rotating frame to the restricted three-body problem and, simultaneously, Lagrange derived an analytical solution that led to the identification of the equilibrium points [5]. Approximately half a century later, Carl Gustav Jacobi recognized a constant of integration associated with the rotating frame formulation [6]. The constant was later renamed and is now commonly labeled as the Jacobi constant.

In 1897, Heinrich Bruns proved the non-existence of any other constant of motion in the three-body problem. Two years later, Jules Henri Poincaré also proved the lack of a non-algebraic constant of motion, i.e., the restricted three-body problem problem is non-integrable [5]. Poincaré also confirmed the existence of periodic solutions in the restricted three-body problem. Research efforts in the three-body problem slowed for over half a century until Victor G. Szebehely thoroughly detailed the derivation and particular solutions in the restricted three-body problem in his book *Theory of Orbits: The Restricted Problem in the Three Bodies* [5]. The last 50 years have witnessed technological advancements that have, once again, spurred new research efforts in the CR3BP.

1.2.2 Motion in the Vicinity of the Collinear Lagrangian Points

The dynamical region in the vicinity of the collinear Lagrangian points has been a topic of interest from various scientific mission prospectives. In 1980, David L.

Richardson presented an approximation for periodic orbits in the Sun-Earth circular restricted problem near the collinear Lagrangian points [7]. In 1982, Kathleen C. Howell, in collaboration with John V. Breakwell, used continuation based on a numerical technique to generate periodic orbits, i.e., halo orbits, that lie beyond the computational capabilities of any analytical approximations [8]. Howell and Breakwell supplied some foundations and demonstrated the existence of stable periodic orbits in the vicinity of the Lagrangian points [9].

The collinear Lagrangian point, L_1, proves to be of particular significance in the investigation of the effects of solar winds and solar flare emissions from the Sun. In 1978, the International Sun-Earth Explorer-3 (ISEE-3) was a joint mission planned by NASA and ESA and was first placed in a halo orbit about the Sun-Earth Lagrangian point, L_1 [10]. The success of ISEE-3 motivated the scientific community to further investigate the solar atmosphere, the solar winds and to study the structure of the Sun. Thus, in 1995, the Solar and Heliospheric Observatory was launched as a joint scientific project by NASA and ESA [11]. Today, it still relays a continuous beam of data for predicting space weather and monitoring solar activity. The Global Geospace Science WIND spacecraft was launched in 1994 and was also placed in a small halo orbit about the Sun-Earth L_1 point. The objective of the WIND mission is to observe unperturbed solar winds and provide scientific data to better understand the Solar-Earth relationship [11], [12]. In 1997, NASA launched the Advanced Composition Explorer (ACE) spacecraft to collect solar and interplanetary particles [11]. The ACE spacecraft transmits important data and warning signs of upcoming solar storms daily to Jet Propulsion Laboratory's Deep Space Network.

1.2.3 Study of Solar Radiation Pressure

The history of scientific and engineering inquiry involving solar radiation pressure dates back to 1873 when James Clerk Maxwell theoretically proved the existence of pressure due to radiation [13]. The first laboratory experiment was conducted by

Peter Lebedew who, in 1900, experimentally demonstrated the existence and effects of solar radiation pressure [14]. The application of solar radiation pressure as a means of propulsion was ultimately proposed by Konstantin E. Tsiolkovsky and Fridrickh Tsanders in 1924 [15]. In the 1970's, when NASA developed an interest in solar sail technology, a serious focus emerged and laboratory experiments were initiated. Within the next four years, NASA's continuous research resulted in a successful lab-based demonstration in 1974 [16]. In the same year, NASA applied the use of solar radiation pressure to the Mariner 10 spacecraft that required attitude control but was low on fuel. The spacecraft solar arrays were turned to face the Sun and employed solar radiation pressure for attitude control. Though the spacecraft was not specifically designed as a sail-based spacecraft, the small but effective force due to solar radiation pressure was demonstrated. India's INSAT 2A and INSAT 3A communications satellites exploited a small solar sail to offset the torque resulting from solar radiation pressure on the solar array [17]. Within the last decade, NASA's collaboration with the Planetary Society has resulted in the active development of a NanoSail vehicle. LightSail-1 and LightSail-2 have been planned to test the solar radiation pressure within the low Earth orbit. Upon successful demonstration, LightSail-3 will be launched for insertion into an orbit in the vicinity of L_1 to enhance early detection of variations in space weather that may be capable of a significant influence on Earth [18]. The recent success of Japan's Interplanetary Kite-craft Accelerated by Radiation Of the Sun (IKAROS) has rejuvenated the ongoing quest for exploiting solar radiation as a source of propulsion. The spacecraft successfully demonstrated both a propulsive force as well as attitude control in July 2010 [19]. The IKAROS spacecraft is currently on its way to Venus.

1.3 Current Work

The core of this investigation is the construction of periodic orbits in the vicinity of artificial collinear Lagrangian points. Based on the characteristics associated with the

solar sail, the location of a Lagrangian point can be altered. Thus, both planar and three-dimensional periodic orbits are computed within the vicinity of the Lagrangian point, L_1. The solar sail orientation angles are used to remain in vicinity of the equilibrium point for an extended period of time. Offset orbits are also determined that hover near the artificial Lagrangian point L_1.

The analysis in this investigation is accomplished by incorporating the solar sail force model into the classical circular restricted three-body problem (CR3BP). Later, a solar sail force is added to represent a hybrid solar sail system in the circular restricted three-body (SS-CR3BP) model.

The investigation is organized into the following chapters:

Chapter 2.
BACKGROUND: THE THREE-BODY PROBLEM

The circular restricted three-body model is introduced and the equations of motions are derived. This model governs the motion of an infinitesimal particle under the gravitational influence of two larger bodies. Assumptions simplify the analysis and a rotating frame relative to an inertial frame is introduced. The equations of motion that are derived are nonlinear and coupled. Thus, the existence of an integral of motion acts as an important tool to compute boundaries, trajectories and orbits. Equilibrium solutions, also labeled Lagrangian points, are evaluated and further analysis is focused near the collinear equilibrium points. Linear behavior in the vicinity of the collinear Lagrangian points is explored. Initial conditions from the linear model are propagated and a linear periodic orbit about the collinear Lagrangian point, L_1 is determined. This linear periodic orbit seeds as an initial guess to compute the periodic orbit in the nonlinear model.

Chapter 3.
DIFFERENTIAL CORRECTIONS ALGORITHM FOR TRAJECTORY DESIGN

This chapter initiates the analysis into the evolution of the state vector over time in response to a change in the initial state. A differential corrections scheme is introduced to modify the design variables to meet certain constraints based on the information supplied by the state transition matrix. The targeting schemes are further employed to determine periodic orbits in the vicinity of the collinear Lagrangian points. A complete formulation is also detailed for the construction of three-dimensional halo orbits. Northern and southern halo families are computed and plotted for the Lagrangian point L_1 and L_2.

Chapter 4.
BACKGROUND: SOLAR SAILS

A brief background of solar radiation pressure and solar sails is summarized. Solar sail models in various developmental stages are discussed. JAXA's IKAROS mission is analyzed in depth and a formulation to model the acceleration due to solar radiation pressure is developed. Comparisons are completed between different sail models based on their size, efficiency and sail loading.

Chapter 5.
SOLAR SAIL IN THE CIRCULAR RESTRICTED THREE-BODY PROBLEM (SS-CR3BP)

A mathematical expression for the acceleration force due to solar radiation pressure as applied to a solar sail is derived. The expression for the acceleration force is then incorporated into the circular restricted three-body model, thus, the model evolves into the Solar Sail Circular Restricted Three-Body Problem (SS-CR3BP). The definitions and assumptions involved in this development are summarized. Displaced collinear Lagrangian points are constructed where their locations are based on a certain sail parameter. Behavior of a spacecraft in the vicinity of a displaced collinear

Lagrangian point is also discussed. Finally, a linear model for periodic orbits in the vicinity of displaced Lagrangian points is analyzed based on the sail characteristics and orientation angles.

Chapter 6.

DIFFERENTIAL CORRECTIONS FOR TRAJECTORY DESIGN EMPLOYING SAIL ANGLES

The SS-CR3BP model is further investigated to develop a corrections algorithm that employs the sail orientation angles as design variables. An augmented state transition matrix is formulated to analyze the variations in the final position and velocity states as a result of changes in the orientation angles. The corrections schemes introduced in Chapter 3 are modified to employ only the sail orientation angles leading to sail-based update schemes. A new targeting scheme is formulated to construct trajectories; the associated families of orbits are established in the vicinity of the Lagrangian points based on specific sail characteristics. Trajectories are designed using sail orientation angles to achieve and maintain desired trajectory based on mission specifications.

Chapter 7.

PERIODIC ORBITS AND TRAJECTORY DESIGN IN SS-CR3BP

The targeting schemes are further employed to determine periodic orbits in the vicinity of the artificial collinear Lagrangian point L_1. A linear model is employed as an initial guess. Sail orientation angles are iteratively corrected and a periodic solution is constructed. Sample trajectory designs incorporating solar sail angles are demonstrated. The y-amplitude adjustments are made to the trajectories in the vicinity of L_1 by varying the orientation angles. A three-dimensional trajectory is designed about L_1 that transfers between three orbits of different y- and z-amplitudes.

Chapter 8.

SUMMARY AND RECOMMENDATIONS

Concluding remarks summarize the results of the current investigation. Suggestions for potential future work are also offered.

2. BACKGROUND: THE THREE-BODY PROBLEM

Preliminary knowledge and understanding of the basic principles governing the motion of a particle in the gravitational environment of multiple bodies is critical to examination of the behavior of a spacecraft. The complexity associated with formulating a mathematical model to represent the $\mathcal{N}$-body problem [1] requires some simplifications to gain insight. Casting the problem within the context of the classical Circular Restricted Three-Body Problem (CR3BP) offers the essential features of the motion with some mathematical advantages [20]. To characterize this analysis, the CR3BP is formulated in detail. The governing differential equations are derived in a form that will later allow the inclusion of a solar sail force.

2.1 The Circular Restricted Three-Body Problem

To understand the interactions between an unspecified number of bodies, all moving under their mutual gravitational influence, the $\mathcal{N}$-body problem was first mathematically formulated by Sir Issac Newton in 1687 [1]. For $\mathcal{N}$ bodies coupled under mutual gravitational forces, any direct derivation of the equations of motion produces $6\mathcal{N}$ scalar differential equations. Due to the lack of available integrals of the motion, no closed-form analytical solution exists for the motion in the general $\mathcal{N}$-body problem. Thus, beginning in the 17^{th} century, many mathematicians investigated a wide variety of approaches to gain insight into the natural behavior. The earliest successes limited the number of particles and shifted the observer [21].

2.1.1 Assumptions

The general $\mathcal{N}$-Body Problem ($\mathcal{N}$-BP) is complex and an analytical solution is not available. Thus, some initial assumptions are useful. In an extension to more than two particles, a mathematical formulation of the $\mathcal{N}$-BP yields $6\mathcal{N}$ scalar differential equations. A solution for such a system requires $6\mathcal{N}$ scalar integrals of the motion. However, only 10 constants of the motion are available in the gravitational problem. In fact, for $\mathcal{N} > 3$, no analytical solution exists. Thus, beyond the conic problem, the introduction of even one more particle alters the character of the problem. Yet, consider the number of particles. If $\mathcal{N} = 2$, the required number of constants is 12. However, as is well known, if the two-Body Problem (2-BP) is recast in terms of a relative formulation, only six differential equations completely model the relative behavior and the problem is analytically solvable, i.e., the well known conic sections [22].

The lack of a closed-form solution in the $\mathcal{N}$-BP results in a first assumption to narrow the number of particles to three. Recall that, in the Three-Body Problem (3-BP), the derivation of a complete solution requires 18 first-order scalar differential equations to completely describe the motion of a single body relative to two other bodies. Due to the lack of integrals (only 10 are known), additional assumptions are incorporated to further simplify the problem and gain some insight into the nonintegrable behavior. The second assumption in the problem involves the masses. The third body P_3, of mass m_3, is assumed to be infinitesimal in comparison to the other two larger bodies. These are termed the two *primaries*, P_1 and P_2, and are of mass m_1 and m_2, respectively, such that $m_3 \ll m_1, m_2$. Thus, P_3 does not gravitationally influence the motion of P_1 and P_2; the orbits of P_1 and P_2 are completely Keplerian in nature and the relative motion is modeled as a two-body problem. If the relative motion of P_1 and P_2 is Keplerian, then the two primaries follow conic paths. Although it is not required, for simplicity, assume that the two primaries move on circular orbits about their common center of mass, that is, the barycenter, B. With

the assumptions, the number of first-order scalar differential equations that govern the relative behavior of the two primaries, P_1 and P_2, in the system is reduced from 18 to 6 and the two primaries move on conic paths. For simplicity, let the motion of the P_1 and P_2 be circular. Then, the motion of an *infinitesimal* mass, P_3, under the gravitational influence of the two larger primaries, P_1 and P_2, is investigated by studying the CR3BP.

2.1.2 Geometry Associated with CR3BP

An innovation in the analysis of the 3-BP, introduced by Euler, is the shift to a rotating view. Thus, to specify the orientation and position of the three bodies with respect to each other, two coordinate frames are defined. The first reference frame is the inertially-fixed coordinate frame, I, whose dextral, perpendicular set of unit vectors are defined as $\hat{X}, \hat{Y}, \hat{Z}$ as represented in Figure 2.1. Note that the caret ($\hat{}$)

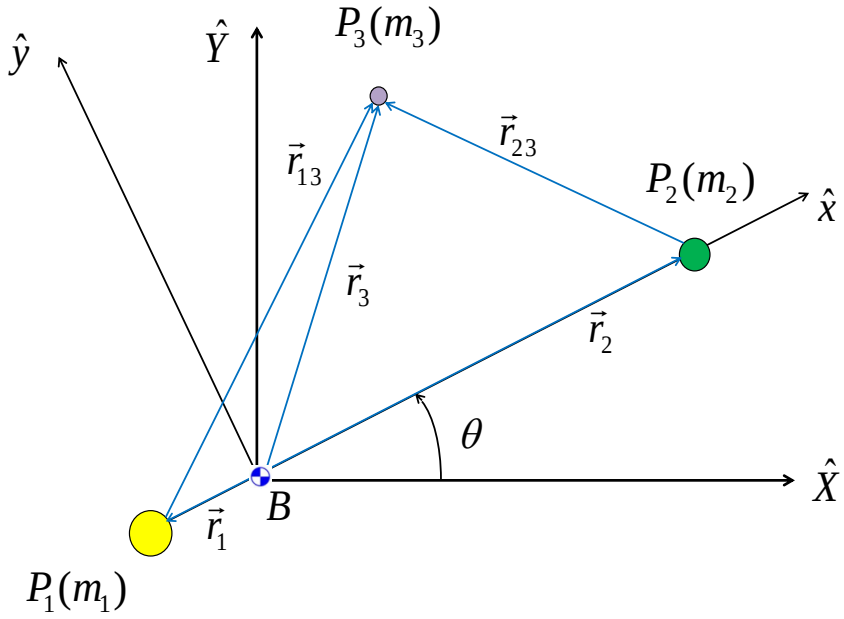

Figure 2.1. Geometrical Definitions in the Circular Restricted Three-Body Problem.

symbol represents a vector of unit magnitude. The $\hat{X} - \hat{Y}$ plane denotes the plane of motion of the two primaries and $\hat{Z}$ is directed parallel to the conic orbital angular

momentum vector; as noted previously, the primaries move on circular orbits relative to each other. A second coordinate frame, R, is rotating consistent with the orbital motion of the primaries. The dextral, orthogonal set of unit vectors associated with the rotating frame is denoted as $\hat{x}, \hat{y}, \hat{z}$ where $\hat{x}$ is always directed from P_1 to P_2.

A precise formulation of the problem requires specifying the relative orientation and position vectors within the context of the CR3BP. The center of mass of the two primaries is defined as the barycenter, B, as represented in Figure 2.1. The orientation of $\hat{x}$ with respect to $\hat{X}$ is defined by the angle θ; note that the reference for θ, i.e., $\theta = 0^\circ$ occurs when $\hat{x}$ and $\hat{X}$ are aligned. As the two primaries are moving along circular paths about the barycenter, the angular velocity, $\dot{\theta}$, remains constant. (Dots reflect derivatives with respect to time.) In addition, $\hat{z}$ is parallel to $\hat{Z}$, i.e., in the direction of primary orbital angular momentum. Then, $\hat{y}$ completes the right-handed triad. The position vectors corresponding to the locations of the three bodies, P_1, P_2 and P_3, relative to the barycenter, are defined as $\vec{r}_1$, $\vec{r}_2$ and $\vec{r}_3$ whereas $\vec{r}_{13}$ and $\vec{r}_{23}$ define the position vector of P_3 relative to P_1 and P_2, respectively, as represented in Figure 2.1. Note that the arrow ($\rightarrow$) over a symbol denotes a vector and, without an arrow, the symbol reflects a scalar magnitude. The geometrical definitions assist in formulating the problem and deriving the equations of motion.

2.1.3 Nondimensional Quantities

Characteristic quantities are defined to generalize the governing differential equations through nondimensionalization. To avoid round-off errors associated with the numerical integration process and to generalize the results, characteristic mass, length, and time quantities are specified. Let the distance between the two primaries be defined as the characteristic length, l^*, such that

$$l^* = r_1 + r_2 \tag{2.1}$$

where r_i is the distance between the system barycenter and the two primaries, P_1 and P_2, respectively. Due to the assumption of circular orbits for the motion of the two

primaries, l^* is the sum of the semi-major axis of P_2 relative to P_1 and is constant. Characteristic mass, m^*, is defined as the sum of masses of the two primaries such that

$$m^* = m_1 + m_2 \tag{2.2}$$

Characteristic length and mass in Equations (2.1) and (2.2) also yield the characteristic time, t^*. Characteristic time, t^*, is defined such that the nondimensional gravitational constant, G, is equal to a value of one, i.e.,

$$t^* = \sqrt{\frac{l^{*3}}{\tilde{G}\, m^*}} \tag{2.3}$$

where $\tilde{G}$ is the dimensional universal gravitational constant. The dimensional mean motion, N, of the system is expressed as

$$N = \sqrt{\frac{\tilde{G}\, m^*}{l^{*3}}} \tag{2.4}$$

Based on these characteristic definitions, other quantities of interest are now easily deduced in nondimensional form. The nondimensional mean motion, n, reduces as follows

$$n = N\, t^* = \sqrt{\frac{\tilde{G}\, m^*}{l^{*3}}}\, \sqrt{\frac{l^{*3}}{\tilde{G}\, m^*}} = 1 \tag{2.5}$$

Nondimentional mass ratio, μ, is introduced such that

$$\mu = \frac{m_2}{m^*} \tag{2.6}$$

Now, the nondimensional masses of the two primaries, based on μ, are

$$\frac{m_1}{m^*} = 1 - \mu \tag{2.7}$$

$$\frac{m_2}{m^*} = \mu \tag{2.8}$$

Nondimentional time and relative position vectors are then expressed in the form

$$\tau = \frac{t}{t^*} \tag{2.9}$$

$$\vec{\rho} = \frac{\vec{r}_3}{l^*} = x\hat{x} + y\hat{y} + z\hat{z} \tag{2.10}$$

$$\vec{d} = \frac{\vec{r}_{13}}{l^*} = (x+\mu)\hat{x} + y\hat{y} + z\hat{z} \tag{2.11}$$

$$\vec{r} = \frac{\vec{r}_{23}}{l^*} = (x-1+\mu)\hat{x} + y\hat{y} + z\hat{z} \tag{2.12}$$

where $\vec{\rho}$, $\vec{d}$, $\vec{r}$ represent the nondimensional position vectors of P_3 relative to the barycenter, P_1 and P_2, respectively. Note that the position vectors are expressed in coordinates defined in terms of rotating unit vectors. The expressions in Equations (2.9) - (2.12) assist in formulating the differential equation and deriving a mathematical model for the motion of P_3.

2.1.4 Derivation of Equations of Motion in CR3BP

The total force acting on the infinitesimal particle, P_3, is evaluated using Newton's Law of Gravity. Based on the geometry in the CR3BP appearing in Figure 2.1, the vector differential equation governing the motion of P_3 under the gravitational influence of P_1 and P_2 is

$$m_3 {}^I\vec{r}_3{}'' = -\frac{\tilde{G}m_3m_1}{r_{13}^3}\vec{r}_{13} - \frac{\tilde{G}m_3m_2}{r_{23}^3}\vec{r}_{23} \tag{2.13}$$

Note that the superscript I denotes that the derivative of the position vector is evaluated as seen by an inertial observer. The prime symbol ($'$) represents the derivative with respect to dimensional time, t. Based on the characteristic quantities, Equation (2.13) can be rewritten in a nondimensional form as

$${}^I\ddot{\vec{\rho}} = -\frac{(1-\mu)}{d^3}\vec{d} - \frac{\mu}{r^3}\vec{r} \tag{2.14}$$

Note that the derivatives in Equation (2.14) are with respect to nondimensional time, τ. Thus, the dot symbol ($\dot{}$) represents the derivative with respect to nondimensional time, τ. Since $\vec{\rho}$ is expressed in terms of rotating coordinates, a kinematic expansion is

employed to develop the derivatives of $\vec{\rho}$. Evaluating $\vec{\rho}$ and its subsequent derivatives with respect to an inertial observer is based on the following expressions

$$ {}^{I}\dot{\vec{\rho}} = \frac{{}^{I}d\vec{\rho}}{dt} = \frac{{}^{R}d\vec{\rho}}{dt} + {}^{I}\vec{\omega}^{R} \times \vec{\rho} \tag{2.15} $$

where ${}^{I}\vec{\omega}^{R}$ is the nondimensional angular velocity of the rotating frame with respect to the inertial frame. Since the primary motion is circular, the angular velocity vector possesses a magnitude equal to unity, that is,

$$ {}^{I}\vec{\omega}^{R} = \dot{\theta}\hat{z} = n\hat{z} = (1)\hat{z} \tag{2.16} $$

Recall that the mean motion, n, equals the constant angular velocity for primary motion in circular orbits. The second derivative of $\vec{\rho}$ is deduced from the expression for ${}^{I}\ddot{\vec{\rho}}$ such that

$$ {}^{I}\ddot{\vec{\rho}} = \frac{{}^{I}d{}^{I}\dot{\vec{\rho}}}{dt} = \frac{{}^{R}d{}^{I}\dot{\vec{\rho}}}{dt} + {}^{I}\vec{\omega}^{R} \times \dot{\vec{\rho}} \tag{2.17} $$

The derivative from Equation (2.17) is then substituted for the left side of Equation (2.14) and results in the following kinematic expression.

$$ {}^{I}\ddot{\vec{\rho}} = (\ddot{x} - 2\dot{y} - x)\hat{x} + (\ddot{y} + 2\dot{x} - y)\hat{y} + \ddot{z}\hat{z} \tag{2.18} $$

Substituting the kinematic expression from Equation (2.18), along with nondimensional position vectors $\vec{r}$ and $\vec{d}$, into Equation (2.14) yields the following three second-order nondimensional scalar equations of motion for P_3 under the gravitational influence of two primaries, P_1 and P_2

$$ \ddot{x} - 2\dot{y} - x = -\frac{(1-\mu)(x+\mu)}{d^3} - \frac{\mu(x-1+\mu)}{r^3} \tag{2.19} $$

$$ \ddot{y} + 2\dot{x} - y = -\frac{(1-\mu)y}{d^3} - \frac{\mu y}{r^3} \tag{2.20} $$

$$ \ddot{z} = -\frac{(1-\mu)z}{d^3} - \frac{\mu z}{r^3} \tag{2.21} $$

Equations (2.19) - (2.21) are reduced to six first-order scalar differential equations. A more condensed formulation is available based on the gravitational potential function associated with a conservative system. Since the differential equations are written in

terms of the rotating frame, a suitable potential function augments the gravitational potential. This pseudo-potential function, Ω^*, is defined as

$$\Omega^* = \frac{1-\mu}{d} + \frac{\mu}{r} + \frac{1}{2}(x^2 + y^2) \tag{2.22}$$

Note that the pseudo-potential function is not an explicit function of time. The partials of the pseudo-potential, Ω_i^*, with respect to the rotating coordinates are evaluated as

$$\Omega_x^* = x - \frac{(1-\mu)(x+\mu)}{d^3} - \frac{\mu(x-1+\mu)}{r^3} \tag{2.23}$$

$$\Omega_y^* = y - \frac{(1-\mu)y}{d^3} - \frac{\mu y}{r^3} \tag{2.24}$$

$$\Omega_z^* = -\frac{(1-\mu)z}{d^3} - \frac{\mu z}{r^3} \tag{2.25}$$

A condensed form of the differential equations of motion, Equations (2.19)-(2.21), are derived based on these partials, that is,

$$\ddot{x} = 2\dot{y} + \Omega_x^* \tag{2.26}$$

$$\ddot{y} = -2\dot{x} + \Omega_y^* \tag{2.27}$$

$$\ddot{z} = \Omega_z^* \tag{2.28}$$

Equations (2.26) - (2.28) represent the mathematical model that governs the motion of P_3. The nonlinear and coupled nature of these differential equations increases the complexity associated with the behavior. Thus, insight into the motion is sought through a constant of motion associated with the differential equations, if one exists.

2.1.5 Integral of Motion in CR3BP

To gain further insight, a search for an integral of the motion originates with Equations (2.19) - (2.21). The nonlinear and coupled nature of the Equations (2.19) - (2.21) does not allow a closed-form solution. However, the forces acting within the system are conservative, thus, there is a possibility that an energy-like quantity is

constant. To expose such an integral, Equations (2.19) - (2.21) are multiplied by $\dot{x}$, $\dot{y}$ and $\dot{z}$, respectively. The summation of these three equations reduces to

$$\dot{x}\ddot{x} + \dot{y}\ddot{y} + \dot{z}\ddot{z} = \Omega^*_x\dot{x} + \Omega^*_y\dot{y} + \Omega^*_z\dot{z} \tag{2.29}$$

$$= \frac{\partial\Omega^*}{\partial x}\frac{dx}{d\tau} + \frac{\partial\Omega^*}{\partial y}\frac{dy}{d\tau} + \frac{\partial\Omega^*}{\partial z}\frac{dz}{d\tau} \tag{2.30}$$

Recall that τ represents the nondimensional time and Ω^* is a function of nondimensional mass and the position coordinates only. The right side of Equation (2.30) represents the total time derivative of the pseudo-potential function

$$\frac{\partial\Omega^*}{\partial x}\frac{dx}{d\tau} + \frac{\partial\Omega^*}{\partial y}\frac{dy}{d\tau} + \frac{\partial\Omega^*}{\partial z}\frac{dz}{d\tau} = \frac{d\Omega^*}{d\tau} \tag{2.31}$$

Integrating both sides of Equation (2.31) by nondimensional time, τ, results in

$$\frac{1}{2}(\dot{x}^2 + \dot{y}^2 + \dot{z}^2) = \Omega^* - \frac{J^*}{2} \tag{2.32}$$

where J^* is the constant of integration. The constant of integration, J^*, is labeled as the Jacobi constant, named after Carl Gustav Jacobi [6]. In Equation (2.32), the magnitude of the relative velocity, that is, v, appears and simplifies the expression to the form

$$v^2 = 2\Omega^* - J^* \tag{2.33}$$

Further substituting for Ω^*, Equation (2.33) is easily rewritten as

$$J^* = 2\Omega^* - v^2 \tag{2.34}$$

$$= (x^2 + y^2) + 2(\frac{(1-\mu)}{d} + \frac{\mu}{r}) - v^2 \tag{2.35}$$

Analysis employing the Jacobi constant is an effective approach to compute boundaries, orbits, trajectories and some transfers. It is also very useful to maintain accuracy in the numerical integration process. However, the addition of other external forces may eliminate this constant.

2.2 Analysis of the Equilibrium Solutions

Within the context of the CR3BP, five particular solutions exist for the equations of motion represented by Equations (2.26) - (2.28) in the rotating frame [23].

These equilibrium solutions, also termed the libration or Lagrangian points, were first recognized by Joseph-Louis Lagrange in 1772 while investigating the *three*-body problem [5].

2.2.1 Equilibrium Points in the CR3BP

To locate any equilibrium points, the velocity and acceleration relative to the rotating frame must be zero. Thus, the first and second derivatives of the position coordinates corresponding to the equilibrium points are zero. Equations (2.26) - (2.28) are evaluated for these conditions

$$\Omega_x^* = \Omega_y^* = \Omega_z^* = 0 \tag{2.36}$$

Substituting the result from Equation (2.36) into Equations (2.23) - (2.25) results in the following three algebraic relationships

$$0 = x_{L_i} - \frac{(1-\mu)(x_{L_i}+\mu)}{d_{L_i}^3} - \frac{\mu(x_{L_i}-1+\mu)}{r_{L_i}^3} \tag{2.37}$$

$$0 = y_{L_i} - \frac{(1-\mu)y_{L_i}}{d_{L_i}^3} - \frac{\mu y_{L_i}}{r_{L_i}^3} \tag{2.38}$$

$$0 = \frac{(1-\mu)z_{L_i}}{d_{L_i}^3} - \frac{\mu z_{L_i}}{r_{L_i}^3} \tag{2.39}$$

where x_{L_i}, y_{L_i}, z_{L_i}, along with d_{L_i} and r_{L_i}, are the coordinates and relative distances of P_3 in the rotating frame with respect to B, P_1, and P_2 respectively. For Equation (2.39) to be satisfied, z_{L_i} must be equal to zero. Thus, the Lagrangian points lie in the xy plane. Apparent from Equation (2.38), certain equilibrium solutions exist for $y = 0$. Thus, equilibrium solutions exist along the line connecting the two primaries. These equilibrium points are termed the collinear Lagrangian points. Solving Equation (2.37) for the locations of the collinear points is nontrivial. The degree of the polynomial in Equation (2.37) suggests that there are three roots to the equation, i.e., three collinear points exist. The relative position of the Lagrangian points are

represented in Figure 2.2 and, thus, the coordinates of the Lagrangian points are redefined relative to the nearest primary as

$$x_{L_1} = d_2 - \gamma_{L_1} \tag{2.40}$$

$$x_{L_2} = d_2 + \gamma_{L_2} \tag{2.41}$$

$$x_{L_3} = -d_1 - \gamma_{L_3} \tag{2.42}$$

such that d_1 and d_2 are the nondimensional distances of P_1 and P_2, respectively, relative to the barycenter, B. First, consider equilibrium points in the vicinity of the smaller primary, P_2. Then, Equation (2.37) is written as a function of γ_{L_i}

$$f(\gamma_{L_i}) = 0 = (d_i + \gamma_{L_i}) - \frac{(1-\mu)((d_i + \gamma_{L_i}) + \mu)}{d_{L_i}^3} - \frac{\mu((d_i + \gamma_{L_i}) - 1 + \mu)}{r_{L_i}^3} \tag{2.43}$$

where $d_i = d_2$ and $\gamma_{L_i} = -\gamma_{L_1}, \gamma_{L_2}$ respectively, when solving for γ_{L_1} and γ_{L_2}. When the solution for γ_{L_3} is being computed, $d_i = -d_1$ and $\gamma_{L_i} = -\gamma_{L_3}$. For an equilibrium solution in the vicinity of the larger primary, P_1, define L_i as L_3 such that γ_{L_3} is computed; then $d_i = -d_1$ and $\gamma_{L_i} = -\gamma_{L_3}$. Equation (2.43) is then solved iteratively using Newton's Method

$$\gamma_{L_i}^{j+1} = \gamma_{L_i}^{j} - \frac{f(\gamma_{L_i}^{j})}{f'(\gamma_{L_i}^{j})} \tag{2.44}$$

This iteration process is continued until the desired accuracy in $|\gamma_{L_i}^{j+1} - \gamma_{L_i}^{j}|$ is achieved and, for this analysis, the tolerance is of order 10^{-12}. The remaining two noncollinear Lagrangian points, termed the equilateral points, are apparent via observations of Equation (2.38). These final two Lagrangian points form equilateral triangles with the two primaries at two vertices of a triangle and the third vertex of the triangle reflects the location of the Lagrangian point. By convention, Lagrangian point L_4 has a positive y coordinate, and L_5 is located with a negative y coordinate in the $x - y$ plane. The x and y coordinates of $L_{4,5}$ expressed relative to the barycenter, B are then

$$x_{L_{4,5}} = \frac{1}{2} - \mu \tag{2.45}$$

$$y_{L_{4,5}} = \pm \frac{\sqrt{3}}{2} \tag{2.46}$$

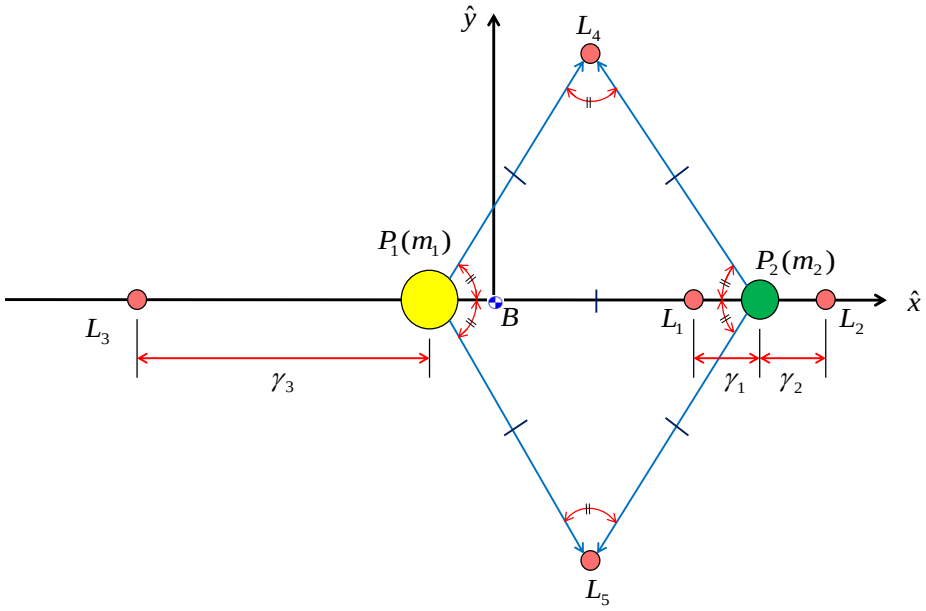

Figure 2.2. Lagrangian Points in the Circular Restricted Three-Body Problem.

The relative locations of all five Lagrangian points for a given system appears in Figure 2.2. These Lagrangian points are the only known equilibrium solutions to the equations of motion.

2.2.2 Behavior in the Vicinity of the Collinear Lagrangian Points

To further the investigation of the behavior of P_3, the stability information corresponding to the equilibrium points is investigated [24]. Since the differential equations are nonlinear, linear stability analysis in the vicinity of the equilibrium points is based on the first-order variational equations. Approximate solutions are generated by linearizing the equations of motion for P_3 relative to the Lagrangian points. The equations of motion represented in Equations (2.26) - (2.28) are used to derive the

linear variational equations relative to the equilibrium solutions. Given equilibrium solutions, perturbations are introduced such that

$$x = x_{L_i} + \xi \tag{2.47}$$

$$y = y_{L_i} + \eta \tag{2.48}$$

$$x = x_{L_i} + \zeta \tag{2.49}$$

where ξ, η, ζ are variations relative to the Lagrangian points in x, y, and z respectively. The equations of motion are rewritten, incorporating the perturbations, using a Taylor series expansion, and neglecting second- and higher-order terms. The resulting second-order, scalar, linear variational equations are

$$\ddot{\xi} - 2\dot{\eta} = \Omega^*_{xx}\xi + \Omega^*_{xy}\eta + \Omega^*_{xz}\zeta \tag{2.50}$$

$$\ddot{\eta} + 2\dot{\xi} = \Omega^*_{yx}\xi + \Omega^*_{yy}\eta + \Omega^*_{yz}\zeta \tag{2.51}$$

$$\ddot{\zeta} = \Omega^*_{zx}\xi + \Omega^*_{zy}\eta + \Omega^*_{zz}\zeta \tag{2.52}$$

where Ω^*_{ij} represents the second partial derivative of the pseudo-potential, that is,

$$\Omega^*_{xx} = 1 - \frac{(1-\mu)}{d^3} - \frac{\mu}{r^3} + \frac{3(1-\mu)(x+\mu)^2}{d^5} + \frac{3\mu(x-1+\mu)^2}{r^5} \tag{2.53}$$

$$\Omega^*_{yy} = 1 - \frac{(1-\mu)}{d^3} - \frac{\mu}{r^3} + \frac{3(1-\mu)y^2}{d^5} + \frac{3\mu y^2}{r^5} \tag{2.54}$$

$$\Omega^*_{zz} = 1 - \frac{(1-\mu)}{d^3} - \frac{\mu}{r^3} + \frac{3(1-\mu)z^2}{d^5} + \frac{3\mu z^2}{r^5} \tag{2.55}$$

$$\Omega^*_{xy} = \frac{3(1-\mu)(x+\mu)y}{d^5} + \frac{3\mu(x-1+\mu)y}{r^5} \tag{2.56}$$

$$\Omega^*_{xz} = \frac{3(1-\mu)(x+\mu)z}{d^5} + \frac{3\mu(x-1+\mu)z}{r^5} \tag{2.57}$$

$$\Omega^*_{yz} = \frac{3(1-\mu)yz}{d^5} + \frac{3\mu yz}{r^5} \tag{2.58}$$

$$\Omega^*_{yx} = \Omega^*_{xy} \tag{2.59}$$

$$\Omega^*_{zx} = \Omega^*_{xz} \tag{2.60}$$

$$\Omega^*_{zy} = \Omega^*_{xy} \tag{2.61}$$

For convenience, the differential equations are rewritten in the state-space form. Let the states be collected in the six-dimensional state vector, $\vec{x}$, such that

$$\vec{x} = \begin{bmatrix} \xi & \eta & \zeta & \dot{\xi} & \dot{\eta} & \dot{\zeta} \end{bmatrix}^T \tag{2.62}$$

Then, in matrix form, Equations (2.50) - (2.52) are rewritten as

$$\begin{Bmatrix} \dot{\xi} \\ \dot{\eta} \\ \dot{\zeta} \\ \ddot{\xi} \\ \ddot{\eta} \\ \ddot{\zeta} \end{Bmatrix} = \begin{bmatrix} \mathbf{N_3} & \mathbf{I_3} \\ \mathbf{\Omega^*_{i,j}} & \mathbf{D} \end{bmatrix} \times \begin{Bmatrix} \xi \\ \eta \\ \zeta \\ \dot{\xi} \\ \dot{\eta} \\ \dot{\zeta} \end{Bmatrix} \tag{2.63}$$

where submatrix $\mathbf{N_3}$ is a 3 x 3 null or zero matrix and submatrix $\mathbf{I_3}$ is the 3 x 3 identity matrix. The elements of the submatrix $\mathbf{\Omega^*_{i,j}}$ represent the second partial derivatives, $\frac{\partial^2 \Omega^*}{\partial i \partial j}$, evaluated at the specified collinear Lagrangian point.

$$\mathbf{\Omega^*_{i,j}} = \begin{bmatrix} \Omega^*_{xx} & \Omega^*_{xy} & \Omega^*_{xz} \\ \Omega^*_{yx} & \Omega^*_{yy} & \Omega^*_{yz} \\ \Omega^*_{zx} & \Omega^*_{zy} & \Omega^*_{zz} \end{bmatrix} \tag{2.64}$$

The cross-partial terms in the matrix in Equation (2.64) are evaluated from Equations (2.56) - (2.61). All the cross-partial values are zero because $y_{L_i} = z_{L_i} = 0$ for the collinear Lagrangian points. Concerning the diagonal elements, it is apparent via observations of Equations (2.53) - (2.55) that the appropriate signs are

$$\Omega^*_{xx} > 0, \ \Omega^*_{yy} < 0, \ \Omega^*_{zz} < 0 \tag{2.65}$$

Similary, based on the linear variational Equations (2.50) - (2.52), submatrix $\mathbf{D}$ is easily evaluated as

$$\mathbf{D} = \begin{bmatrix} 0 & 2 & 0 \\ -2 & 0 & 0 \\ 0 & 0 & 0 \end{bmatrix} \tag{2.66}$$

Equation (2.63) can be rewritten in a condensed state-space form as

$$\dot{\vec{x}} = \mathbf{A}\vec{x} \tag{2.67}$$

where matrix $\mathbf{A}$ is the system matrix

$$\mathbf{A} = \begin{bmatrix} \mathbf{N_3} & \mathbf{I_3} \\ \mathbf{\Omega^*_{i,j}} & \mathbf{D} \end{bmatrix} \tag{2.68}$$

and it observed that $\mathbf{A}$ is a constant matrix. In an expanded form, Equation (2.67) appears as

$$\begin{Bmatrix} \dot{\xi} \\ \dot{\eta} \\ \dot{\zeta} \\ \ddot{\xi} \\ \ddot{\eta} \\ \ddot{\zeta} \end{Bmatrix} = \begin{bmatrix} 0 & 0 & 0 & 1 & 0 & 0 \\ 0 & 0 & 0 & 0 & 1 & 0 \\ 0 & 0 & 0 & 0 & 0 & 1 \\ \Omega^*_{xx} & 0 & 0 & 0 & 2 & 0 \\ 0 & \Omega^*_{yy} & 0 & -2 & 0 & 0 \\ 0 & 0 & \Omega^*_{zz} & 0 & 0 & 0 \end{bmatrix} \begin{Bmatrix} \xi \\ \eta \\ \zeta \\ \dot{\xi} \\ \dot{\eta} \\ \dot{\zeta} \end{Bmatrix} \tag{2.69}$$

From Equation (2.69), it is noted that the linear out-of-plane motion, represented by ζ and its derivatives, is decoupled from the linear in-plane motion in terms of ξ and η. As previously noted, $\Omega^*_{zz} < 0$; therefore, the roots associated with the out-of-plane motion are purely imaginary, and the linear out-of-plane motion is sinusoidal, that is,

$$\zeta = C_1 Cos(\omega\tau) + C_2 Sin(\omega\tau) \tag{2.70}$$

where C_1 and C_2 are constants; $\omega = \sqrt{|\Omega^*_{zz}|}$ is the frequency associated with the harmonic out-of-plane component, ζ. For the in-plane motion, the solution to the linear, first-order differential equations appears in the form

$$\xi = \sum_{k=1}^{4} A_k e^{\lambda_k \tau} \tag{2.71}$$

$$\eta = \sum_{k=1}^{4} B_k e^{\lambda_k \tau} \tag{2.72}$$

where A_k and B_k are interdependant constants of integration, and λ_k are the four eigenvalues of matrix $\mathbf{A}$ associated with the in-plane motion. Note that there are

only four terms in the summation as the remaining two terms associated with the out-of-plane motion are decoupled from the in-plane excursions. The characteristic polynomial corresponding only to the in-plane behavior is formulated using information from Equations (2.50) - (2.51),

$$\lambda^4 + (4 - \Omega^*_{xx} - \Omega^*_{yy})\lambda^2 + 2(\Omega^*_{xy} - \Omega^*_{yx})\lambda + (\Omega^*_{xx}\Omega^*_{yy} - \Omega^*_{xy}\Omega^*_{yx}) = 0 \tag{2.73}$$

Limiting the analysis to the collinear points, i.e. $y_{L_i} = z_{L_i} = 0$ and $\Omega^*_{xy} = \Omega^*_{yx} = 0$, further reduces Equation (2.73) to the form

$$\lambda^4 + (4 - \Omega^*_{xx} - \Omega^*_{yy})\lambda^2 + \Omega^*_{xx}\Omega^*_{yy} = 0 \tag{2.74}$$

Note that $\Omega^*_{xx}\Omega^*_{yy} < 0$. Because of the form of Equation (2.74), it is easily transformed from a quartic to a quadratic characteristic equation of the form

$$\Lambda^2 + 2\beta_1\Lambda - \beta_2^2 = 0 \tag{2.75}$$

where Λ represents the roots of Equation (2.75). The associated constants are reformulations of the coefficients from Equation (2.74), that is,

$$\beta_1 = 2 - \frac{\Omega^*_{xx} + \Omega^*_{yy}}{2} \tag{2.76}$$

$$\beta_2^2 = -\Omega^*_{xx}\Omega^*_{yy} \tag{2.77}$$

Note that, β_1 and β_2 are both real. The quadratic roots of Equation (2.75) are evaluated as

$$\Lambda_1 = -\beta_1 + \sqrt{\beta_1^2 + \beta_2^2} \tag{2.78}$$

$$\Lambda_2 = -\beta_1 - \sqrt{\beta_1^2 + \beta_2^2} \tag{2.79}$$

Based on the signs of Ω^*_{xx} and Ω^*_{yy}, then $\Omega^*_{xx}\Omega^*_{yy} < 0$, and the observation leads to the conclusion that $\Lambda_1 > 0$ and $\Lambda_2 < 0$. Thus, the quintic roots of Equation (2.74) are computed as

$$\lambda_{1,2} = \pm\sqrt{\Lambda_1} \tag{2.80}$$

$$\lambda_{3,4} = \pm\sqrt{\Lambda_2} \tag{2.81}$$

Further analysis into the quintic eigenvalues reveals that $\lambda_{1,2}$ are real ($\Re$) eigenvalues and $\lambda_{3,4}$ are pure imaginary ($\Im$) eigenvalues associated with the system represented by Equation (2.74). Lyapunov's criteria for the stability associated with a linear system and a corresponding nonlinear solution states that [25]

- If the $\Re(\lambda_i) < 0 \; \forall$ the eigenvalues associated with the linear system of equations relative to L_i, the nonlinear solution is asymptotically stable.
- If the $\Re(\lambda_i) > 0$ for at least one of the eigenvalues associated with the linear system of equations relative to L_i, the nonlinear solution is unstable.
- If the $\Re(\lambda_i) \leq 0$ and at least one of the $\Re(\lambda_i) = 0$ for the eigenvalues associated with the linear system of equations relative to L_i, no conclusion is available concerning the stability of the solution in the nonlinear system.

Equation (2.80) demonstrates that there are two real eigenvalues associated with the in-plane motion relative to the collinear Lagrangian points, one of which is positive and the other is negative. Thus, the positive, real eigenvalue result yields the conclusion that the collinear Lagrangian points are intrinsically linearly unstable. Equation (2.81) further demonstrates that there exist imaginary eigenvalues associated with the in-plane motion in the vicinity of the collinear Lagrangian points. Consequently, it is possible to appropriately select initial conditions, $\xi(\tau_0)$ and $\eta(\tau_0)$ such that the divergent behavior is not excited.

To explore the planar behavior in the vicinity of the collinear Lagrangian points, it is possible to select the coefficients in Equations (2.71) - (2.72) such that only the stable terms are excited [5]. As noted previously, coefficients in Equation (2.71) - (2.72) are interdependent and the following relationship is developed between the coefficients associated with the in-plane motion

$$B_i = \nu_i A_i \tag{2.82}$$

where

$$\nu_i = \frac{\lambda_i^2 - \Omega_{xx}^*}{2\lambda_i} \tag{2.83}$$

By expanding Equations (2.71) and (2.72)

$$\xi = A_1 e^{\lambda_1 \tau} + A_2 e^{\lambda_2 \tau} + A_3 e^{\lambda_3 \tau} + A_4 e^{\lambda_4 \tau} \tag{2.84}$$

$$\eta = A_1 \nu_1 e^{\lambda_1 \tau} + A_2 \nu_2 e^{\lambda_2 \tau} + A_3 \nu_3 e^{\lambda_3 \tau} + A_4 \nu_4 e^{\lambda_4 \tau} \tag{2.85}$$

and it is evident that coefficients A_1 and A_2 are associated with the unstable eigenvalues λ_1 and λ_2. To inhibit the excitation of the unstable mode, initial conditions must be selected such that A_1 and A_2 are equal to zero. Also recall that the imaginary roots are equal in magnitude, i.e., $\lambda_4 = -\lambda_3$ and $\nu_4 = -\nu_3$. Thus, initial conditions, given A_3 and A_4, are evaluated from

$$\xi = A_3 e^{\lambda_3 \tau} + A_4 e^{-\lambda_3 \tau} \tag{2.86}$$

$$\eta = A_3 \nu_3 e^{\lambda_3 \tau} - A_4 \nu_3 e^{-\lambda_3 \tau} \tag{2.87}$$

Initially, $\xi(\tau_0) = \xi_0$ and $\eta(\tau_0) = \eta_0$. Equations (2.86) and (2.87) are then evaluated at the initial time, $\tau = \tau_0$, and the following expressions for A_3 and A_4 are deduced

$$A_3 = \frac{\xi_0 \nu_3 + \eta_0}{2\nu_3 e^{\lambda_3 \tau_0}} \tag{2.88}$$

$$A_4 = \frac{\xi_0 \nu_3 - \eta_0}{2\nu_3 e^{-\lambda_3 \tau_0}} \tag{2.89}$$

When $\tau_0 = 0, A_3$ and A_4 are further reduced to

$$A_3 = \frac{\xi_0 \nu_3 + \eta_0}{2\nu_3} \tag{2.90}$$

$$A_4 = \frac{\xi_0 \nu_3 - \eta_0}{2\nu_3} \tag{2.91}$$

The general solution for in-plane motion near the vicinity of the collinear Lagrangian points is summarized as

$$\xi = \xi_0 Cos[s(\tau - \tau_0)] + \frac{\eta_0}{\beta_3} Sin[s(\tau - \tau_0)] \tag{2.92}$$

$$\eta = \eta_0 Cos[s(\tau - \tau_0)] + \xi_0 \beta_3 Sin[s(\tau - \tau_0)] \tag{2.93}$$

where s and β_3 are real quantities, i.e.,

$$\lambda_3 = is \tag{2.94}$$

$$\nu_3 = i\beta_3 \tag{2.95}$$

The representative expressions for s and β_3 are

$$s = \sqrt{\beta_1 + \sqrt{\beta_1^2 + \beta_2^2}} \tag{2.96}$$

$$\beta_3 = \frac{s^2 + \Omega_{xx}^*}{2s} \tag{2.97}$$

Initial conditions for the in-plane relative velocity components are derived by evaluating the derivatives of Equations (2.92) and (2.93) at $\tau = \tau_0$

$$\dot{\xi}_0 = \frac{\eta_0 s}{\beta_3} \tag{2.98}$$

$$\dot{\eta}_0 = -\xi_0 \beta_3 s \tag{2.99}$$

For a particular set of initial conditions, ξ and η, a specific set of initial velocities, $\dot{\xi}$ and $\dot{\eta}$, results in a periodic orbit about L_1 Lagrangian point as plotted in Figure 2.3. For visualization purposes, the Earth has been scaled to 10 times its actual size. The trajectory in the figure represents a first-order linear approximation to a particular solution of the equations of motion in CR3BP. An initial state along the x-axis at a distance of $200,000$ km from the L_1 libration point but opposite to the Earth is selected. Based on this value, other initial conditions are generated.

$$\begin{array}{ll} \xi_0 = 200,000 \text{ km} & \dot{\xi}_0 = 0 \text{ km/s} \\ \eta_0 = 0 \text{ km} & \dot{\eta}_0 = 0.268306831786395 \text{ km/s} \end{array}$$

The period of this orbit is 175 days, approximately half the period of the Earth in its orbit about the Sun. Propagation of these initial conditions in a nonlinear model results in departure of the spacecraft from the vicinity of this linear approximate trajectory, i.e., once the unstable behavior is triggered, the path departs from the L_1 vicinity. But the linear solution can be employed as a good initial guess for numerical techniques to produce an exact solution in the nonlinear model.

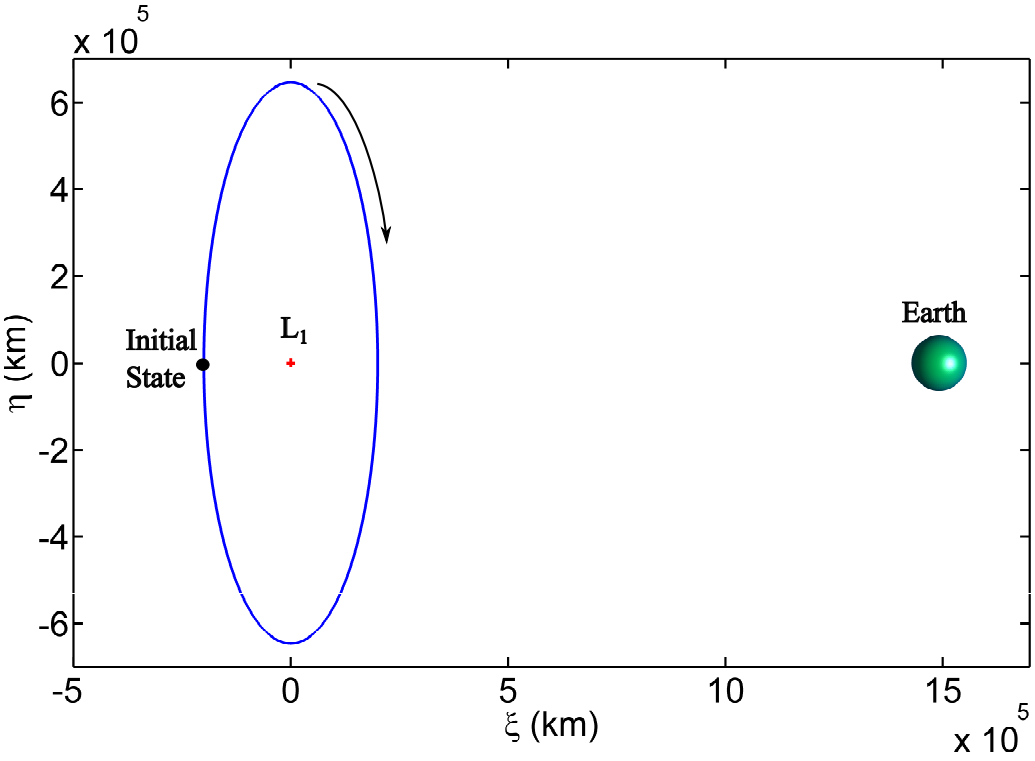

Figure 2.3. L_1 Linearized Periodic Orbit in Sun-Earth System.

3. DIFFERENTIAL CORRECTIONS ALGORITHM FOR TRAJECTORY DESIGN

Construction of trajectories within a nonlinear force environment can be facilitated with a differential corrections scheme. Any corrections algorithm employs numerical techniques to search for periodic orbits and trajectories in the CR3BP; of particular interest are the regions in the vicinity of the Lagrangian points. To accomplish the development of a corrections algorithm, it is important to understand the sensitivity associated with the states along the trajectory.

3.1 The State Transition Matrix

Prior to assessing the behavior of a particle or body under the influence of nonlinear forces, it is critical to investigate the evolution of a state over time in response to changes in the initial state. This linear map, that is, the state transition matrix (STM), is formulated based on a linear variational model to estimate the final state as a response to certain perturbations introduced in the initial state [26]. The STM is particularly useful for trajectory design and periodic orbit computation. To develop an expression for the STM, a baseline reference arc is first calculated. Let there be a certain six-dimensional initial state vector, $\vec{X}(\tau_0)$, that results in a time-varying reference path, $\vec{X}(\tau)$. By introducing a small perturbation, $\delta\vec{X}(\tau_0)$, to the initial state, an updated initial state, $\vec{X}^*(\tau_0)$, results in a new time-varying nearby arc, $\vec{X}^*(\tau)$,

$$\vec{X}^*(\tau_0) = \vec{X}(\tau_0) + \delta\vec{X}(\tau_0) \tag{3.1}$$

where

$$\vec{X}(\tau_0) = \left\{ x_0 \quad y_0 \quad z_0 \quad \dot{x}_0 \quad \dot{y}_0 \quad \dot{z}_0 \right\}^T \tag{3.2}$$

$$\delta\vec{X}(\tau_0) = \left\{ \delta x_0 \quad \delta y_0 \quad \delta z_0 \quad \delta \dot{x}_0 \quad \delta \dot{y}_0 \quad \delta \dot{z}_0 \right\}^T \tag{3.3}$$

A schematic demonstrating the above scenario appears in Figure 3.1. The state along

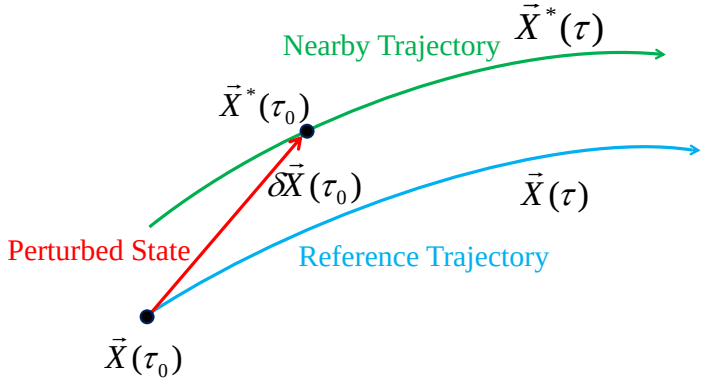

Figure 3.1. Reference Trajectory, Perturbed State and Nearby Trajectory Arc.

a nearby trajectory is approximated based on the STM. Using the first-order Taylor series expansion about the reference and neglecting the higher-order terms, the linear vector variational relationship is written

$$\delta\dot{\vec{X}} = \mathbf{A}(\tau)\delta\vec{X} \tag{3.4}$$

In contrast to Equation (2.68), the $\mathbf{A}$ matrix is time dependent, and the partials of the equations of motion are evaluated along the reference path. The partials corresponding to the elements of $\mathbf{A}$ matrix are formulated such that

$$\left.\frac{\partial\vec{F}}{\partial\vec{X}}\right|_{\vec{X}(\tau)} = \mathbf{A}(\tau) = \begin{bmatrix} \mathbf{N_3} & \mathbf{I_3} \\ \mathbf{\Omega_{i,j}}(\tau) & \mathbf{D} \end{bmatrix} \tag{3.5}$$

The general solution to the linear vector form of variational relationship in Equation (3.4) is expressed as

$$\delta\vec{X}(\tau_f) = \Phi(\tau_f, \tau_0)\delta\vec{X}(\tau_0) \tag{3.6}$$

where $\Phi(\tau_f, \tau_0)$ is the STM that maps the change in initial state, $\delta\vec{X}(\tau_0)$ to the change in final state, $\delta\vec{X}(\tau_f)$ at a final time, τ_f, along the reference trajectory, $\vec{X}(\tau)$. The elements of the STM matrix are evaluated by simultaneously numerically integrating the variational vector equation along with the equations of motion for the system. The matrix form of the differential equations is

$$\dot{\Phi}(\tau_f, \tau_0) = \mathbf{A}(\tau_f)\Phi(\tau_f, \tau_0) \tag{3.7}$$

Given six scalar variational states, as defined in Equation 3.3, the elements of the 6×6 STM are evaluated in terms of the following partials

$$\Phi(\tau_f, \tau_0) = \begin{bmatrix} \frac{\partial x}{\partial x_0} & \frac{\partial x}{\partial y_0} & \frac{\partial x}{\partial z_0} & \frac{\partial x}{\partial \dot{x}_0} & \frac{\partial x}{\partial \dot{y}_0} & \frac{\partial x}{\partial \dot{z}_0} \\ \frac{\partial y}{\partial x_0} & \frac{\partial y}{\partial y_0} & \frac{\partial y}{\partial z_0} & \frac{\partial y}{\partial \dot{x}_0} & \frac{\partial y}{\partial \dot{y}_0} & \frac{\partial y}{\partial \dot{z}_0} \\ \frac{\partial z}{\partial x_0} & \frac{\partial z}{\partial y_0} & \frac{\partial z}{\partial z_0} & \frac{\partial z}{\partial \dot{x}_0} & \frac{\partial z}{\partial \dot{y}_0} & \frac{\partial z}{\partial \dot{z}_0} \\ \frac{\partial \dot{x}}{\partial x_0} & \frac{\partial \dot{x}}{\partial y_0} & \frac{\partial \dot{x}}{\partial z_0} & \frac{\partial \dot{x}}{\partial \dot{x}_0} & \frac{\partial \dot{x}}{\partial \dot{y}_0} & \frac{\partial \dot{x}}{\partial \dot{z}_0} \\ \frac{\partial \dot{y}}{\partial x_0} & \frac{\partial \dot{y}}{\partial y_0} & \frac{\partial \dot{y}}{\partial z_0} & \frac{\partial \dot{y}}{\partial \dot{x}_0} & \frac{\partial \dot{y}}{\partial \dot{y}_0} & \frac{\partial \dot{y}}{\partial \dot{z}_0} \\ \frac{\partial \dot{z}}{\partial x_0} & \frac{\partial \dot{z}}{\partial y_0} & \frac{\partial \dot{z}}{\partial z_0} & \frac{\partial \dot{z}}{\partial \dot{x}_0} & \frac{\partial \dot{z}}{\partial \dot{y}_0} & \frac{\partial \dot{z}}{\partial \dot{z}_0} \end{bmatrix} \tag{3.8}$$

To numerically integrate and evaluate the 36 time-varying elements of the STM, the initial conditions for the matrix differential equation in Equation (3.7) are specified; the initial state is also apparent from Equation (3.6), that is,

$$\Phi(\tau_0, \tau_0) = I_{6\times6} \tag{3.9}$$

where $I_{6\times6}$ is a 6×6 identity matrix. The STM is employed in any corrections strategy to design trajectory arcs and periodic orbits. It also offers insight in the examination of the stability associated with the trajectory.

3.2 Differential Corrections Algorithm

Trajectory design is accomplished through the application of a differential corrections scheme to a two-point boundary value problem (2PBVP). The STM is formulated to supply a linear estimate of the final states as the result of a variation in the

initial states and is then incorporated in a shooting algorithm. An iterative process is employed that is based on information provided by the STM. In a simple targeting scheme, given an available baseline reference trajectory, the corrections algorithm is applied to iteratively adjust the initial states, based on the miss difference at the final state, until a certain level of tolerance is achieved. There are a variety of approaches to implement a corrections process. A formulation based on constraints and free-variables is employed in this analysis.

In the algorithm for the shooting scheme, constraints can be specified as the desired target states; then, free-variables are the available controls. This formulation is relatively easy to implement and the constraints are straightforward to add. In simple targeting, the 'controls' are the initial states governing the path of the spacecraft. In a general formulation, the vector, $\vec{X}$, includes the states acting as control parameters that are employed to meet some set of constraints associated with the trajectory. Initiate the algorithm by first recognizing n free-variables that form a base design variable vector, $\vec{X}$

$$\vec{X}(\tau) = \left\{ \begin{array}{c} \vec{X}_1 \\ \vec{X}_2 \\ \vdots \\ \vec{X}_{n-1} \\ \vec{X}_n \end{array} \right\} \tag{3.10}$$

For the simple case, let $\vec{X}_i$ be a one-dimensional vector. Thus, this control variable vector can consist of the six states associated with the position and the velocity at some initial time, τ_0. The m scalar constraint equations, $F_i(\vec{X})$, are required to be fulfilled by the available controls and are collected into the vector $\vec{F}(\vec{X})$

$$\vec{F}(\vec{X}) = \left\{ \begin{array}{c} F_1(\vec{X}) \\ F_2(\vec{X}) \\ \vdots \\ F_{m-1}(\vec{X}) \\ F_m(\vec{X}) \end{array} \right\} \tag{3.11}$$

The constraints are formulated such that $\vec{F}(\vec{X}) = \vec{0}$ if all the individual scalar constraints are satisfied. The corrections algorithm proceeds iteratively until a certain level of accuracy is achieved. The set of control variables that satisfy the constraints are defined as, $\vec{X}^*$, i.e.,

$$\vec{F}(\vec{X}^*) \cong \vec{0} \tag{3.12}$$

Samples of typical constraints include the position and the velocity or any other spacecraft related parameters. Thus, the constraint vector function, $\vec{F}(\vec{X})$, is evaluated in terms of a Taylor series expansion about a reference value, $\vec{X}^i$, such that,

$$\vec{F}(\vec{X}) \approx \vec{F}(\vec{X}^i) + D\vec{F}(\vec{X}^i)(\vec{X} - \vec{X}^i) \tag{3.13}$$

where $D\vec{F}(\vec{X}^i)$ is an $m \times n$ Jacobian matrix,

$$D\vec{F}(\vec{X}^i) = \frac{\partial \vec{F}(\vec{X}^i)}{\partial \vec{X}^i} = \begin{bmatrix} \frac{\partial F_1}{\partial\ X_1} & \frac{\partial F_1}{\partial X_2} & \cdots & \frac{\partial F_1}{\partial X_n} \\ \frac{\partial F_2}{\partial X_1} & \frac{\partial F_2}{\partial X_2} & \cdots & \frac{\partial F_2}{\partial X_n} \\ \vdots & \vdots & \ddots & \vdots \\ \frac{\partial F_m}{\partial X_1} & \frac{\partial F_m}{\partial X_2} & \cdots & \frac{\partial F_m}{\partial\ X_n} \end{bmatrix} \tag{3.14}$$

Since the goal is $\vec{F}(\vec{X}) = \vec{0}$, the expression in Equation (3.13) is employed to determine the value of $\vec{X}$ that achieves the goal. Recognizing that the system is nonlinear, Equation (3.13) is rewritten as an expression that is to be solved iteratively, that is,

$$\vec{F}(\vec{X}^j) + D\vec{F}(\vec{X}^j)(\vec{X}^{j+1} - \vec{X}^j) = \vec{0} \tag{3.15}$$

The partials within the Jacobian matrix, $D\vec{F}(\vec{X}^j)$ depend on the previous iteration (j^{th}) or the initial guess for the design vector, $\vec{X}$. The goal is to iteratively solve for $\vec{X}^{(j+1)}$ until

$$\vec{F}(\vec{X}^{j+1}) = \vec{F}(\vec{X}^c) \approx \vec{0} \tag{3.16}$$

The process is continued until reaching a pre-specified tolerance level.

The number of control variables, n, and constraints, m, influences the type of possible solutions that exist for Equation (3.15). When the number of control variables equals the number of constraints

$$n = m \quad \Rightarrow \ \textit{Unique Solution} \tag{3.17}$$

The uniqueness of this solution is based on $D\vec{F}(\vec{X}^j)$ as a square matrix and is then inverted to determine a solution to Equation (3.15),

$$\vec{X}^{j+1} = \vec{X}^j - D\vec{F}(\vec{X}^j)^{-1}\vec{F}(\vec{X}^j) \tag{3.18}$$

The change in initial control variables is then $\delta\vec{X}$

$$\delta\vec{X} = -D\vec{F}(\vec{X}^j)^{-1}\vec{F}(\vec{X}^j) \tag{3.19}$$

When the number of controls available is greater than the number of constraints

$$n > m \quad \Rightarrow \; Infinite\ Number\ of\ Solutions \tag{3.20}$$

The Jacobian matrix, $D\vec{F}(\vec{X}^j)$, is no longer a square matrix and to select a solution from among all the possible options that satisfy Equation (3.15), a minimum norm solution yields

$$\vec{X}^{j+1} = \vec{X}^j - D\vec{F}(\vec{X}^j)^T[D\vec{F}(\vec{X}^j)D\vec{F}(\vec{X}^j)^T]^{-1}\vec{F}(\vec{X}^j) \tag{3.21}$$

Equation (3.21) can be rewritten as the change in the initial control states that are required to meet the constraints, i.e.

$$\delta\vec{X} = -D\vec{F}(\vec{X}^j)^T[D\vec{F}(\vec{X}^j)D\vec{F}(\vec{X}^j)^T]^{-1}\vec{F}(\vec{X}^j) \tag{3.22}$$

A minimum norm solution is based on a gradient search process that is more successful when $\delta\vec{X}$ is small. Thus, this methodology seeks a solution that exists in the vicinity of $\vec{X}^j$ such that $\vec{X}^{j+1}$ is characterized by traits that are closely related to those of $\vec{X}^j$. This corrections scheme can be applied in both fixed- and variable-time single shooting algorithms.

3.2.1 Fixed-Time Single Shooting

As an example of a targeting algorithm, consider a vehicle at a given location with some velocity. The goal is the modification of the initial velocity to reach a specified position downstream. A fixed-time single shooting algorithm is employed to

determine a single arc that is delivered to the desired final state, $\vec{X}^*(\tau_f)$, by adjusting the available controls within the initial state vector, $\vec{X}(\tau_0)$,

$$\vec{X}(\tau_0) = \left\{\vec{X}_1\right\} = \begin{Bmatrix} x_0 \\ y_0 \\ z_0 \\ \dot{x}_0 \\ \dot{y}_0 \\ \dot{z}_0 \end{Bmatrix} \tag{3.23}$$

Note, $\vec{X}$ is comprised of only one six-dimensional state vector. A schematic representing a fixed-time single shooting algorithm appears in Figure 3.2. Note that τ_0 represents the initial nondimensional time and the state, $\vec{X}$, is initially defined at τ_0. A reference trajectory is generated that acts as the baseline for the corrections scheme and is supplied as an initial guess for the appropriate arc. The state at the end of the reference trajectory is defined as $\vec{X}(\tau_f)$.

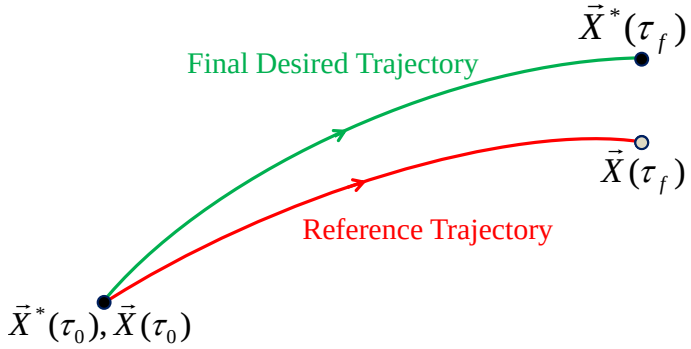

Figure 3.2. Fixed-Time Single Shooting Illustration.

In the example, the corrections scheme is formulated to target a desired state, $\vec{X}^*(\tau_f)$. The final six-dimensional state vector is expressed in terms of the three-dimensional position vector, $\vec{r}^*$, and the three-dimensional velocity vector, $\vec{v}^*$, that is

$$\vec{X}^*(\tau_f) = \begin{Bmatrix} \vec{r}^* \\ \vec{v}^* \end{Bmatrix} \tag{3.24}$$

where τ_f is the nondimensional time corresponding to the end of the arc and delivers the path to the target state. Based on the definitions, $(\tau_f - \tau_0)$ is the time of flight (TOF) between the initial and the final states; one option maintains the TOF, thus, the time remains fixed along both the baseline trajectory and the desired path. To formulate the problem in this simple example, only the position state, $\vec{r}^*$, at the end of the desired trajectory is targeted and the velocity state, $\vec{v}^*$, at the final time is unrestricted. The desired final scalar position states, i.e., the target vector, is

$$\vec{r}^* = \begin{bmatrix} x^* \\ y^* \\ z^* \end{bmatrix} \tag{3.25}$$

The initial three velocity states are formulated to define the available design variables in the design variable vector, $\vec{X}(\tau_0)$, and are submitted to the algorithm as

$$\vec{X}(\tau_0) = \vec{v}_0 = \begin{bmatrix} \dot{x}_0 \\ \dot{y}_0 \\ \dot{z}_0 \end{bmatrix} \tag{3.26}$$

The constraint vector is written as the difference between the position states along the reference path at the terminal time and the final specified target position states,

$$\vec{F}(\vec{X}) = \left\{ \vec{r}(\tau_f) - \vec{r}^*(\tau_f) \right\} = \begin{bmatrix} x - x^* \\ y - y^* \\ z - z^* \end{bmatrix} \tag{3.27}$$

The iterations proceed until the constraint equation meets the $\vec{F}(\vec{X}^*) = \vec{0}$ requirement such that the actual value $\vec{F}(\vec{X}^*) \approx \vec{0}$ within a specified tolerance level. For this example, the Jacobian matrix introduced in Equation (3.14) is written in terms of submatrices relating the final position and velocity to the initial position and velocity vectors

$$D\vec{F}(\vec{X}) = \frac{\partial \vec{F}(\vec{X})}{\partial \vec{X}} = \begin{bmatrix} \frac{\partial \vec{r}}{\partial \vec{r}_0} & \frac{\partial \vec{r}}{\partial \vec{v}_0} \\ \frac{\partial \vec{v}}{\partial \vec{r}_0} & \frac{\partial \vec{v}}{\partial \vec{v}_0} \end{bmatrix} \tag{3.28}$$

As the initial design variables are represented in $\vec{X}(\tau_0)$ in Equation (3.26) and only the end position states, $\vec{r}$, at time, τ_f, are targeted using the initial velocity states, $\vec{v}_0$, as the available design variables, Equation (3.28) reduces to the following 3×3 matrix,

$$D\vec{F}(\vec{X}) = \frac{\partial \vec{F}(\vec{X})}{\partial \vec{X}} = \frac{\partial \vec{r}}{\partial \vec{v}_0} = \begin{bmatrix} \frac{\partial x}{\partial \dot{x}_0} & \frac{\partial x}{\partial \dot{y}_0} & \frac{\partial x}{\partial \dot{z}_0} \\ \frac{\partial y}{\partial \dot{x}_0} & \frac{\partial y}{\partial \dot{y}_0} & \frac{\partial y}{\partial \dot{z}_0} \\ \frac{\partial z}{\partial \dot{x}_0} & \frac{\partial z}{\partial \dot{y}_0} & \frac{\partial z}{\partial \dot{z}_0} \end{bmatrix} \tag{3.29}$$

Comparison between Equation (3.8) and Equation (3.29) results in a new expression for $D\vec{F}(\vec{X})$ in terms of the elements of the STM

$$D\vec{F}(\vec{X}) = \frac{\partial \vec{r}}{\partial \vec{v}_0} = \begin{bmatrix} \phi_{14} & \phi_{15} & \phi_{16} \\ \phi_{24} & \phi_{25} & \phi_{26} \\ \phi_{34} & \phi_{35} & \phi_{36} \end{bmatrix} \tag{3.30}$$

The elements, ϕ_{pq}, in Equation (3.30) represent the change in the position states at the terminal time along the reference trajectory, $\vec{r} = [x \ y \ z]^T$ as a result of adjustments in the initial velocity state, $\vec{v}_0 = [\dot{x}_0 \ \dot{y}_0 \ \dot{z}_0]^T$. The partials are, thus, all evaluated along the reference path. For the update equation, the number of available controls, n, equals the number of constraints, m, so a unique solution exists. The update equation for successive iteration is expressed as,

$$\vec{X}^{j+1} = \begin{bmatrix} \dot{x}_0^{j+1} \\ \dot{y}_0^{j+1} \\ \dot{z}_0^{j+1} \end{bmatrix} = \vec{X}^j + \delta\vec{X}^j = \begin{bmatrix} \dot{x}_0^j \\ \dot{y}_0^j \\ \dot{z}_0^j \end{bmatrix} + \begin{bmatrix} \delta\dot{x}_0^j \\ \delta\dot{y}_0^j \\ \delta\dot{z}_0^j \end{bmatrix} \tag{3.31}$$

where j represents the j^{th} iteration while applying Newton's method to solve for the unique solution. As is apparent in Equation (3.30), $D\vec{F}(\vec{X})$ is a square matrix. Thus, the change in the initial control variables is evaluated as

$$\delta\vec{X}^j = \begin{bmatrix} \delta\dot{x}_0^j \\ \delta\dot{y}_0^j \\ \delta\dot{z}_0^j \end{bmatrix} = -D\vec{F}(\vec{X}^j)^{-1}\vec{F}(\vec{X}^j) \tag{3.32}$$

Note that the reference path is updated at each step, that is, the $(j-1)^{th}$ arc serves as a reference path to trigger the j^{th} iteration. The iterative process, originating with the reference trajectory, continues until a final desired trajectory is determined that meets the end constraints to a specific tolerance.

3.2.2 Variable-Time Single Shooting

The strategy to develop a variable-time single shooting algorithm is easily formulated by augmenting the process summarized for a fixed-time single shooting scheme. The algorithm is augmented to allow the time-of-flight (TOF), i.e., the integration time ($\tau = \tau_f - \tau_0$), to vary over successive iterations. A schematic for variable-time single shooting appears in Figure 3.3. Note that the propagation time along the final desired path leading to desired state, $\vec{X}^*(\tau_f^*)$, is different from the end state, $\vec{X}(\tau_f)$, along the reference trajectory. Thus, TOF is now included in the design variable vector. Thus, the augmented design variable vector $\vec{X}(\tau_0)$ is

$$\vec{X}(\tau_0) = \begin{Bmatrix} \vec{v}_0 \\ \tau \end{Bmatrix} = \begin{bmatrix} \dot{x}_0 \\ \dot{y}_0 \\ \dot{z}_0 \\ \tau \end{bmatrix} \tag{3.33}$$

The shooting scheme is developed to target the same final position states as represented in Equation (3.25). Thus, the constraint vector remains the same as in

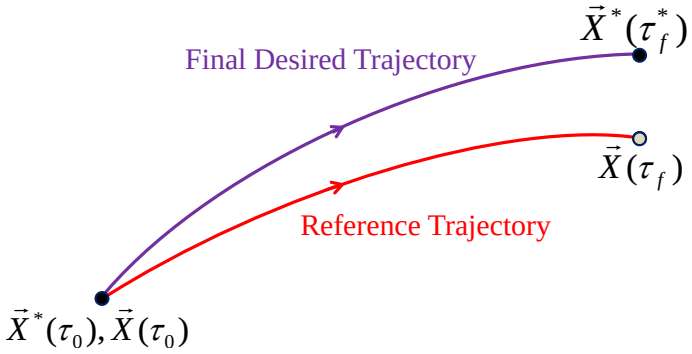

Figure 3.3. Variable-Time Single Shooting Illustration.

Equation (3.27). The Jacobian matrix introduced in Equation (3.14) is augmented to relate the final position and velocity to the initial position, velocity and TOF, τ,

$$D\vec{F}(\vec{X}) = \frac{\partial \vec{F}(\vec{X})}{\partial \vec{X}} = \begin{bmatrix} \frac{\partial \vec{r}}{\partial \vec{r}_0} & \frac{\partial \vec{r}}{\partial \vec{v}_0} & \frac{\partial \vec{r}}{\partial \tau} \\ \frac{\partial \vec{v}}{\partial \vec{r}_0} & \frac{\partial \vec{v}}{\partial \vec{v}_0} & \frac{\partial \vec{v}}{\partial \tau} \end{bmatrix} \tag{3.34}$$

The augmented design variable vector represented in Equation (3.33) and the final desired position states reduce Equation (3.34) to the following form

$$D\vec{F}(\vec{X}) = \frac{\partial \vec{F}(\vec{X})}{\partial \vec{X}} = \begin{Bmatrix} \frac{\partial \vec{r}}{\partial \vec{v}_0} & \frac{\partial \vec{r}}{\partial \tau} \end{Bmatrix} = \begin{bmatrix} \frac{\partial x}{\partial \dot{x}_0} & \frac{\partial x}{\partial \dot{y}_0} & \frac{\partial x}{\partial \dot{z}_0} & \frac{\partial x}{\partial \tau} \\ \frac{\partial y}{\partial \dot{x}_0} & \frac{\partial y}{\partial \dot{y}_0} & \frac{\partial y}{\partial \dot{z}_0} & \frac{\partial y}{\partial \tau} \\ \frac{\partial z}{\partial \dot{x}_0} & \frac{\partial z}{\partial \dot{y}_0} & \frac{\partial z}{\partial \dot{z}_0} & \frac{\partial z}{\partial \tau} \end{bmatrix} \tag{3.35}$$

Recall that the elements of this matrix are all evaluated along the reference path. The augmented matrix $D\vec{F}(\vec{X})$ is rewritten in terms of the elements of the STM and the velocities at the terminal time along the reference path

$$D\vec{F}(\vec{X}) = \begin{Bmatrix} \frac{\partial \vec{r}}{\partial \vec{v}_0} & \frac{\partial \vec{r}}{\partial \tau} \end{Bmatrix} = \begin{bmatrix} \phi_{14} & \phi_{15} & \phi_{16} & \dot{x} \\ \phi_{24} & \phi_{25} & \phi_{26} & \dot{y} \\ \phi_{34} & \phi_{35} & \phi_{36} & \dot{z} \end{bmatrix} \tag{3.36}$$

Note that the matrix is no longer square. Since the number of available controls, n, is greater than the number of constraints, m, there exist an infinite number of solutions. Thus, the new update equation for successive iterations is expressed in the form

$$\vec{X}^{j+1} = \begin{bmatrix} \dot{x}_0^{j+1} \\ \dot{y}_0^{j+1} \\ \dot{z}_0^{j+1} \\ \tau^{j+1} \end{bmatrix} = \vec{X}^j + \delta\vec{X}^j = \begin{bmatrix} \dot{x}_0^j \\ \dot{y}_0^j \\ \dot{z}_0^j \\ \tau^j \end{bmatrix} + \begin{bmatrix} \delta\dot{x}_0^j \\ \delta\dot{y}_0^j \\ \delta\dot{z}_0^j \\ \delta\tau^j \end{bmatrix} \tag{3.37}$$

Recall, the subscript, 0, represents the initial state at time, τ_0. The solution is no longer unique. Based upon a minimum norm solution, the change in the initial control variables is evaluated from

$$\delta\vec{X}^j = \begin{bmatrix} \delta\dot{x}_0^j \\ \delta\dot{y}_0^j \\ \delta\dot{z}_0^j \\ \delta\tau^j \end{bmatrix} = -D\vec{F}(\vec{X}^j)^T[D\vec{F}(\vec{X}^j)D\vec{F}(\vec{X}^j)^T]^{-1}\vec{F}(\vec{X}^j) \tag{3.38}$$

Again, the algorithm is repeated to update the design parameters until the constraint vector meets a certain level of tolerance.

3.3 Multiple Shooting Algorithm

For more complex scenarios and for the option of additional types of constraints, the concept of differential corrections is further extended to develop a targeting scheme for a set of n discrete points. The foundation of any multiple shooting strategy lies in the corrections algorithm which can be based on the same steps as those employed in a single shooting scheme. The trajectory is decomposed into segments that originate from a sequence of patch points. The objective is typically convergence to a path continuous in position and velocity. Such a result is accomplished by targeting the end state originating from the $(n-1)^{th}$ patch point such that it

merges with the initial states along the next segment, i.e., the n^{th} patch point. An illustration that demonstrates a multiple shooting scheme is represented in Figure 3.4 where $\vec{X}_i(\tau_{0_i})$ represents the initial state at each patch point and $\vec{X}_i(\tau_{f_i})$ identifies the reference states after the trajectory arc is propagated for nondimensional time, τ_i, that is equivalent to

$$\tau_i = \tau_{f_i} - \tau_{0_i} \tag{3.39}$$

Multiple patch points aid in offsetting the numerical sensitivity associated with the

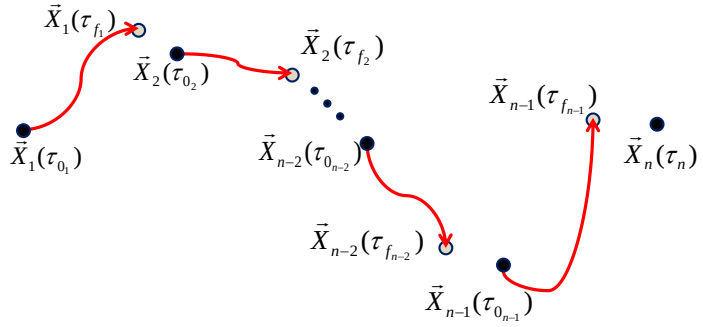

Figure 3.4. Unconverged Multiple Shooting Schematic.

trajectory design in the vicinity of the Lagrangian points. To formulate a trajectory continuous in both position and velocity, constraints are added such that the end states along any segment coincide with the initial point on the subsequent segment. Once a converged path is achieved, the updated states, $\vec{X}_i^*(\tau_{0_i})$, are iteratively established as illustrated in Figure 3.5. Based on the specific scenario, the TOF may or

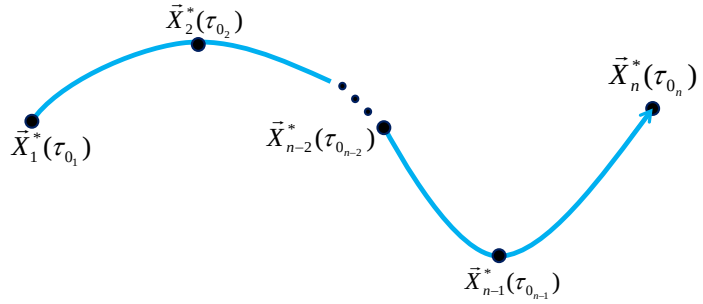

Figure 3.5. Converged Multiple Shooting Schematic.

may not be allowed to vary along each segment. This option allows two different formulations for multiple shooting, i.e., fixed-time and variable-time multiple shooting scheme.

3.3.1 Fixed-Time Multiple Shooting

Fixing the integration time, τ_i, along each of the trajectory segments that comprise the path results in the formulation of a fixed-time multiple shooting scheme. The design variable vector is comprised of both the position and the velocity states corresponding to each patch point, in the general form

$$\vec{X} = \begin{Bmatrix} \vec{X}_1(\tau_{0_1}) \\ \vec{X}_2(\tau_{0_2}) \\ \vdots \\ \vec{X}_{n-1}(\tau_{0n-1}) \\ \vec{X}_n(\tau_{0_n}) \end{Bmatrix} \tag{3.40}$$

where $\vec{X}_i(\tau_{0_i})$ is a six-dimensional vector and n indicates the number of path points to discretize the trajectory into segments. Thus, $\vec{X}$ is a $6n \times 1$ dimensional design variable vector for a fixed-time multiple shooting algorithm. As represented in Figure 3.4, there exists a discontinuity between the end reference states along each segment, $\vec{X}_i(\tau_{f_i})$, and the states at the subsequent patch point, $\vec{X}_{i+1}(\tau_{0_{i+1}})$, that is, the initial point on the subsequent arc. The constraint vector, $\vec{F}(\vec{X})$, is constructed to maintain continuity in both position and velocity states across multiple arcs,

$$\vec{F}(\vec{X}) = \begin{Bmatrix} \vec{X}_1(\tau_{f_1}) - \vec{X}_2(\tau_{0_2}) \\ \vec{X}_2(\tau_{f_2}) - \vec{X}_3(\tau_{0_3}) \\ \vdots \\ \vec{X}_{n-2}(\tau_{f_{n-2}}) - \vec{X}_{n-1}(\tau_{0_{n-1}}) \\ \vec{X}_{n-1}(\tau_{f_{n-1}}) - \vec{X}_n(\tau_{0_n}) \end{Bmatrix} \tag{3.41}$$

The length of the constraint vector is $6(n-1)$ since the number of arcs is one less than the number of patch points. Again the objective is convergence to a path continuous in both position and velocity to a pre-specified tolerance.

The Jacobian matrix, $D\vec{F}(\vec{X})$, is constructed based on the partials relating the constraint vector to variations in the design variables. The Jacobian matrix, $D\vec{F}(\vec{X})$, is a banded matrix, i.e., the non-zero entries are along the diagonals,

$$D\vec{F}(\vec{X}) = \begin{bmatrix} (\frac{\partial \vec{X}_1(\tau_{f_1})}{\partial \vec{X}_1(\tau_{0_1})} - \frac{\partial \vec{X}_2(\tau_{0_2})}{\partial \vec{X}_1(\tau_{0_1})}) & (\frac{\partial \vec{X}_1(\tau_{f_1})}{\partial \vec{X}_2(\tau_{0_2})} - \frac{\partial \vec{X}_2(\tau_{0_2})}{\partial \vec{X}_2(\tau_{0_2})}) & & \\ \ddots & \ddots & & \\ & (\frac{\partial \vec{X}_{n-1}(\tau_{f_{n-1}})}{\partial \vec{X}_{n-1}(\tau_{0_{n-1}})} - \frac{\partial \vec{X}_n(\tau_{0_n})}{\partial \vec{X}_{n-1}(\tau_{0_{n-1}})}) & (\frac{\partial \vec{X}_{n-1}(\tau_{f_{n-1}})}{\partial \vec{X}_n(\tau_{0_n})} - \frac{\partial \vec{X}_n(\tau_{0_n})}{\partial \vec{X}_n(\tau_{0_n})}) \end{bmatrix} \tag{3.42}$$

The end state along the reference arc i, $\vec{X}_i(\tau_{f_i})$, is a function of the initial states, $\vec{X}_i(\tau_{0_i})$. In this example, many of the scalar partials are elements of the STM. The subsequent patch point is not affected by the selection of the previous initial patch point and, thus, $\frac{\partial \vec{X}_{i+1}(\tau_{f_{i+1}})}{\partial \vec{X}_i(\tau_{0_i})}$ is equal to $\vec{0}$. Similarly, the end state along the i^{th} reference arc, $\vec{X}_i(\tau_{f_i})$, is not a function of the subsequent patch point, $\vec{X}_{i+1}$. Thus, $\frac{\partial \vec{X}_i(\tau_{f_i})}{\partial \vec{X}_{i+1}(\tau_{0_{i+1}})}$ is equal to $\vec{0}$. Finally, the partial $\frac{\partial \vec{X}_i(\tau_{0_i})}{\partial \vec{X}_i(\tau_{0_i})}$ is equal to the 6×6 identity matrix. Substituting this information yields a $6(n-1) \times 6n$ matrix,

$$D\vec{F}(\vec{X}) = \frac{\partial \vec{F}(\vec{X})}{\partial \vec{X}} = \begin{bmatrix} \phi(\tau_{f_1}, \tau_{0_1}) & -I_{6\times 6} & & \\ & \ddots & \ddots & \\ & & \phi(\tau_{f_{n-1}}, \tau_{0_{n-1}}) & -I_{6\times 6} \end{bmatrix} \tag{3.43}$$

Iteration is again employed to converge the constraint vector, $\vec{F}(\vec{X})$ to $\vec{0}$ within an acceptable tolerance by applying the appropriate update equation using the $D\vec{F}(\vec{X})$ matrix.

3.3.2 Variable-Time Multiple Shooting

Varying the integration time, τ_i, along each segment or arc results in the formulation of a variable-time multiple shooting scheme. The addition of integration time to the design variable vector results in a $7n-1$ vector; for n patch points, there are $n-1$

integration times corresponding to $n-1$ arcs. Thus, the augmented design variable vector is

$$\vec{X} = \begin{Bmatrix} \vec{X}_1(\tau_{0_1}) \\ \vdots \\ \vec{X}_n(\tau_{0_n}) \\ \tau_1 \\ \vdots \\ \tau_{n-1} \end{Bmatrix} \tag{3.44}$$

To maintain continuity in both position and velocity, the constraint vector, $\vec{F}(\vec{X})$, is of dimension $6(n-1)$, the same as was specified in the case of fixed-time multiple shooting scheme.

$$\vec{F}(\vec{X}) = \begin{Bmatrix} \vec{X}_1(\tau_{f_1}) - \vec{X}_2(\tau_{0_2}) \\ \vec{X}_2(\tau_{f_2}) - \vec{X}_3(\tau_{0_3}) \\ \vdots \\ \vec{X}_{n-2}(\tau_{f_{n-2}}) - \vec{X}_{n-1}(\tau_{0_{n-1}}) \\ \vec{X}_{n-1}(\tau_{f_{n-1}}) - \vec{X}_n(\tau_{0_n}) \end{Bmatrix} \tag{3.45}$$

Introduction of time as a new variable changes the banded matrix, $D\vec{F}(\vec{X})$, as each end reference state, $\vec{X}_i(\tau_{f_i})$ is a function of an integration time, τ_i. The matrix represented in Equation (3.43) is augmented due to the inclusion of time as a variable and is rewritten as

$$D\vec{F}(\vec{X}) = \begin{bmatrix} \phi(\tau_{f_1}, \tau_{0_1}) & -I_{6\times 6} & & \dot{\vec{X}}_1 & & \\ & \ddots & \ddots & & \ddots & \\ & & \phi(\tau_{f_n}, \tau_{f_{n-1}}) & -I_{6\times 6} & & \dot{\vec{X}}_{n-1} \end{bmatrix} \tag{3.46}$$

where $\dot{\vec{X}}_i$ represents the time derivatives of the end reference state, $\vec{X}_i(\tau_{f_i})$. The minimum norm solution is obtained as the Jacobian, $D\vec{F}(\vec{X})$, is a $6(n-1) \times 7n$ rectangular matrix. The algorithm is iteratively simulated until the desired level of tolerance is achieved for the constraint vector, $\vec{F}(\vec{X}) = \vec{0}$. At the end of the process,

new converged position and velocity states are determined for the patch points along with new times, τ_i between each pair of patch points.

3.4 Periodic Orbits in the CR3BP

A corrections scheme is applied for the construction of periodic orbits in the vicinity of the collinear Lagrangian points. Families of planar and three-dimensional orbits have been investigated over the past few decades [2] and a number of three-dimensional families bifurcate from planar families. One type of three-dimensional periodic orbit is a simple symmetric orbit in the set that comprises the 'halo' family of orbits [3]. Halo orbits have been of particular interest since 1978 when the International Sun-Earth Explorer-3 (ISEE-3) spacecraft was launched and inserted into a halo orbit in the vicinity of the Sun-Earth Lagrangian point, L_1 [10].

3.4.1 Construction of a Three-Dimensional Halo Orbit

A three-dimensional shooting algorithm is developed to compute three-dimensional halo orbits that exist in the vicinity of the collinear Lagrangian points. Because the differential equations are time-invariant, certain symmetric properties are observed. One straightforward approach to compute solutions involves a search for a periodic orbit that is symmetric across the $x-z$ plane. To initiate the construction of a family or orbits, an initial guess is generated by exploiting this symmetry property but is based on the linear model developed in Subsection 2.2.2. By introducing an out-of-plane step along z, a variable-time single-step corrections scheme is developed to determine the symmetric periodic halo orbits. Symmetry and perpendicular crossings are then employed as constraints to generate the orbits.

As noted previously, one strategy for construction of periodic orbits assumes perpendicular crossings at the $x-z$ plane [27]. Given an initial guess to initiate the corrections process, free variables are first identified. Assuming that the initial state

lies in the $\hat{x} - \hat{z}$ plane and the initial velocity is normal to the plane, the initial state is of the form

$$\vec{X}(\tau_0) = \begin{bmatrix} x_0 \\ 0 \\ z_0 \\ 0 \\ \dot{y}_0 \\ 0 \end{bmatrix} \tag{3.47}$$

where only three of six states are non-zero. A simple formulation is governed by fixing one initial condition and allowing the others to vary. An iterative process yields a perpendicular crossing, i.e., a half period for any three-dimensional halo orbit. Note that both the initial and the final states correspond to perpendicular crossings of the $x-z$ plane. To meet the final goal of a perpendicular crossing, both the final velocity in the x and z directions should be zero, i.e., $\dot{x} = \dot{z} = 0$ at the final crossing. Thus, the selection of a set of free variables allows one of the non-zero variables, $x_0, z_0, \dot{y}_0$, to be constrained. For example, to construct a halo orbit that crosses the x-axis at a specified location, constrain x_0 and then iterate to determine z_0 and $\dot{y}_0$. For simply periodic three-dimensional orbits that are symmetric across the $x - z$ plane, there are, consequently, three options for selecting free variables from the initial position and velocity states.

$$\vec{X}(\tau_0) = \begin{bmatrix} x_0 \\ \\ \dot{y}_0 \end{bmatrix} \; or \; \begin{bmatrix} z_0 \\ \\ \dot{y}_0 \end{bmatrix} \; or \; \begin{bmatrix} x_0 \\ \\ z_0 \end{bmatrix} \tag{3.48}$$

To demonstrate the algorithm, z_0 is selected as a free variable, along with $\dot{y}_0$. To ensure a perpendicular crossing at the next $\hat{x} - \hat{z}$ plane crossing, the constraint vector is carefully defined as,

$$\vec{F}(\vec{X}_{z_0, \dot{y}_0}) = \begin{bmatrix} \dot{x}_{\{y=0\}} \\ \\ \dot{z}_{\{y=0\}} \end{bmatrix} = \vec{0} \tag{3.49}$$

where the subscripts, $z_0, \dot{y}_0$, on $\vec{X}$ represent the design variable vector used in this formulation. The $D\vec{F}(\vec{X}_{z_0,\dot{y}_0})$ matrix is formulated by direct application of the chain rule

$$D\vec{F}(\vec{X}_{z_0,\dot{y}_0}) = \begin{bmatrix} \frac{\partial \dot{x}}{\partial z_0} + \frac{\partial \dot{x}}{\partial y}\frac{\partial y}{\partial z_0} & \frac{\partial \dot{x}}{\partial \dot{y}_0} + \frac{\partial \dot{x}}{\partial y}\frac{\partial y}{\partial \dot{y}_0} \\ \frac{\partial \dot{z}}{\partial z_0} + \frac{\partial \dot{z}}{\partial y}\frac{\partial y}{\partial z_0} & \frac{\partial \dot{z}}{\partial \dot{y}_0} + \frac{\partial \dot{z}}{\partial y}\frac{\partial y}{\partial \dot{y}_0} \end{bmatrix} \tag{3.50}$$

where

$$y(\dot{x}(\tau), \dot{z}(\tau), \tau) = 0 \tag{3.51}$$

serves as the stopping condition (in contrast to time) to ensure delivery precisely to the $x - z$ plane. In this formulation, the integration time has been implicitly defined as the time to cross the map, $\Sigma : y = 0$, i.e., half the period of the orbit. To evaluate the partials in Equation (3.50), Equation (3.51) is differentiated with respect to nondimensional time, τ, resulting in the following two expressions,

$$\frac{\partial y}{\partial \tau} + \frac{\partial y}{\partial \dot{x}}\frac{\partial \dot{x}}{\partial \tau} = 0 \tag{3.52}$$

$$\frac{\partial y}{\partial \tau} + \frac{\partial y}{\partial \dot{z}}\frac{\partial \dot{z}}{\partial \tau} = 0 \tag{3.53}$$

Consequently, the expressions for $\frac{\partial \dot{x}}{\partial y}$ and $\frac{\partial \dot{z}}{\partial y}$ are

$$\frac{\partial \dot{x}}{\partial y} = -\frac{\ddot{x}}{\dot{y}} \tag{3.54}$$

$$\frac{\partial \dot{z}}{\partial y} = -\frac{\ddot{z}}{\dot{y}} \tag{3.55}$$

The matrix of partials, $D\vec{F}(\vec{X})$, in Equation (3.50) is then rewritten in terms of the elements of the STM and Equations (3.54) - (3.55)

$$D\vec{F}(\vec{X}_{z_0,\dot{y}_0}) = \begin{bmatrix} \phi_{43} - \frac{\ddot{x}}{\dot{y}}\phi_{23} & \phi_{45} - \frac{\ddot{x}}{\dot{y}}\phi_{25} \\ \phi_{63} - \frac{\ddot{z}}{\dot{y}}\phi_{23} & \phi_{65} - \frac{\ddot{z}}{\dot{y}}\phi_{25} \end{bmatrix} \tag{3.56}$$

A more compact formulation is expressed in the form

$$D\vec{F}(\vec{X}_{z_0,\dot{y}_0}) = \begin{bmatrix} \phi_{43} & \phi_{45} \\ \phi_{63} & \phi_{65} \end{bmatrix} - \frac{1}{\dot{y}} \begin{Bmatrix} \ddot{x} \\ \ddot{z} \end{Bmatrix} \begin{bmatrix} \phi_{23} & \phi_{25} \end{bmatrix} \tag{3.57}$$

Similarly, using the other two possible design variable vectors in Equation (3.48) results in the following two alternative $D\vec{F}(\vec{X}$ matrices,

$$D\vec{F}(\vec{X}_{x_0,\dot{y}_0}) = \begin{bmatrix} \phi_{43} & \phi_{45} \\ \phi_{63} & \phi_{65} \end{bmatrix} - \frac{1}{\dot{y}} \begin{Bmatrix} \ddot{x} \\ \ddot{z} \end{Bmatrix} \begin{bmatrix} \phi_{21} & \phi_{25} \end{bmatrix} \tag{3.58}$$

$$D\vec{F}(\vec{X}_{x_0,z_0}) = \begin{bmatrix} \phi_{41} & \phi_{43} \\ \phi_{61} & \phi_{63} \end{bmatrix} - \frac{1}{\dot{y}} \begin{Bmatrix} \ddot{x} \\ \ddot{z} \end{Bmatrix} \begin{bmatrix} \phi_{21} & \phi_{23} \end{bmatrix} \tag{3.59}$$

Given an equal number of constraints and design variables, the $D\vec{F}(\vec{X})$ matrices in Equations (3.57) - (3.59) are all square matrices. The update equations for successive iterations are formulated for the three possible design variable vectors as follows

$$\vec{X}^{j+1}_{z_0,\dot{y}_0} = \begin{bmatrix} z_0^{j+1} \\ \dot{y}_0^{j+1} \end{bmatrix} = \vec{X}^{j}_{z_0,\dot{y}_0} + \delta\vec{X}^{j}_{z_0,\dot{y}_0} = \begin{bmatrix} z_0^{j} \\ \dot{y}_0^{j} \end{bmatrix} + \begin{bmatrix} \delta z_0^{j} \\ \delta\dot{y}_0^{j} \end{bmatrix} \tag{3.60}$$

$$\vec{X}^{j+1}_{x_0,\dot{y}_0} = \begin{bmatrix} z_0^{j+1} \\ \dot{y}_0^{j+1} \end{bmatrix} = \vec{X}^{j}_{x_0,\dot{y}_0} + \delta\vec{X}^{j}_{x_0,\dot{y}_0} = \begin{bmatrix} z_0^{j} \\ \dot{y}_0^{j} \end{bmatrix} + \begin{bmatrix} \delta z_0^{j} \\ \delta\dot{y}_0^{j} \end{bmatrix} \tag{3.61}$$

$$\vec{X}^{j+1}_{x_0,z_0} = \begin{bmatrix} z_0^{j+1} \\ \dot{y}_0^{j+1} \end{bmatrix} = \vec{X}^{j}_{x_0,z_0} + \delta\vec{X}^{j}_{x_0,z_0} = \begin{bmatrix} z_0^{j} \\ \dot{y}_0^{j} \end{bmatrix} + \begin{bmatrix} \delta z_0^{j} \\ \delta\dot{y}_0^{j} \end{bmatrix} \tag{3.62}$$

where the change in the design variables is then evaluated as

$$\delta\vec{X}^{j}_{z_0,\dot{y}_0} = \begin{bmatrix} \delta z_0^{j} \\ \delta\dot{y}_0^{j} \end{bmatrix} = -D\vec{F}(\vec{X}_{z_0,\dot{y}_0})\vec{F}(\vec{X}^{j}_{z_0,\dot{y}_0}) \tag{3.63}$$

$$\delta\vec{X}^{j}_{x_0,\dot{y}_0} = \begin{bmatrix} \delta x_0^{j} \\ \delta\dot{y}_0^{j} \end{bmatrix} = -D\vec{F}(\vec{X}_{x_0,\dot{y}_0})\vec{F}(\vec{X}^{j}_{x_0,\dot{y}_0}) \tag{3.64}$$

$$\delta\vec{X}^{j}_{x_0,z_0} = \begin{bmatrix} \delta x_0^{j} \\ \delta z_0^{j} \end{bmatrix} = -D\vec{F}(\vec{X}_{x_0,z_0})\vec{F}(\vec{X}^{j}_{x_0,z_0}) \tag{3.65}$$

Iteration produces a solution that meets the final constraints $\dot{x} = \dot{z} = 0$ and, consequently, produces a perpendicular crossing of the map, $\Sigma : y = 0$. Initial conditions

are selected such that the state lies on the map, $\Sigma : y = 0$ with an initial velocity only along the $\hat{y}$ unit direction vector. This results in the reference trajectory illustrated in Figure 3.6. After implementing the targeting scheme to construct a perpendicu-

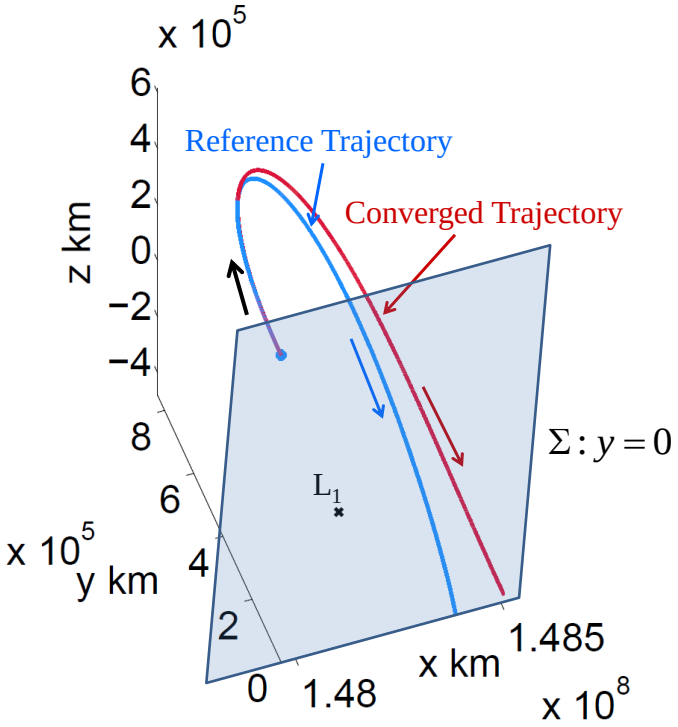

Figure 3.6. Targeting Perpendicular Crossing of the Map $\Sigma : y = 0$.

lar crossing of the map, $\Sigma : y = 0$, a converged trajectory is achieved that meets the constraints by varying the design parameters. For this illustration, the design parameters are z_0 and $\dot{y}_0$.

Once the trajectory has been corrected to deliver perpendicular crossings with a variable-time scheme, a complete halo orbit is available by propagating the new initial conditions over precisely twice the integration time that is required for a half orbit. A three-dimensional view of the halo orbit, relative to the Lagrangian point, L_1, as well as the Earth is represented in Figure 3.7(b). Note that the Earth has been scaled $\times 6$ for visualization purposes. The three planar projections offer a better understanding of the general shape of the orbit as is apparent in Figures 3.7(a), 3.7(c) and 3.7(d).

As noted from Figure 3.7(c), this halo orbit possesses a relatively large out-of-plane

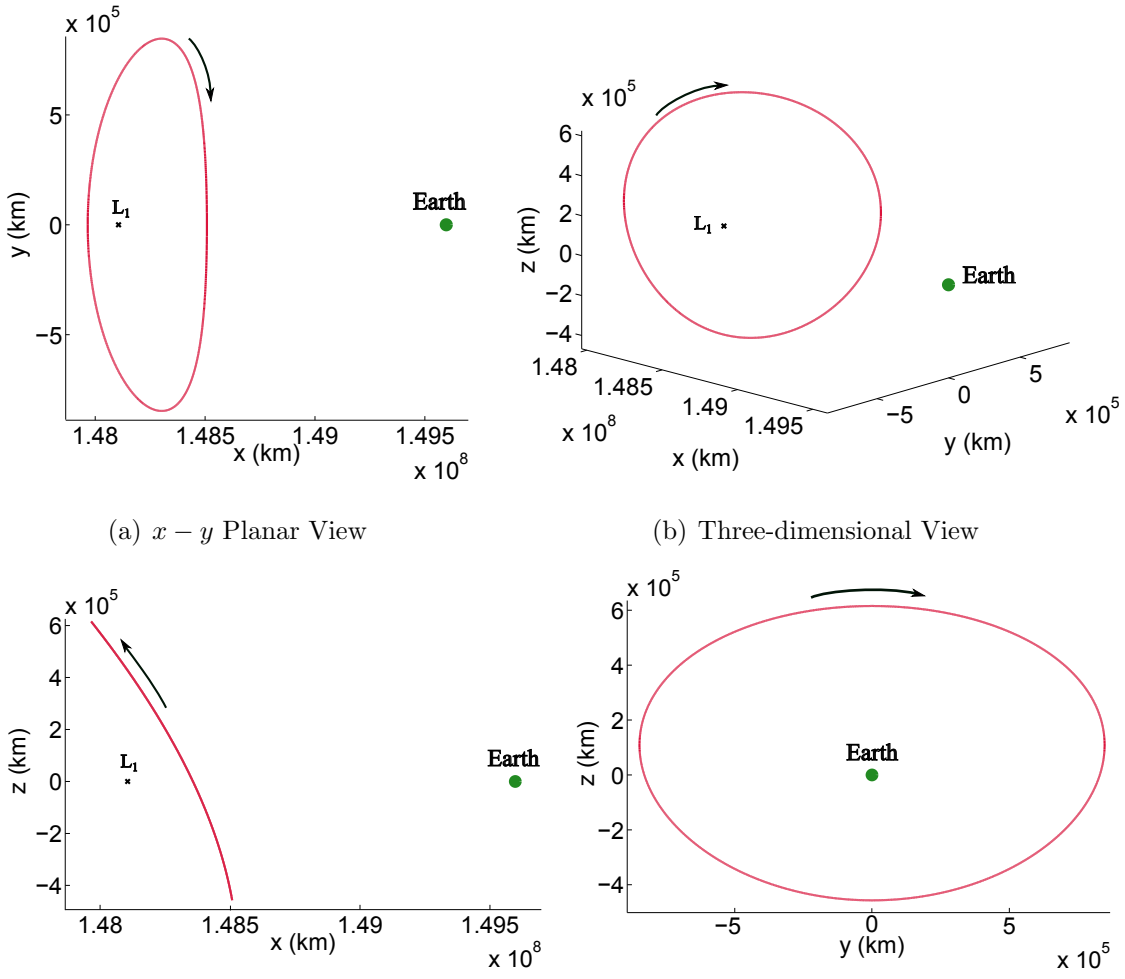

(a) $x - y$ Planar View

(b) Three-dimensional View

(c) $x - z$ Planar View

(d) $x - z$ Planar View

Figure 3.7. Sun-Earth System L_1 Halo Orbit

z amplitude. The in-plane component of the halo orbit has amplitudes A_x = 350,000 km and A_y = 900,000 km, whereas the out-of-plane amplitude is A_z = 600,000 km. Nearby halo orbits can now be explored to construct a family of trajectories.

3.4.2 Halo Families in the Vicinity of L_1/L_2 Collinear Lagrangian Points

Construction of a three-dimensional, symmetric, periodic halo orbit using the corrections process is further extended to investigate the dynamical regime near the collinear Lagrangian points. Family members in the vicinity of the converged orbit are computed using a slope-based continuation scheme. A three-dimensional view of a selected subset of periodic trajectories that are members of the Sun-Earth L_1 northern halo family appears in Figure 3.8. Continuation is employed to determine the

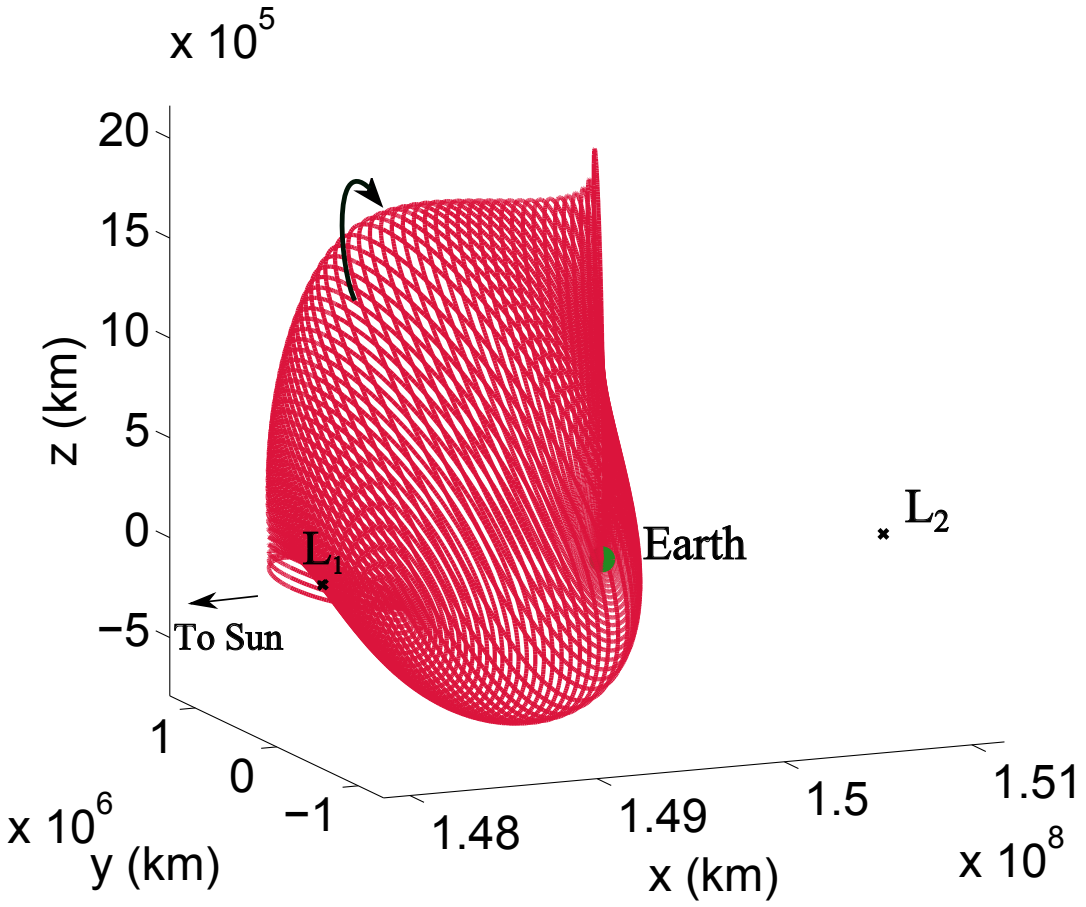

Figure 3.8. Periodic Trajectories in the Sun-Earth L_1 Northern Halo Family

northern and the southern family members respectively. Planar projections of orbits from the Sun-Earth L_1 northern halo family are plotted in Figure 3.9. Similarly, a

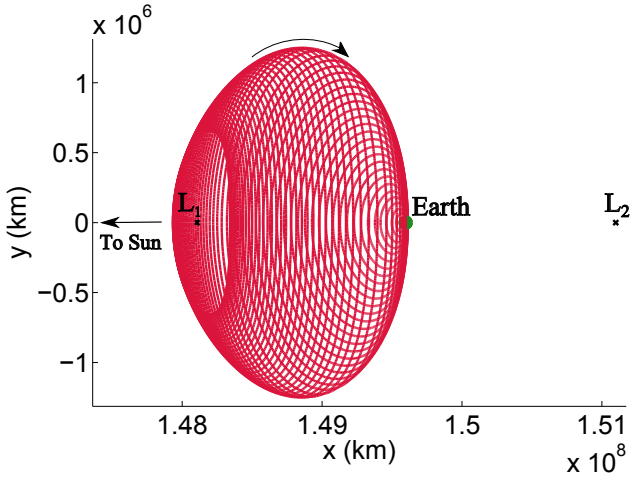

(a) $x - y$ Planar View

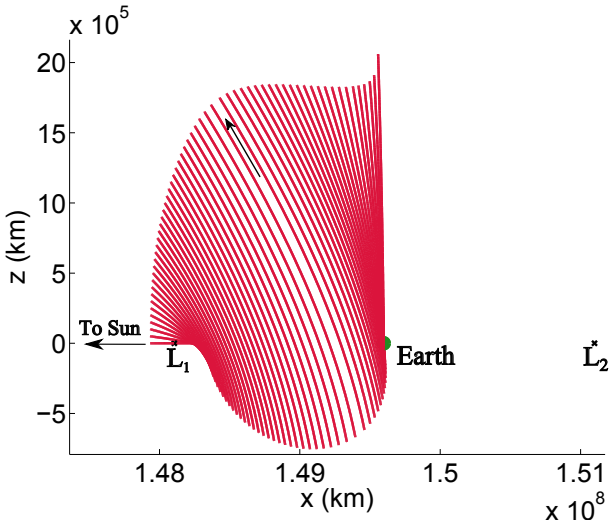

(b) $x - z$ Planar View

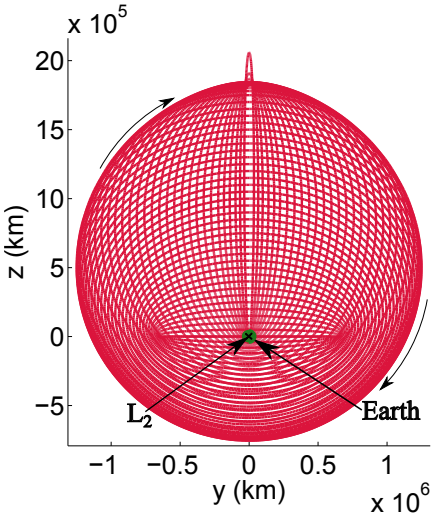

(c) $x - z$ Planar View

Figure 3.9. Projections of the Sun-Earth L_1 Northern Halo Family

selected subset of periodic trajectories that are members of the Sun-Earth L_1 southern halo family are illustrated in Figures 3.10 and 3.11.

Moving to the Sun-Earth L_2 Lagrangian point, a subset of northern halo family is illustrated in Figures 3.12 and 3.13.

A selected subset of periodic trajectories that are members of the Sun-Earth L_2 southern halo family are illustrated in Figures 3.14 and 3.15. All four families of

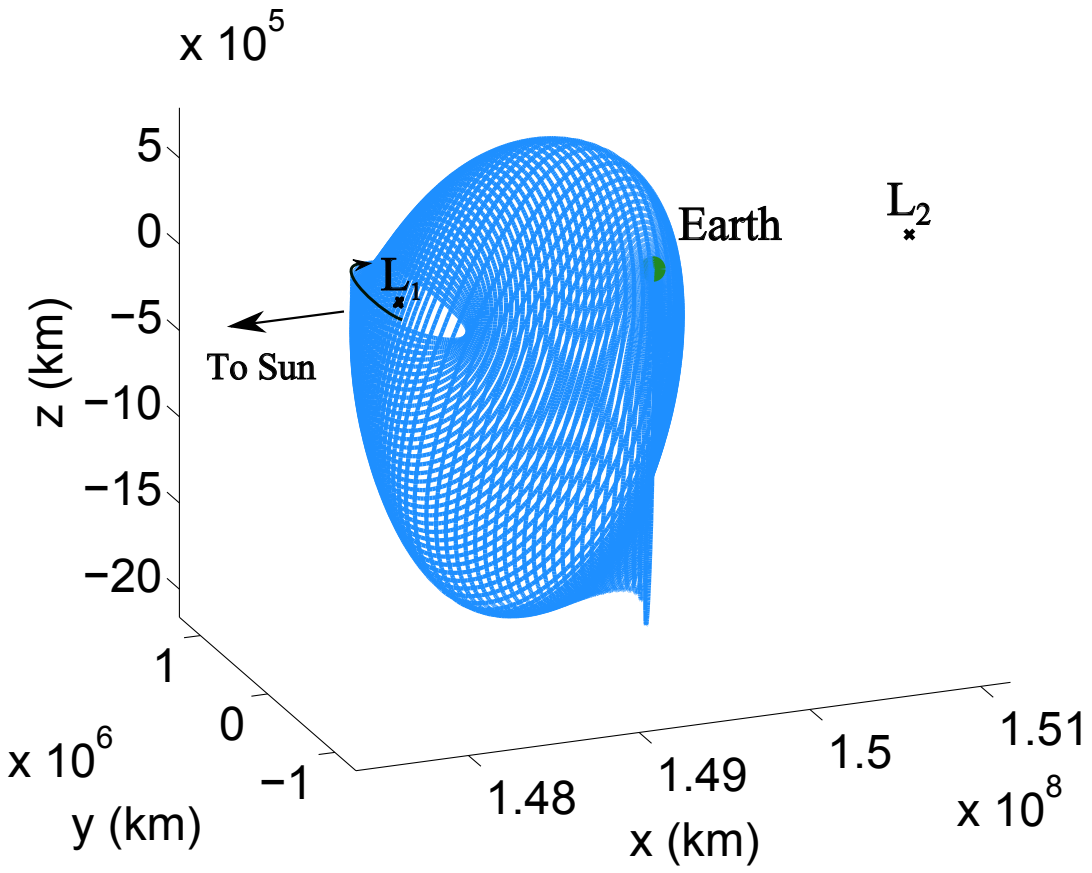

Figure 3.10. Periodic Trajectories in the Sun-Earth L_1 Southern Halo Family

periodic orbits are combined into one figure for comparison. An illustration for all four families, encompassing Sun-Earth L_1 and L_2 northern and southern halo family members, is represented in Figures 3.16 and 3.17. Note that these orbits are based on natural dynamics within the circular restricted three-body regime. To further investigate the effects of external forces that also act upon a spacecraft, deriving an extended dynamical model, based upon the specifications of the force, is relatively straightforward.

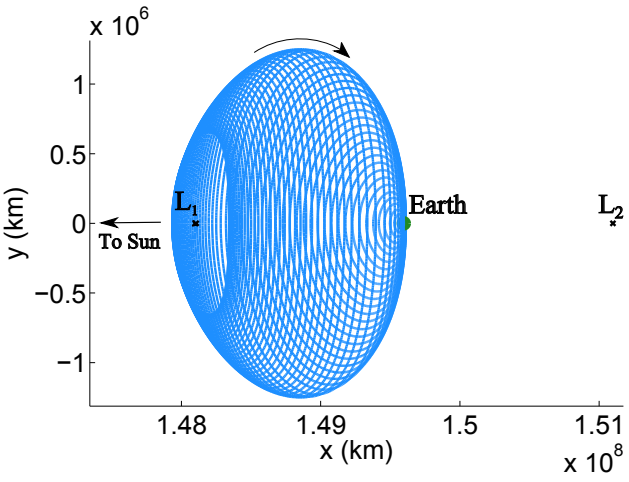

(a) $x - y$ Planar View

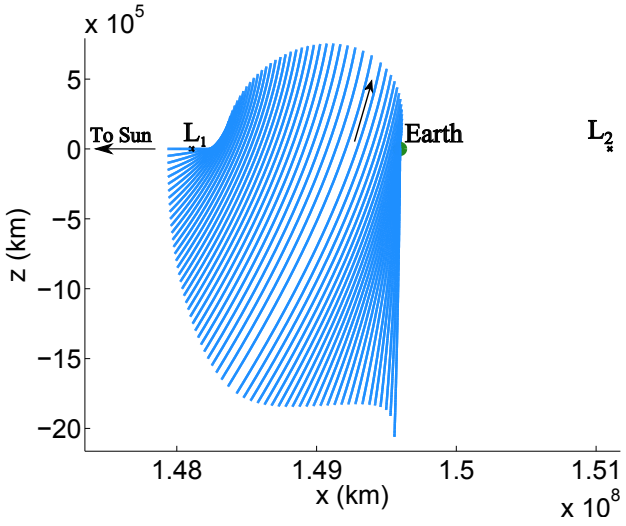

(b) $x - z$ Planar View

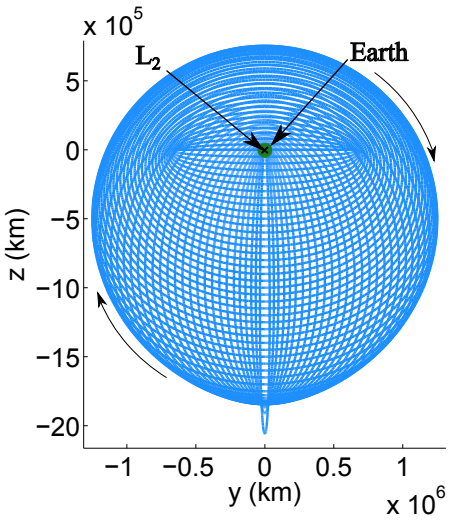

(c) $x - z$ Planar View

Figure 3.11. Projections of the Sun-Earth L_1 Southern Halo Family

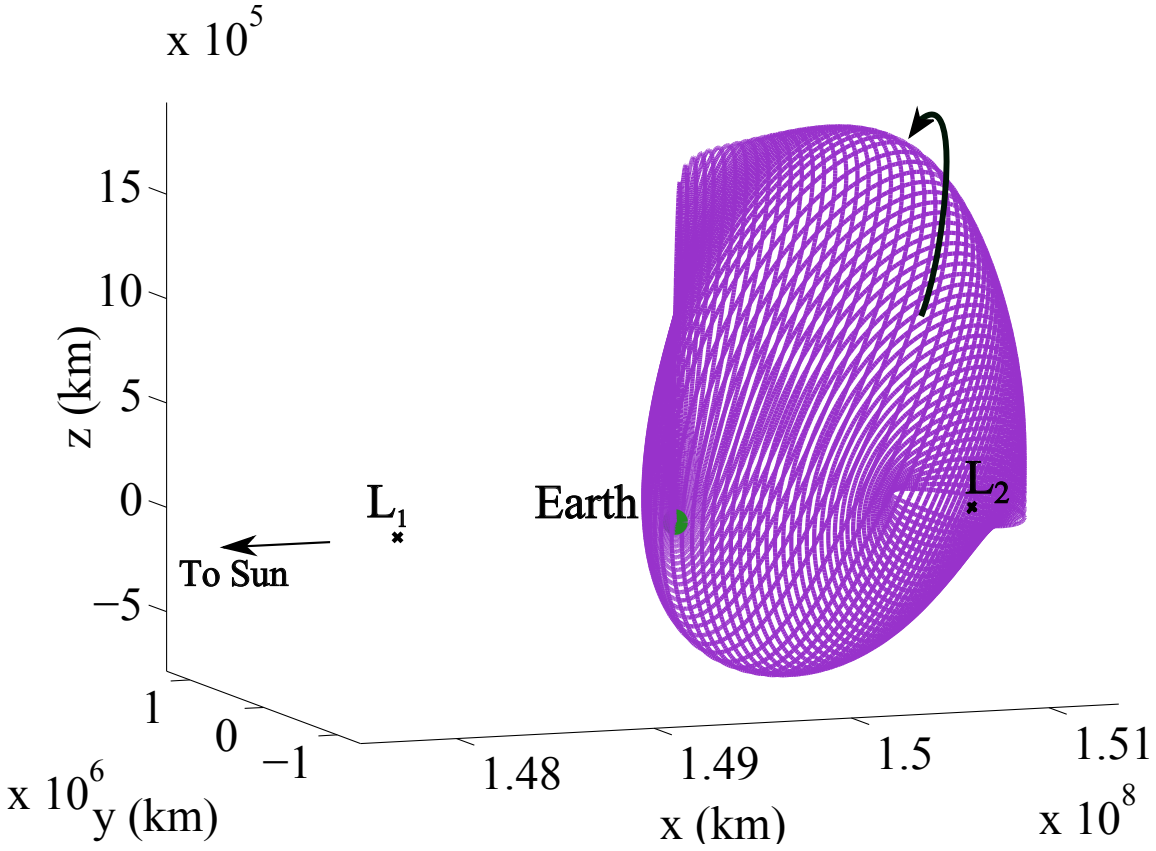

Figure 3.12. Periodic Trajectories in the Sun-Earth L_2 Northern Halo Family

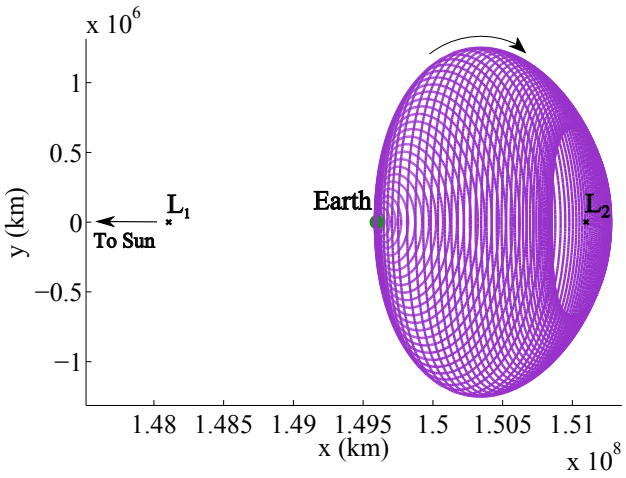

(a) $x - y$ Planar View

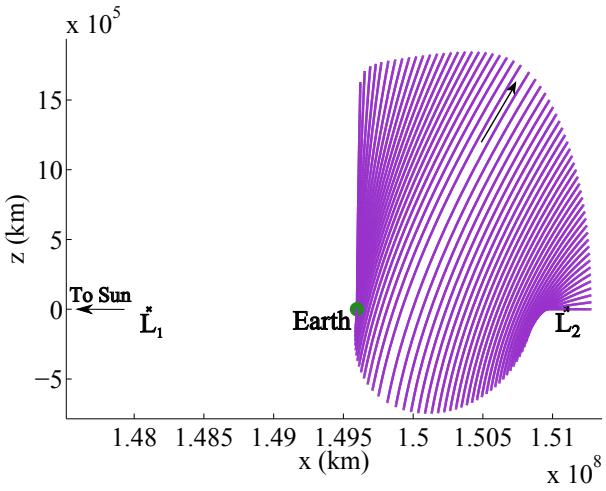

(b) $x - z$ Planar View

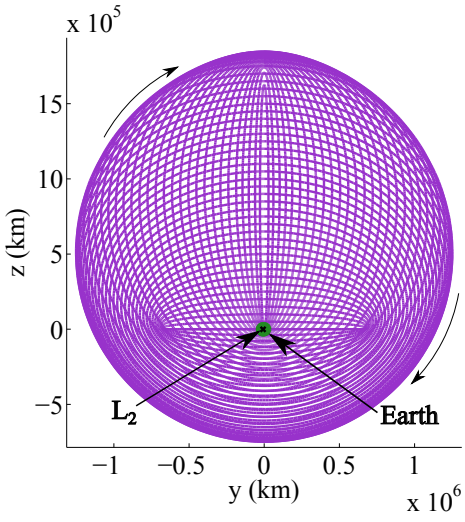

(c) $x - z$ Planar View

Figure 3.13. Projection of the Sun-Earth L_2 Northern Halo Family

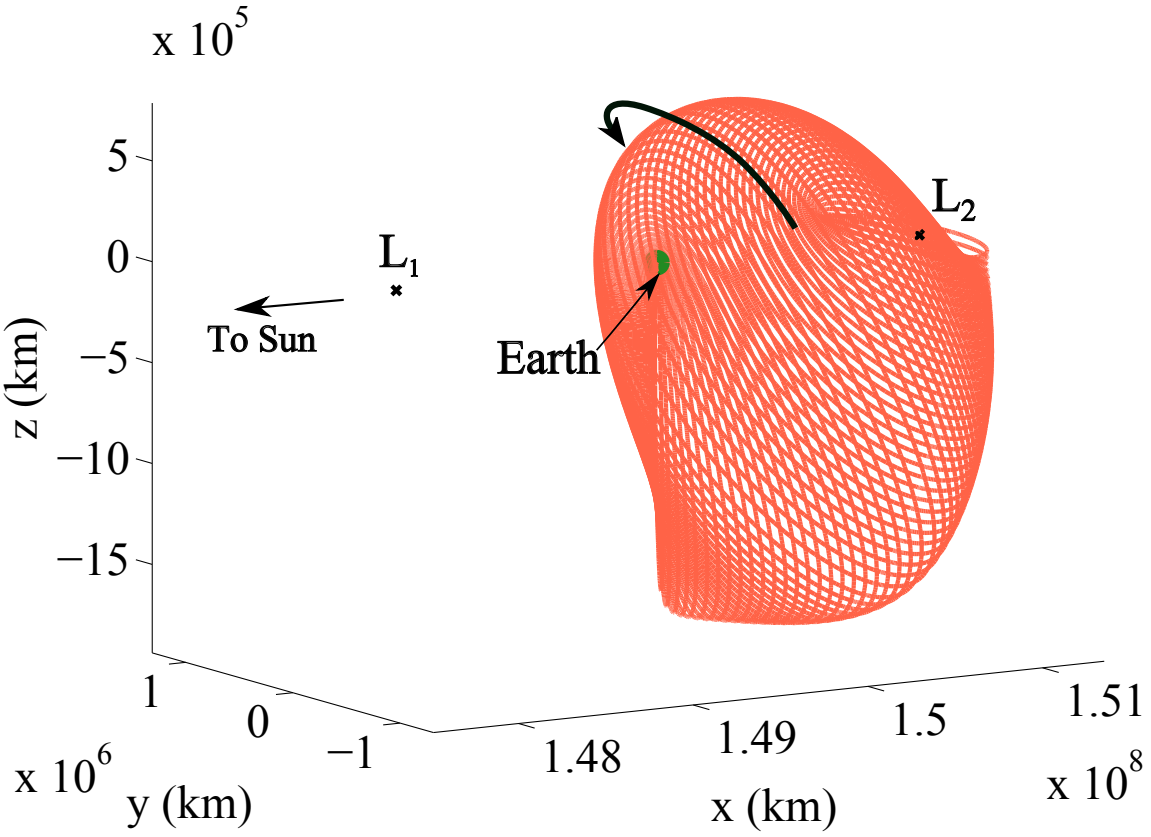

Figure 3.14. Periodic Orbits in the Sun-Earth L_2 Southern Halo Family

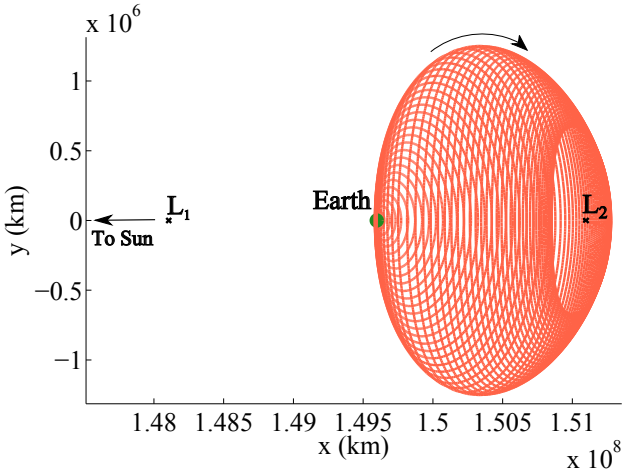

(a) $x - y$ Planar View

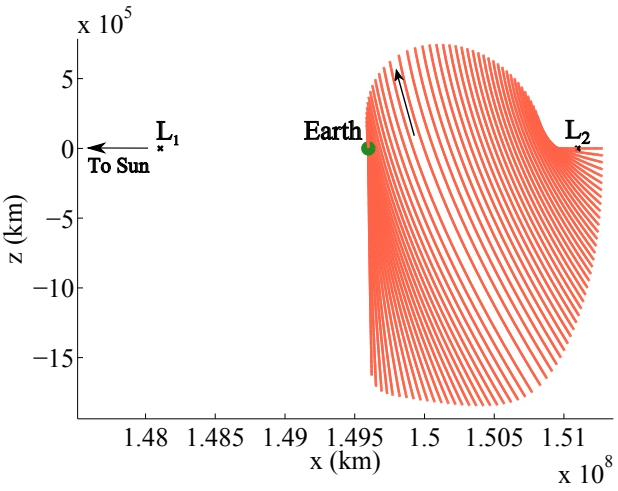

(b) $x - z$ Planar View

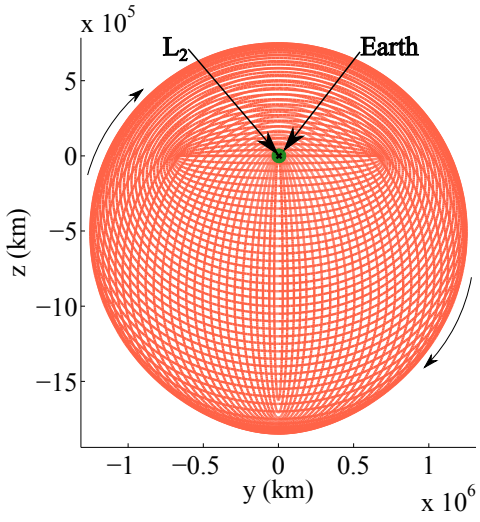

(c) $x - z$ Planar View

Figure 3.15. Projections of the Sun-Earth L_2 Southern Halo Family

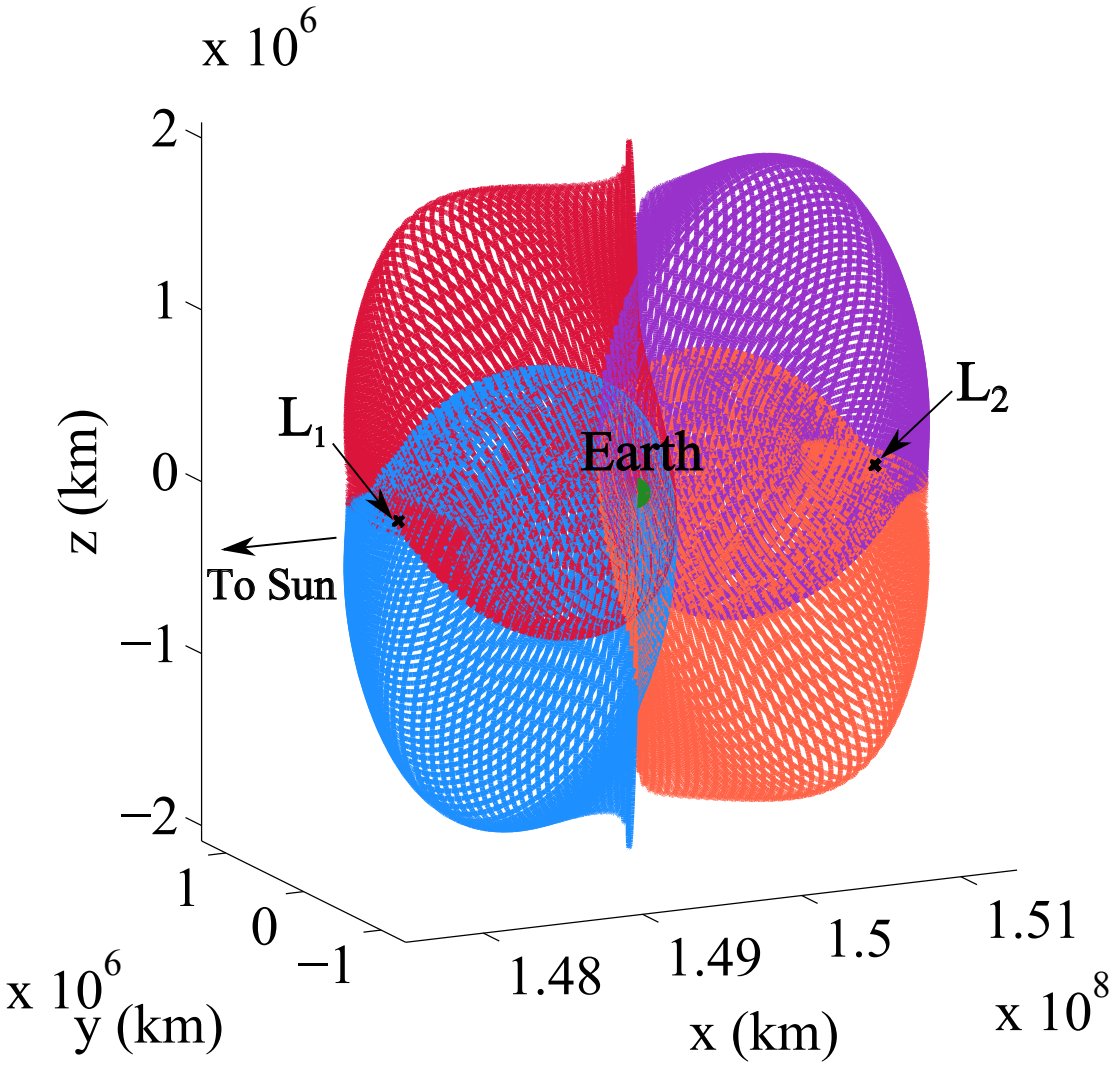

Figure 3.16. Periodic Trajectories in the Sun-Earth L_1 and L_2 Halo Families

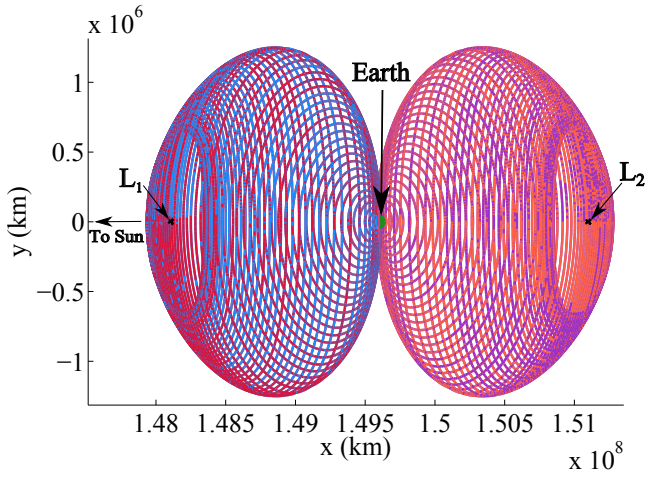

(a) $x - y$ Planar View

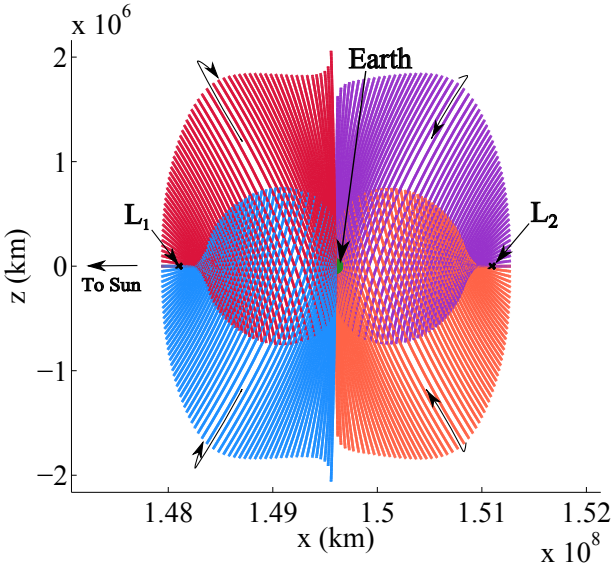

(b) $x - z$ Planar View

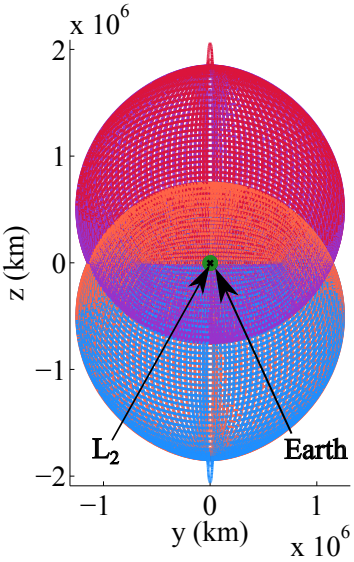

(c) $x - z$ Planar View

Figure 3.17. Projections of the Sun-Earth L_1 and L_2 Halo Families

4. BACKGROUND: SOLAR SAILS

The exploration of solar sails to move throughout the solar system is based on a dynamical concept for harnessing the energy carried by photons from the Sun in the form of momentum. Conventional propulsion systems for maneuvers deplete propellant over time and, thus, the life of the spacecraft is limited. The operational lifetime can be increased by increasing the amount of propellant; such an option may not be feasible or practical, however. Alternatively, solar sails potentially offer indefinite maneuvering capability by using photons from the Sun as a means of propulsion. Incorporating a solar sail model within the context of the circular restricted three-body problem extends the design options. A model that includes a solar sail force within the framework of the Solar Sail Circular Restricted Three-Body Problem (SS-CR3BP) is derived. The design space in the SS-CR3BP is then explored.

4.1 Solar Sail Model

Although serious planning to explore the solar system using solar sails has gained momentum only in last few decades, the concept of harnessing solar radiation pressure (SRP) was first studied in 1873 by James Clerk Maxwell [13]. But, a Russian physicist, Peter Lebedew, initially conducted laboratory experiments to demonstrate the effects of SRP in 1900 [14]. Further interest in solar sailing technology was developed when Konstantin Tsiolkovsky, the Soviet astronautics pioneer, and Fredrickh Tsander wrote of *"using tremendous mirrors of very thin sheets"* and *"using the pressure of sunlight to attain cosmic velocities"*[1] [28], [15]. Carl Wiley was the first American engineer to propose the idea of solar sailing. He went on to propose orbit raising as well as

[1]Collin R. McInnes, *Solar Sailing: Technology, Dynamics and Mission Applications* (Chichester, United Kingdom: Springer - Praxis, 1999), 2.

spiraling inwards towards the Sun [29]. In 1958, Rickard Garwin from the IBM Watson Laboratory also deduced that solar sails require no propellant and are continuously accelerated once deployed [30]. He also recognized that this continuous acceleration leads to large velocity changes over a longer time interval. Garwin is also credited with coining the term *"solar sailing"* [29].

With the advancement of the technology linked to deployable structures, along with thin films and the development of the Space Shuttle in the 1970's, the focus shifted from theory to increased laboratory testing. A NASA-funded investigation in 1974, conducted at the Battelle laboratories in Ohio, delivered a promising demonstration of solar sailing [16]. The NASA investigation and other studies conducted in the mid-1970's gained worldwide interest. Eventually, a European analysis at the Center National d'Etudes Spatiales (CNES) in Toulouse, France offered an assessment of a potential deep space mission incorporating solar sails [13]. Later in the decade, specifically in 1979, Robert Staehle of the Jet Propulsion Laboratory formed the World Space Foundation (WSF) in California. Two years later, the Union pour la Promotion de la Propulsion Photonique (U3P) emerged in Toulouse. The Solar Sail Union of Japan (SSUJ) was formed in 1982 and soon joined with WSF and U3P to promote the long term prospects of solar sails.

With further technological advancements, the first ever ground deployment of a solar sail was conducted by the German Space Agency, Deutsches Zentrum für Luft- und Raumfahrt (DLR), in collaboration with the European Space Agency (ESA) and a smaller German company, INVENT GmbH, in December of 1999 at Köln, Germany [31]. The sail was 20m x 20m and a deployed model appears in Figure 4.1. As part of solar sail development programs at both DLR and ESA, a smaller, in-orbit demonstration is currently planned for 2013 [33]. NASA-funded programs aimed toward development of solar sail technology were completed in 2005 by two firms, ATK Space Systems of Goleta, California and L'Garde Inc., of Tustin California. L'Garde used inflatable boom technology to deploy the boom. In contrast, ATK employed a coilable graphite boom that would uncoil and support the sail structure. The 20m x

Figure 4.1. Solar Sail Ground Deployment Test by DLR [32].

20m sails were tested at the NASA Glenn Research Center's Plum Brook Station in Sandusky, Ohio [34] but neither achieved Technology Readiness Level (TRL) 6.

In 2010, the first spacecraft to demonstrate the use of solar radiation pressure as a source of propulsion in flight was launched by the Japanese Space Agency, JAXA. The solar sail spacecraft, Interplanetary Kite-craft Accelerated by Radiation Of the Sun (IKAROS), is a square sail, 20m in diameter, and 7.5 μm thick created from polyimide film. A model of the IKAROS spacecraft, as well as the actual deployed spacecraft, appears in Figure 4.2. IKAROS successfully demonstrated both a propulsive force of 1.12 mN and attitude control capabilities [19]. Thus, IKAROS paved a pathway for further development in the field of solar sail technology.

In the United States, NASA, in collaboration with the Planetary Society, is developing the NanoSail-D (a 'CubeSat' project) based on solar sail technology; later, the project was actually renamed LightSail. A laboratory-based, deployed NanoSail-D

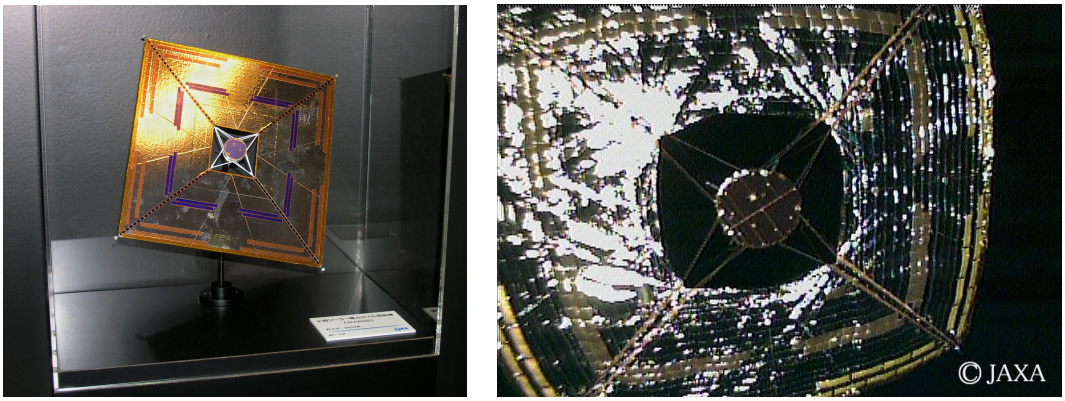

(a) Model of IKAROS Spacecraft [35] (b) IKAROS after Solar Sail Deployment [36]

Figure 4.2. IKAROS Solar Sail Spacecraft.

appears in Figure 4.3. NanoSail-D was onboard the SpaceX Falcon 1 in August 2008 which was designed to test the capabilities in low-Earth orbit. The Falcon 1 launch was unsuccessful, and both the rocket and the payload were lost. Now LightSail-1 is planned to test the propulsion capabilities of the spacecraft at an altitude of 800 km. The Planetary Society had initially planned on launching LightSail-1 in 2012.

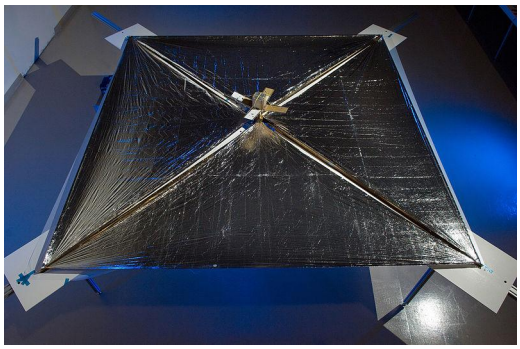

Figure 4.3. Fully Deployed NanoSail-D [37]

As of November 06, 2012, no further update is available [38]. Upon the successful testing of LightSail-1, LightSail-2 is planned for launch to further enhance the solar sail based control strategy. It is expected that LightSail-3 will follow with a proposed mission that incorporates an insertion into an orbit near the Sun-Earth Lagrangian

point, L_1. LightSail-3 will provide early detection and warning of geomagnetic storms capable of damaging power and communication systems on Earth [18]. Thus, the recent rejuvenation of interest in harnessing the potential of a solar sail has accelerated the development of technology. The success of the IKAROS mission was a significant breakthrough and, thus, interest continues in further testing and the validation of solar sail technology.

4.2 Solar Radiation Pressure Force

The transfer of momentum from photons, originating at the Sun in the form of bundles of energy, to a solar sail gives rise to Solar Radiation Pressure (SRP) as mentioned by J. C. Maxwell [13]. The pressure from the continuous bombardment of radiation onto the sail results in the acceleration of the sail. The energy flux (W), carried by photons, is used to calculate the amount of momentum transfer, hence, the SRP acting on the sail. Thus, the SRP exerted on the sail is expressed as

$$P = \frac{W}{c} \tag{4.1}$$

where P is the solar radiation pressure and c is the speed of light. For an ideal sail, i.e., a perfectly reflecting sail, the total radiation pressure, P, is twice that of the value in Equation (4.1). The factor of two is due to the momentum transferred to the sail by the incident photons as well as the momentum transferred as a result of perfect reflection. A schematic representation appears in Figure 4.4. where $\hat{n}$ is the unit direction vector parallel to the normal to the surface of the sail and $\hat{r}_{13}$ is the unit vector directed along the Sun-sail line. The angle between the unit vector directed along the Sun-sail line, $\hat{r}_{13}$, and the unit vector parallel to the sail normal, $\hat{n}$, is represented by angle α. The incident photons result in a force, $\vec{F}_I$, along the $\hat{r}_{13}$ unit vector and the reflected photons provide the sail with a force along a direction that is normal to $\hat{r}_{13}$. Thus, a net resultant force, $\vec{F}_{Sail}$, is directed parallel to the sail normal, $\hat{n}$, evident in Figure 4.4.

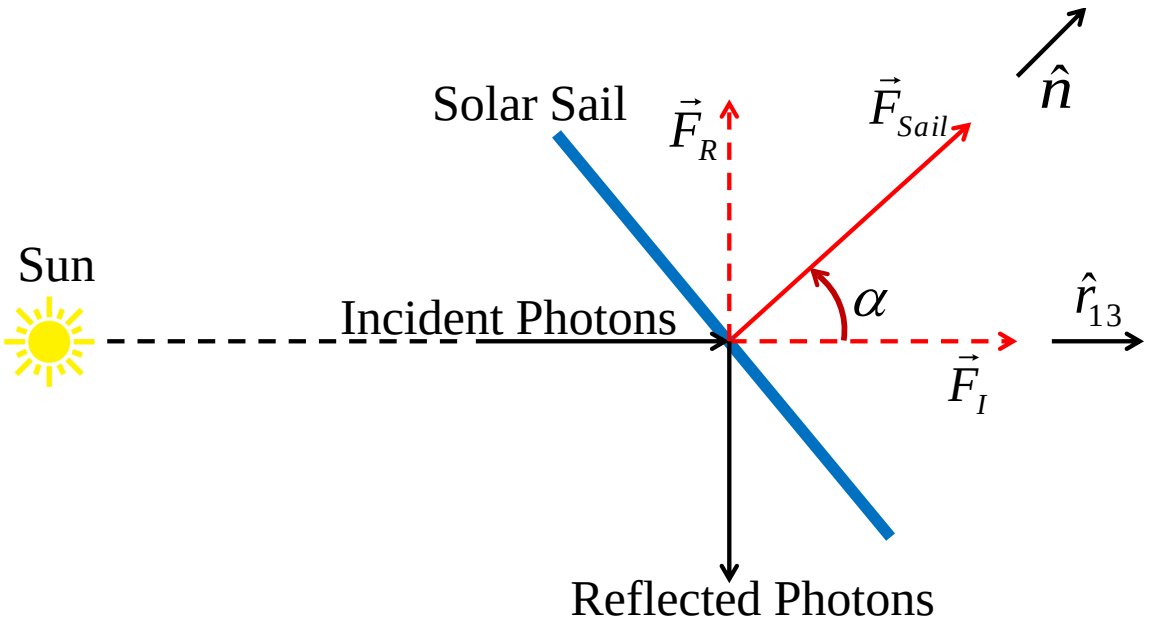

Figure 4.4. Net Force, $\vec{F}_{sail}$, Acting on a Perfectly Reflecting Solar Sail

The solar flux, W, is a a function of the distance of the solar sail from the Sun. Thus, the general expression for solar flux, W, is modeled as

$$W = W_{1AU}\left(\frac{r_1 + r_2}{r_{13}}\right)^2 \tag{4.2}$$

where W_{1AU} is the solar flux experienced by the solar sail at a distance of one astronomical unit (AU), i.e., in the vicinity of the Earth. In addition, $(r_1 + r_2)$ is the distance between the primaries, in this case, the distance between the Sun and the Earth, and r_{13} is the distance between the Sun and the solar sail-based spacecraft. The amount of solar radiation pressure acting on the sail at an approximate distance equal to 1 AU (distance from the Sun to the Earth) is available and an acceptable value for the solar flux, W at 1 AU is

$$W_{1AU} = 1368\ \frac{\text{J}}{\text{m}^2\ \text{s}} \tag{4.3}$$

Consider the required solar sail size based on the desired acceleration that can be achieved as a result of solar flux at 1 AU. The total solar radiation pressure acting

on a perfectly reflecting solar sail at an approximate distance of 1 AU is evaluated using Equation (4.1) and results in the value,

$$P_{Sail} = 2(P) = 9.12 \times 10^{-6} \ \frac{\text{N}}{\text{m}^2} \tag{4.4}$$

Assume that an experimental sail with the same size and comprised of the same material as IKAROS is operating at 1 AU. The experimental sail is assumed to be flat, rigid and perfectly reflecting. Thus, the total force acting on the experimental sail due to solar radiation pressure is

$$F_{Ideal} = P_{Sail} * A_{Sail} = 1.824 \text{ mN} \tag{4.5}$$

From the data collected, IKAROS demonstrated a propulsive force of 1.12 mN [19]. Thus, for the experimental sail, the efficiency, ϵ, is calculated as

$$\text{Efficiency } (\epsilon) = \frac{F_{Actual}}{F_{Ideal}} \times 100 = 61.4 \ \% \tag{4.6}$$

In addition, based on the information available, it is possible to calculate a sail acceleration, a_{Sail}, given a total mass (consistent with the IKAROS spacecraft) that is 310 kg [39],

$$a_{Sail} = \frac{F_{Actual}}{mass_{Total}} = 3.61 \ \frac{\mu\text{m}}{\text{s}^2} \tag{4.7}$$

To be capable of carrying the total load, i.e., mass of the spacecraft, payload and the sail, an ideal sail must be of a certain pre-specified dimensions. Such analysis appears in Figure 4.5 for an ideal sail. The required sail edge length assumes that the sail is square in design and a pre-specified sail acceleration capability. Based on the sail loading and the acceleration that can be produced, the requirements for the edge length are indicated. To investigate the sail loading capabilities, the load factor, σ, is introduced,

$$\sigma = \frac{m_{Total}}{A_{Sail}} = \frac{310 \text{ kg}}{200 \text{ m}^2} = 1550 \ \frac{\text{g}}{\text{m}^2} \tag{4.8}$$

From the acceleration of the experimental sail, as well as the efficiency, an analysis relating sail edge length and mass to the acceleration level appears in Figure 4.6. Recall that the acceleration experienced by the experimental sail is 3.61 μm/s^2 as

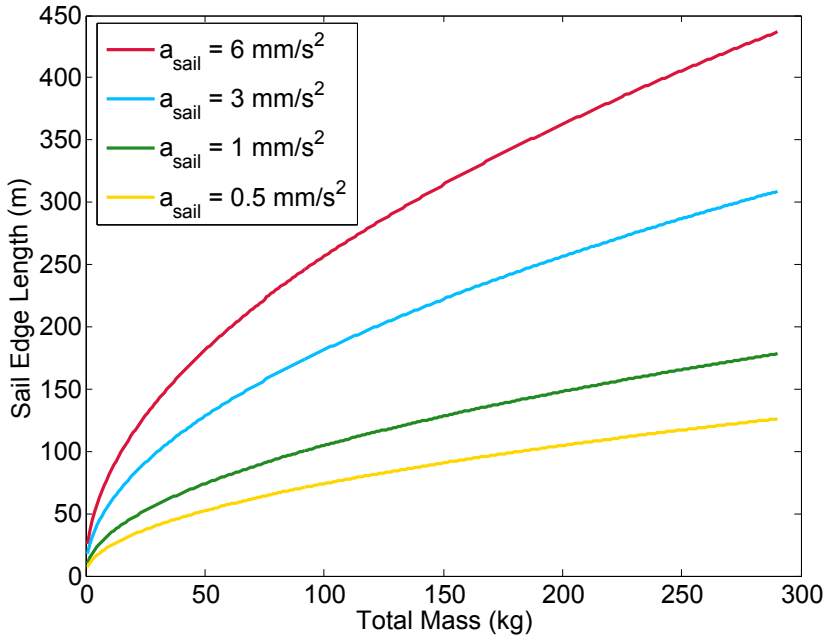

Figure 4.5. Required Sail Edge Length based on Sail Loading and Sail Acceleration for an Ideal Sail.

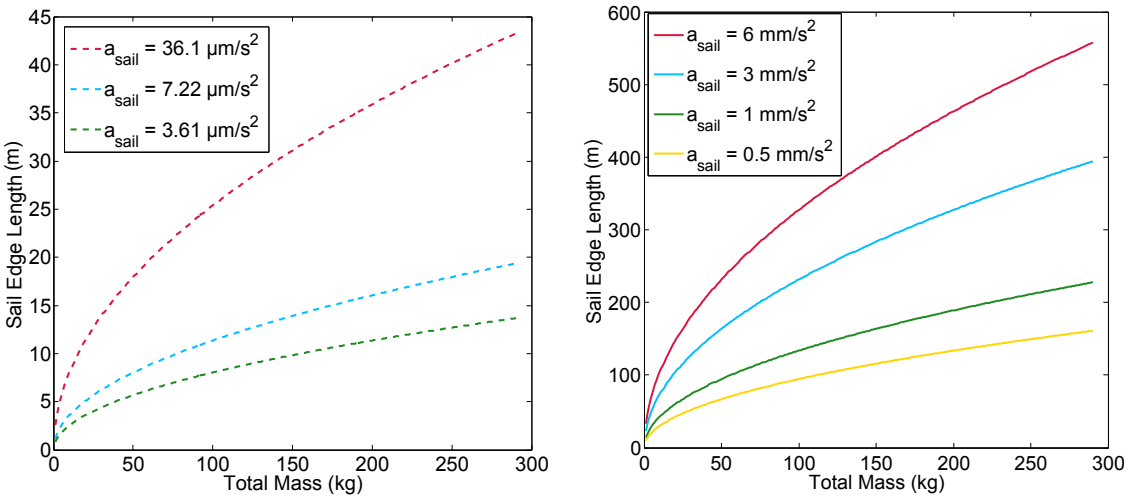

(a) Analysis for Lower Sail Accelerations

(b) Analysis for Higher Sail Accelerations

Figure 4.6. Sail Edge Length requirements based on the Efficiency (ϵ) = 61.4 % of the Experimental Sail.

noted in Equation (4.7). Though the acceleration, A_{Sail}, is small, it still is significant. The plots in Figure 4.6(a) compare the sail size requirements for a sail with an

acceleration level equal to that of IKAROS to sails with accelerations that are two and ten times that of IKAROS. From the figure, it is easily inferred that the size and efficiency of the sail plays a huge role in the overall acceleration level that the sail can achieve for a given total mass. Thus, to increase the solar sail acceleration, the load factor must be reduced. The decrease in the load factor is achieved by significantly increasing the size of the sail.

Continuing investigations into solar sail technologies aid in improving the characteristics associated with solar sails, thereby increasing efficiency. Recall that the efficiency demonstrated by the sails on a spacecraft similar to the IKAROS spacecraft and operating at 1 AU is 61.4 %. In Figure 4.7, the sail size requirements as a function of acceleration and total mass are apparent to demonstrate an efficiency of 90%. As an example, assume that the total mass of the spacecraft (payload and sail)

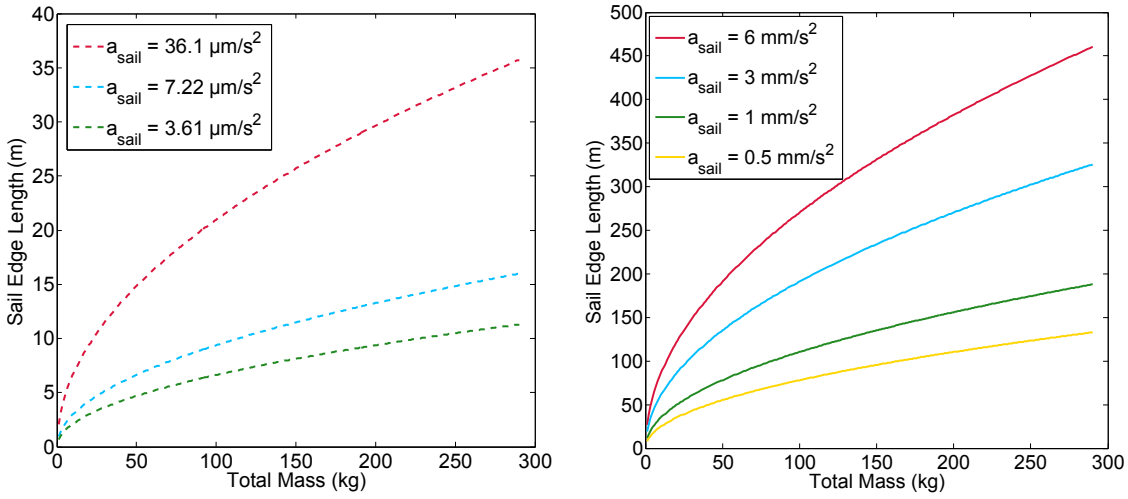

(a) Analysis for Lower Sail Accelerations (b) Analysis for Higher Sail Accelerations

Figure 4.7. Sail Edge Length Requirements based on the Efficiency (ϵ) = 90 %.

is 150 kg. Given that the experimental sail is 61.4 % efficient (same as IKAROS), to achieve an acceleration of 36.1 μm/s^2 due to SRP, the approximate dimensions that are required equal 30m $\times$ 30m, i.e., an area of 900 m^2 (Figure 4.6(a)). Similarly, if the experimental sail is 90 % efficient, the same acceleration would require the sail

to be appoximately 25m $\times$ 25m, i.e., area of 625 m^2 (Figure 4.7(a)). Thus, reducing the required sail area by 275 m^2. In summary, a 90 % efficient sail of dimensions 30m $\times$ 30m is capable of supporting an increased total load of 200 kg and achieve an acceleration of 36.1 $\mu m/s^2$ due to SRP.

In another scenario, assume that the mission specification requires the sail acceleration to be 3 mm/s^2 and capable of supporting a total mass of 200 kg. The experimental sail, with an efficiency of 61.4 % (Figure 4.6(b)), would require the sail to be of dimension 320m $\times$ 320m, i.e., an area of 102,400 m^2. Increasing the efficiency of the experimental sail to 90 % would require a sail of dimension 270 m $\times$ 270 m as apparent from Figure 4.7(b). Thus, reducing the required sail area by 29,500 m^2. Alternatively, if a 90 % efficient sail is still of dimension 320m $\times$ 320m, the sail loading capacity is increased to 300 kg. Thus, increasing the sail mass-to-area ratio to 2.93 gm/m^2.

The analysis summarized in this chapter is fundamental and serves as the basic requirements that the sail must meet to carry a certain load and achieve a desired sail acceleration. The investigation is extended to incorporate a change in the solar sail acceleration level as a result of a change in the sail's position from the source of the radiation pressure, i.e., the Sun. Incorporating the sail characteristics in the equations of motion for a spacecraft is formulated by inclusion of the force model due to the solar radiation pressure. Further examination is completed to analyze the behavior of a sailcraft in the restricted three-body problem, thus, formulating a new hybrid model labeled as the Solar Sail Circular Restricted Three-Body Problem (SS-CR3BP).

5. SOLAR SAIL IN THE CIRCULAR RESTRICTED THREE-BODY PROBLEM (SS-CR3BP)

A concept for harnessing the energy carried by photons from the Sun in the form of momentum extends the solar sail model into the CR3BP framework. The momentum transfer from the incident and reflected photons acting on a sail result in a net force that continuously accelerates the vehicle. Thus, a mathematical model is formulated to incorporate the solar sail in the CR3BP. The model is consistent with previous analyses by McInnes [13], Nuss [40] and McInnes [41]. Certain assumptions pertaining to the solar sail and the intercepted photons are specified in the development of the model. The location of the collinear Lagrangian points as a result of the inclusion of the acceleration due to solar radiation pressure force is investigated.

5.1 Sail Orientation

In the development of a force model, a mathematical description of the direction of force relative to the sail orientation is a key kinematical relationship. The quantity of photons encountered by the solar sail is directly related to the sail orientation with respect to the direction of photon flow. Thus, the orientation of the sail governs the acceleration produced on the solar sail by the incident and the reflected protons. A schematic representation appears in Figure 5.1. The orientation of the solar sail is defined based on two angles with respect to an orthogonal reference frame as seen in the figure. The reference frame of interest is formed from the unit vector, $\hat{z}$, the direction that remains fixed in both the inertial and the rotating frame, as well as the unit vector, $\hat{d}$, along the Sun-sail line. The angle α represents the angle between the Sun-sail unit direction, $\hat{d}$, and the direction vector parallel to the surface normal of the sail, $\hat{n}$. The angle α is also represented in Figure 4.4; α is frequently denoted

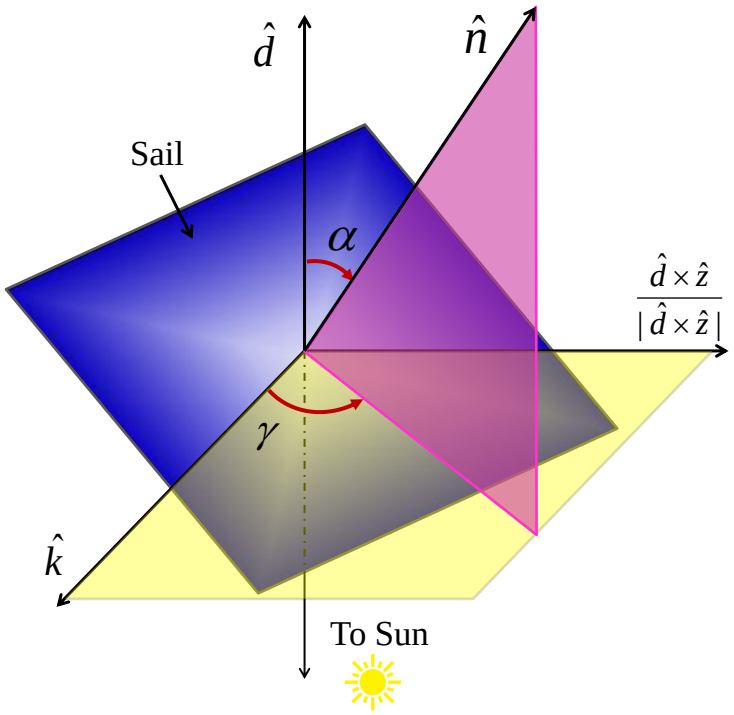

Figure 5.1. Solar Sail Angle Definitions.

as the cone angle or the nutation angle of the solar sail relative to the Sun-sail line. The second angle in Figure 5.1 is represented as the angle γ. The angle γ is defined between the plane spanned by the unit vectors, $\hat{d}$ and $\hat{n}$ lie and the reference unit direction vector, $\hat{k}$. The vector $\hat{k}$ is defined as

$$\hat{k} = \frac{(\hat{d} \times \hat{z}) \times \hat{d}}{|(\hat{d} \times \hat{z}) \times \hat{d}|} \tag{5.1}$$

In a sense, γ defines the angle by which the plane spanned by the unit vectors, $\hat{d}$ and $\hat{n}$ has precessed; thus, the angle γ is also the precession angle or the clock angle. Based on the currently available technology, the maximum rate of rotation for attitude control is equal to 0.02 deg/s for a three-axis spacecraft equipped with sails that use sail panel rotations [42]. This attitude control rate is referenced to offer insight into the relative time that is required for a desired maneuver. It is vital to note that if the sail orientation angles, α and γ, remain constant relative to the Sun in the rotating frame, the orientation will change in the inertial frame. Thus, the hardware

must continually reorient the sail with respect to the inertial frame. To maintain the orientation of a sail relative to the Sun in the inertial frame, the sail must reorient at approximately one degree per day to maintain an orbit with an estimated period of 180 days.

Prior to introducing a force acting on a sail in the dynamical model, it is necessary to mathematically express the sail orientation in the rotating frame coordinates. The unit direction vector, $\hat{n}$, as indicated in Figure 5.1, is parallel to the surface normal of the sail. The vector $\hat{n}$, in terms of the rotating frame coordinates $\hat{x}$, $\hat{y}$, and $\hat{z}$ is defined as

$$\hat{n} = n_x\hat{x} + n_y\hat{y} + n_z\hat{z} \tag{5.2}$$

where the magnitudes, n_x, n_y, and n_z are evaluated as

$$n_x = Cos\alpha\frac{(x+\mu)}{|\vec{d}|} - Sin\alpha Cos\gamma\frac{z(x+\mu)}{|(\vec{d}\times\hat{z})\times\vec{d}|} + Sin\alpha Sin\gamma\frac{y}{|\vec{d}\times\hat{z}|} \tag{5.3}$$

$$n_y = Cos\alpha\frac{(y)}{|\vec{d}|} - Sin\alpha Cos\gamma\frac{yz}{|(\vec{d}\times\hat{z})\times\vec{d}|} - Sin\alpha Sin\gamma\frac{(x+\mu)}{|\vec{d}\times\hat{z}|} \tag{5.4}$$

$$n_z = Cos\alpha\frac{z}{|\vec{d}|} + Sin\alpha Cos\gamma\frac{[y^2+(x+\mu)^2]}{|(\vec{d}\times\hat{z})\times\vec{d}|} \tag{5.5}$$

and the denominators in Equations (5.3) - (5.4) are

$$|\vec{d}| = \sqrt{(x+\mu)^2+y^2+z^2} \tag{5.6}$$

$$|(\vec{d}\times\hat{z})\times\vec{d}| = \sqrt{(x+\mu)^2+y^2} \tag{5.7}$$

$$|\vec{d}\times\hat{z}| = \sqrt{(x+\mu)^2z^2+y^2z^2+((x+\mu)^2+y^2)^2} \tag{5.8}$$

Expressing $\hat{n}$ in the rotating coordinate frame assists in successfully incorporating the force and the orientation information into the force model for the CR3BP to formulate the new set of differential equations that reflect the SS-CR3BP. Note, $\hat{d}$ is always the direction of photons from the Sun. In Figure 5.1, it is also clear that for an angle equal to zero, $\alpha = 0^o$, the maximum quantity of photons are intercepted by the solar sail surface. Thus, at the particular orientation identified as $\alpha = 0^o$, the solar sail experiences the maximum acceleration due to solar radiation pressure. Consequently, as the sail angle increases, the quantity of photons that are encountered by the solar

sail decreases, lowering the acceleration of the sail. At a sail angle equal to $\alpha = 90^o$, the sail is edge-on to the flow of photons and, thus, the solar sail acceleration receives no contribution due to the solar radiation pressure. The sail orientation described by $\alpha = 90^o$ reflects a net force on the spacecraft equal to that in the CR3BP model.

5.2 Mathematical Expression for Solar Sail Acceleration

The derivation of the acceleration due to solar radiation pressure is based on three critical assumptions and emerges as a function of the sail angles, α and γ. For preliminary analysis, it is assumed that the solar sail is ideal and flat with a perfectly reflecting surface, i.e., there is no absorption or refraction but only reflection due to the incident photons. Thus, all the photons experience perfectly elastic collisions and "bounce off" the surface of the solar sail as demonstrated in Figure 4.4. It is also assumed that the source of photons is the primary, P_1, which is the Sun. Thus, the flow of incident photons is parallel to the Sun-sail line and the resultant force is parallel to the sail surface normal. The total net force acting on the solar sail is expressed as a function of angle, α, in the form

$$\vec{F}_{Sail} = \epsilon P_{Sail} A_{Sail} Cos^2\alpha \ \hat{n} \tag{5.9}$$

where ϵ is the efficiency of the sail. Recall, in Equation (4.8), the load factor, σ, is defined as the ratio of the total mass supported by the sail to the total surface area of the sail. The load factor, σ, is now used to rewrite the solar sail acceleration from Equation (5.9),

$$\vec{a}_{sail} = \epsilon \frac{P_{sail}}{\sigma} Cos^2\alpha \ \hat{n} \tag{5.10}$$

Thus, a new quantity is also defined as the solar sail characteristic accelerations, a^*. The characteristic acceleration is the acceleration at 1 AU and, for the particular orientation, such that the sail angle is equal to zero, i.e., $\alpha = 0^o$, or

$$a^* = \epsilon \frac{P_{sail}}{\sigma} = \epsilon \frac{9.12}{\sigma[\mathrm{g/m^2}]} \ [\mathrm{mm/s^2}] \tag{5.11}$$

The characteristic acceleration, a^*, serves as a reference value for comparison with general solar sail accelerations. Consistent with the definition of σ, a characteristic mass-to-area ratio, $\sigma*$, is defined that produces a force equal and opposite to the force acting on the sail due to solar radiation pressure, i.e.,

$$\sigma^* = \frac{P_{Sail}\ r_{13}}{\tilde{G}m_1} \tag{5.12}$$

Recall that $\tilde{G}$ is the dimensional universal gravitational constant, the quantity r_{13} is the dimensional scalar distance of the third body, i.e., the solar sail spacecraft, from the first primary, P_1, the Sun and m_1 is the mass of the first primary, P_1. The introduction of the sail lightness parameter, β, is appropriate as

$$\beta = \frac{\sigma^*}{\sigma} \tag{5.13}$$

The sail lightness parameter, also frequently denoted the sail loading parameter, is the ratio of the acceleration due to the solar radiation pressure to the classical solar gravitational acceleration [13]. Thus, the solar sail acceleration expression in Equation (5.10) for efficiency equal to one, i.e., $\epsilon = 1$, is rewritten as

$$\vec{a} = \beta\frac{\tilde{G}m_1}{r_{13}}Cos^2\alpha\ \hat{n} \tag{5.14}$$

Now, rewriting Equation (5.14) in terms of nondimensional quantities

$$\ddot{\vec{r}}_{Sail} = \beta\frac{(1-\mu)}{d^2}Cos^2\alpha\ \hat{n} \tag{5.15}$$

where $\ddot{\vec{r}}_{Sail}$ is the nondimensional acceleration of the solar sail due to solar radiation pressure. Recall that d is the nondimensional distance of the solar sail from the Sun. The model for the nondimensional solar sail acceleration in Equation (5.15) is now easily included to augment the equations of motion in the classical CR3BP.

5.3 Augmented Equations of Motion in the CR3BP

The dimensional vector differential equation governing the motion of P_3 under the gravitational influence of P_1 and P_2 in the classical CR3BP is derived and appears

in Equation (2.13). Augmenting the force to include the contribution due to the solar radiation pressure acting on the spacecraft results in the following dimensional equation,

$$m_3 {}^I\vec{r}_3{}'' = -\frac{\tilde{G}m_3m_1}{r_{13}^3}\vec{r}_{13} - \frac{\tilde{G}m_3m_2}{r_{23}^3}\vec{r}_{23} + \beta\frac{\tilde{G}m_3m_1}{r_{13}^2}Cos^2\alpha\ \hat{n} \tag{5.16}$$

To avoid round-off errors associated with the numerical integration and to generalize the results, Equation (5.16) is rewritten in a nondimensional form,

$${}^I\ddot{\vec{\rho}} = -\frac{(1-\mu)}{d^3}\vec{d} - \frac{\mu}{r^3}\vec{r} + \beta\frac{(1-\mu)}{d^2}Cos^2\alpha\ \hat{n} \tag{5.17}$$

Thus, Equation (5.17) represents the nondimensional differential equation governing the motion of P_3 under the gravitational influence of P_1 and P_2 as well as the influence of solar radiation pressure on P_3 given that P_3 represents a spacecraft with a solar sail and P_1 acts as the source of the solar radiation pressure. Substituting the kinematic expression from the previously derived result in Equation (2.18) into Equation (5.17) yields the following three second-order nondimensional scalar differential equations of motion for the spacecraft, P_3, equipped with a solar sail, under the gravitational influence of the two primaries, P_1 and P_2 and the solar radiation pressure from P_1, the Sun, i.e.,

$$\ddot{x} - 2\dot{y} - x = -\frac{(1-\mu)(x+\mu)}{d^3} - \frac{\mu(x-1+\mu)}{r^3} + a_{Sail-x} \tag{5.18}$$

$$\ddot{y} + 2\dot{x} - y = -\frac{(1-\mu)y}{d^3} - \frac{\mu y}{r^3} + a_{Sail-y} \tag{5.19}$$

$$\ddot{z} = \frac{(1-\mu)z}{d^3} - \frac{\mu z}{r^3} + a_{Sail-z} \tag{5.20}$$

where a_{Sail-x}, a_{Sail-y}, and a_{Sail-z} are the components of the nondimensional solar sail acceleration expressed in rotating coordinates acting along $\hat{x}$, $\hat{y}$, and $\hat{z}$ unit direction vectors, respectively. The expressions for the acceleration components are as follows

$$a_{Sail-x} = \beta\frac{(1-\mu)}{d^2}Cos^2\alpha\ n_x \tag{5.21}$$

$$a_{Sail-y} = \beta\frac{(1-\mu)}{d^2}Cos^2\alpha\ n_y \tag{5.22}$$

$$a_{Sail-z} = \beta\frac{(1-\mu)}{d^2}Cos^2\alpha\ n_z \tag{5.23}$$

The scalar magnitudes are the same as those in Equations (5.3) - (5.5). Based on the definition of the pseudo-potential function in Equation (2.22), a condensed form of Equations (5.18) - (5.20) is rewritten as

$$\ddot{x} = 2\dot{y} + \Omega_x^* + a_{Sail-x} \tag{5.24}$$

$$\ddot{y} = -2\dot{x} + \Omega_y^* + a_{Sail-y} \tag{5.25}$$

$$\ddot{z} = \Omega_z^* + a_{Sail-z} \tag{5.26}$$

The mathematical model represented in Equations (5.24) - (5.26) is nonlinear and coupled, thus, no closed-form solution exists. Collinear equilibrium points exist in the SS-CR3BP and the behavior of a solar sail equipped spacecraft is analyzed in the vicinity of the L_1 and L_2 Lagrangian points. The subsequent analysis offers new regions for exploration using the solar sails.

5.4 Collinear Lagrangian Points: Analysis in the SS-CR3BP

The inclusion of the acceleration terms due to solar radiation pressure in the CR3BP model modifies the dynamical characteristics associated with the system. As a result, collinear 'displaced' Lagrangian points emerge as new equilibrium locations. The collinear, displaced Lagrangian points are also termed the collinear artificial Lagrangian points. The parameters associated with the sail allow to vary the locations of the collinear Lagrangian point along the $\hat{x}$ unit direction vector, in turn, reaching locations that might be significant from a scientific prospective.

5.4.1 Displaced Collinear Lagrangian Points

To explore the physical location of the displaced collinear Lagrangian points within the context of a rotating frame, recall that both the relative acceleration and the

relative velocity are zero. Consequently, the mathematical model in Equations (5.24) - (5.26) reduces to

$$0 = \Omega_x^* + a_{Sail-x} \tag{5.27}$$

$$0 = \Omega_y^* + a_{Sail-y} \tag{5.28}$$

$$0 = \Omega_z^* + a_{Sail-z} \tag{5.29}$$

These relationships are also expressed as the gradient of the potential function, i.e., $-\vec{\nabla}\Omega$, such that,

$$-\vec{\nabla}\Omega = \beta\frac{(1-\mu)}{d^2}Cos^2\alpha\ \hat{n} \tag{5.30}$$

The location of the collinear points along the x-axis, i.e., $y = 0$ and $z = 0$, is determined from the cross product of Equation (5.30) with $\hat{n}$ gives [41], that is,

$$-\vec{\nabla}\Omega \times \hat{n} = \vec{0} \tag{5.31}$$

For the displaced Lagrangian points along the x-axis, it is apparent from Equation (5.31) that the equilibrium points exist for

$$\hat{n} = \frac{-\vec{\nabla}\Omega}{|-\vec{\nabla}\Omega|} = \pm\hat{x} \tag{5.32}$$

Thus, Equation (5.32) implies that the sail angle is equal to zero, $\alpha = 0^o$. The equation governing the location of the displaced collinear Lagrangian point is derived from Equation (5.18) after incorporating the appropriate orientation of the sail. The assumption that $y = z = 0$, as well as the fact that the acceleration and velocity components are equal to zero, yields

$$0 = x - \frac{(1-\mu)(x+\mu)}{d^3} - \frac{\mu(x-1+\mu)}{r^3} + \beta\frac{(1-\mu)}{d^2} \tag{5.33}$$

The expression in Equation (5.33) is rearranged into a more compact form as

$$0 = x_{L_i} - \frac{(1-\beta)(1-\mu)(x_{L_i}+\mu)}{d_{L_i}^3} - \frac{\mu(x_{L_i}-1+\mu)}{r_{L_i}^3} \tag{5.34}$$

where, the subscripts are consistent with those employed in Equation (2.37) for the formulation in the C3BBP. Note that, for sail a lightness parameter equal to zero, i.e,

$\beta = 0$, Equation (5.34) is equivalent to Equation (2.37). Thus, the expression reduces to the equation in the CR3BP, implying that the location of the collinear equilibrium points in the classical CR3BP is simply a special case of the SS-CR3BP analysis, one for which the value of $\beta = 0$.

A schematic representing the locations of the displaced collinear Lagrangian points as a function of the sail lightness parameter, β, is plotted in Figure 5.2. As the

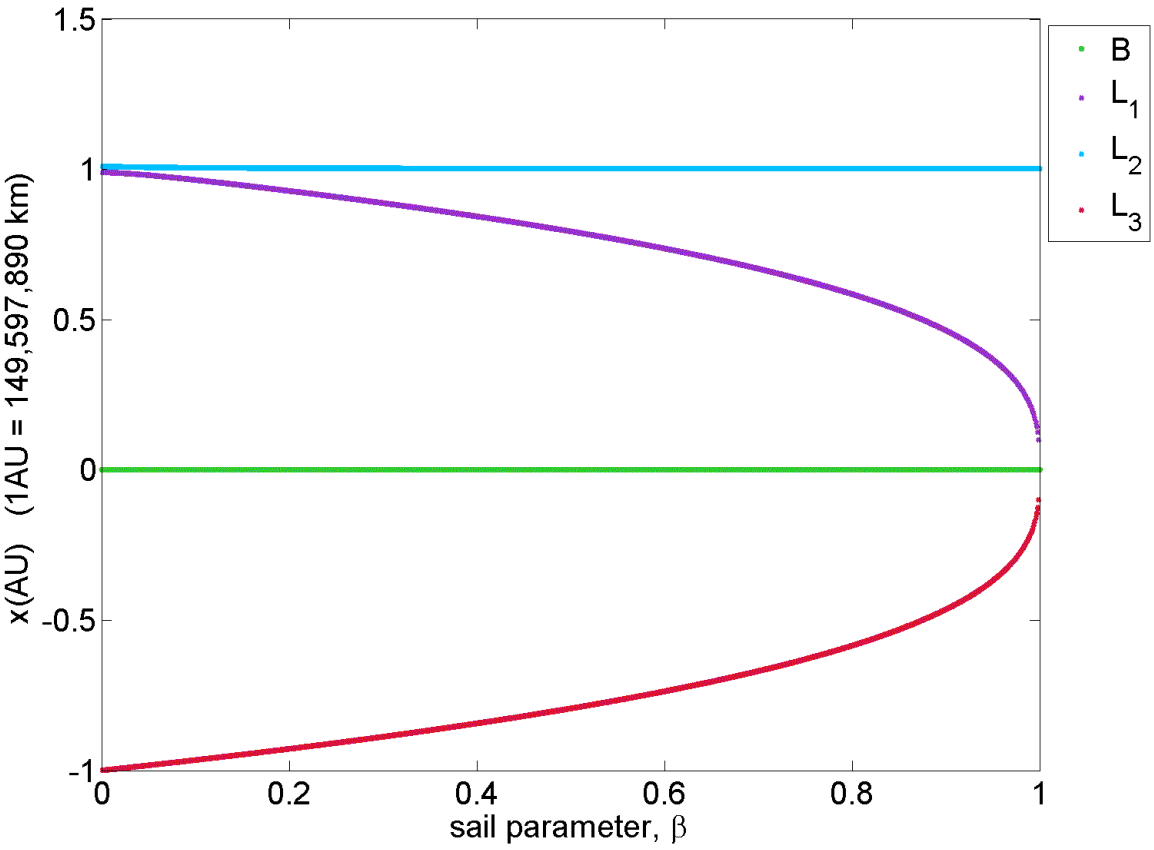

Figure 5.2. Displaced Sun-Earth Collinear Lagrangian Points Progression.

value of β approaches zero, the Lagrangian points shift to their location within the context of the classical CR3BP. Alternatively, as the value of β approaches one, the Lagrangian points, L_1 and L_2, both tend to asymptotically approach the barycenter, B. Clearly, all the collinear points tend to shift closer to the primary, P_1. As a result

of variations in the sail lightness parameter, β, the displacement of L_1 and L_2 along the Sun-Earth line is much more significant as compared to the displacement of L_3. Thus, the existence of displaced, artificial Lagrangian points broadens the options for exploration within the SS-CR3BP. Further investigation into the potential existence of periodic orbits in the vicinity of the displaced Lagrangian points is warrantied.

5.4.2 Behavior Near the Displaced Lagrangian Points in the SS-CR3BP

To obtain stability information corresponding to the displaced Lagrangian points, differential equations are linearized relative to the equilibrium points. The linear stability analysis is then based on the first-order variational equations. As a result of the incorporation of the accelerations of the solar sail due to the solar radiation pressure from the Sun, Equations (2.50) - (2.52) are rewritten as

$$\ddot{\xi} - 2\dot{\eta} = (\Omega^*_{xx} + a^*_{Sail-x_x})\xi + (\Omega^*_{xy} + a^*_{Sail-x_y})\eta + (\Omega^*_{xz} + a^*_{Sail-x_z})\zeta \tag{5.35}$$

$$\ddot{\eta} + 2\dot{\xi} = (\Omega^*_{yx} + a^*_{Sail-y_x})\xi + (\Omega^*_{yy} + a^*_{Sail-y_y})\eta + (\Omega^*_{yz} + a^*_{Sail-y_z})\zeta \tag{5.36}$$

$$\ddot{\zeta} = (\Omega^*_{zx} + a^*_{Sail-z_x})\xi + (\Omega^*_{zy} + a^*_{Sail-z_y})\eta + (\Omega^*_{zz} + a^*_{Sail-z_z})\zeta \tag{5.37}$$

where Ω^*_{ij} represents the second partial derivative of the pseudo-potential from Equations (2.53) - (2.55) evaluated at the specified collinear displaced Lagrangian point. The $a^*_{Sail-i_j}$ terms correspond to the partial derivatives of the scalar solar sail acceleration in the i^{th} unit direction vector of the rotating frame with respect to the j^{th} position coordinate in the rotating frame. The expressions for $a^*_{Sail-i_j}$ are summarized in Appendix A. Similarly, the augmented system matrix, $\mathbf{A}_{Aug}$ in the state-space representation, is now expanded as

$$\mathbf{A}_{Aug} = \begin{bmatrix} \mathbf{N_3} & \mathbf{I_3} \\ (\mathbf{\Omega^*_{i,j}} + \mathbf{a^*_{Sail-i_j}}) & \mathbf{D} \end{bmatrix} \tag{5.38}$$

and observe that $\mathbf{A}_{Aug}$ is a constant matrix. Thus, the state-space form for the analysis of behavior in the vicinity of the collinear Lagrangian points with a solar sail appears as

$$\begin{Bmatrix} \dot{\xi} \\ \dot{\eta} \\ \dot{\zeta} \\ \ddot{\xi} \\ \ddot{\eta} \\ \ddot{\zeta} \end{Bmatrix} = \begin{bmatrix} 0 & 0 & 0 & 1 & 0 & 0 \\ 0 & 0 & 0 & 0 & 1 & 0 \\ 0 & 0 & 0 & 0 & 0 & 1 \\ (\Omega^*_{xx} + a^*_{Sail-x_x}) & 0 & 0 & 0 & 2 & 0 \\ 0 & (\Omega^*_{yy} + a^*_{Sail-y_y}) & 0 & -2 & 0 & 0 \\ 0 & 0 & (\Omega^*_{zz} + a^*_{Sail-z_z}) & 0 & 0 & 0 \end{bmatrix} \begin{Bmatrix} \xi \\ \eta \\ \zeta \\ \dot{\xi} \\ \dot{\eta} \\ \dot{\zeta} \end{Bmatrix} \tag{5.39}$$

The new characteristic polynomial corresponding to the in-plane motion is formulated using the information from Equation (5.35) - (5.36), and the result is

$$\begin{aligned} &\lambda^4 + (4 - \Omega^*_{xx} - \Omega^*_{yy} - a^*_{Sail-x_x} - a^*_{Sail-y_y})\lambda^2 \\ &\quad + 2(\Omega^*_{xy} - \Omega^*_{yx} + a^*_{Sail-x_y} - a^*_{Sail-y_x})\lambda \\ &\quad + ((\Omega^*_{xx} + a^*_{Sail-x_x})(\Omega^*_{yy} + a^*_{Sail-y_y}) - (\Omega^*_{xy} + a^*_{Sail-x_y})(\Omega^*_{yx} + a^*_{Sail-y_x})) = 0 \end{aligned} \tag{5.40}$$

Confining the analysis to displaced collinear Lagrangian points, i.e. $y_{L_i} = z_{L_i} = 0$, and $\Omega^*_{xy} = \Omega^*_{yx} = 0$, further reduces Equation (5.40) to the form

$$\lambda^4 + (4 - \Omega^*_{xx} - \Omega^*_{yy} - a^*_{Sail-x_x} - a^*_{Sail-y_y})\lambda^2 + (\Omega^*_{xx} + a^*_{Sail-x_x})(\Omega^*_{yy} + a^*_{Sail-y_y}) = 0 \tag{5.41}$$

Confining the solution to the primary plane of motion results in $(\Omega^*_{xx} + a^*_{Sail-x_x})(\Omega^*_{yy} + a^*_{Sail-y_y}) < 0$. The form of Equation (5.41) is easily transformed from a quartic to a quadratic equation of the form

$$\Lambda^2 + 2\rho_1\Lambda - \rho_2^2 = 0 \tag{5.42}$$

where Λ again represents the roots of the Equation (5.42). The reformulations of the coefficients from Equation (5.41) result in the associated constants,

$$\rho_1 = 2 - \frac{\Omega^*_{xx} + \Omega^*_{yy} + a^*_{Sail-x_x} + a^*_{Sail-y_y}}{2} \tag{5.43}$$

$$\rho_2^2 = -(\Omega^*_{xx} + a^*_{Sail-x_x})(\Omega^*_{yy} + a^*_{Sail-y_y}) \tag{5.44}$$

Similar to Equations (2.76) - (2.77), ρ_1 and ρ_2 are both real. Thus, the quadratic roots are of the same form as Equations (2.78) and (2.79), that is,

$$\Lambda_1 = -\rho_1 + \sqrt{\rho_1^2 + \rho_2^2} \tag{5.45}$$

$$\Lambda_2 = -\rho_1 - \sqrt{\rho_1^2 + \rho_2^2} \tag{5.46}$$

Analysis of the quintic roots reveals that the eigenvalues of the linear solar sail model possess the same characteristics as the linear system represented by Equation (2.74) That is, $\lambda_{1,2}$ are real ($\Re$) eigenvalues and $\lambda_{3,4}$ are purely imaginary ($\Im$) eigenvalues. Thus, continuing the linear analysis similar to that completed for the linear model in the traditional CR3BP, the appropriate selection of the initial conditions prevents the excitation of the divergent behavior. Recall that the general solution for the in-plane motion near the vicinity of the collinear Lagrangian points in the CR3BP is reflected in Equations (2.92) and (2.93). The corresponding expression in terms of the new definitions is rewritten as

$$\xi = \xi_0 Cos[\varpi(\tau - \tau_0)] + \frac{\eta_0}{\rho_3} Sin[\varpi(\tau - \tau_0)] \tag{5.47}$$

$$\eta = \eta_0 Cos[\varpi(\tau - \tau_0)] + \xi_0 \rho_3 Sin[\varpi(\tau - \tau_0)] \tag{5.48}$$

where ϖ and ρ_3 are real quantities, i.e.,

$$\lambda_3 = i\varpi \tag{5.49}$$

$$\nu_3 = i\rho_3 \tag{5.50}$$

The representative expressions for ϖ and β_3 are

$$\varpi = \sqrt{\rho_1 + \sqrt{\rho_1^2 + \rho_2^2}} \tag{5.51}$$

$$\beta_3 = \frac{\varpi^2 + \Omega_{xx}^* + a_{Sail-x_x}^*}{2\varpi} \tag{5.52}$$

Thus, the initial conditions for the in-plane components of velocity are derived from the derivatives of Equations (5.47) and (5.48) at an initial time, $\tau = \tau_0$,

$$\dot{\xi}_0 = \frac{\eta_0 \varpi}{\rho_3} \tag{5.53}$$

$$\dot{\eta}_0 = -\xi_0 \rho_3 \varpi \tag{5.54}$$

Note that the initial conditions are functions of the sail lightness parameter, β, since the acceleration components for the solar sail model are directly related to the sail lightness parameter. The impact of β on the initial conditions for the linear response is represented in Table 5.1. To visualize the shift in both the locations of the displaced Lagrangian points and the relative orbit about that point, the linear paths associated with three sets of initial conditions are plotted corresponding to three different values of the sail lightness parameter, β, in Figure 5.3. The table locates the position of the

Table 5.1 Initial Condition for Linear Orbits as a Function of Sail Parameter, β.

β_i	x_{L_1} (km)	ξ_0 (km)	η_0 (km)	$\dot{\xi}_0$ (km/s)	$\dot{\eta}_0$ (km/s)	Period (days)
$\beta_1 = 0.00$	148105889	200,000	0	0	0.26831	≈175
$\beta_2 = 0.03$	147397139	200,000	0	0	0.141507	≈247
$\beta_3 = 0.05$	146671041	200,000	0	0	0.107480	≈291

collinear Lagrangian point relative to P_2, the Earth, and the initial velocities, $\dot{\xi}_0$ and $\dot{\eta}_0$, for s specific sail parameter, β. In this example, the sail is completely "face-on" to the flow of photons, i.e., $\alpha = 0^o$ and γ is arbitrary. Using the information listed in Table 5.1, the linear response for the three sets of initial conditions appears in Figure 5.3. The set of three orbits includes the orbit corresponding to $\beta_1 = 0.00$, i.e., equivalent to a spacecraft with either no sail or a sail completely turned edge-on as plotted in purple. The initial conditions for each orbit in the figure is denoted as a black dot along with the clockwise direction. Clearly, the position of the artificial Lagrangian point, L_1, shifts towards P_1, i.e., the Sun. The size of the linear orbit also decreases with sail lightness parameter. Of course, these initial conditions result in a periodic orbit only in the linear system. In addition, the orbits are consistent with the assumption that the sail maintains its orientation throughout the periodic orbit, i.e., $\alpha = 0^o$ and γ is arbitrary. Propagation of these initial conditions in a nonlinear model for the SS-CR3BP results in the departure of the spacecraft from the vicinity of the linear approximation, thus, departing from an orbit about the displaced Lagrangian

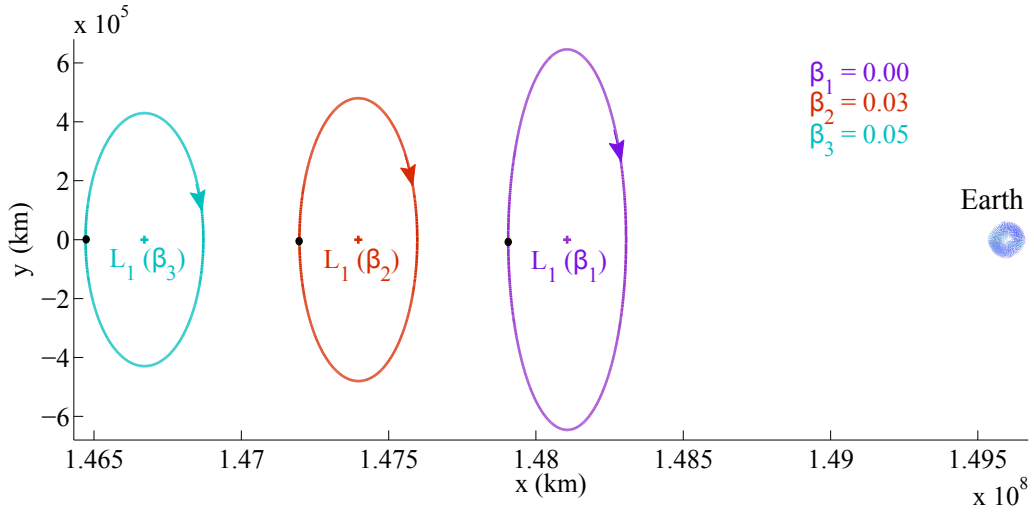

Figure 5.3. Displaced S-E Collinear Lagrangian Points Progression with Linearized Periodic Orbits.

point. Although the trajectory departs, the linear solution is a good initial guess for a corrections process to produce an exact solution in the nonlinear problem.

6. DIFFERENTIAL CORRECTIONS FOR TRAJECTORY DESIGN EMPLOYING SAIL ANGLES

Preliminary design of trajectories in the SS-CR3BP is typically based on a differential corrections scheme. A numerical corrections approach from the CR3BP is extended to incorporate the solar sail angles. The existence of displaced Lagrangian points expands the regions of interest in the vicinity of these libration points. These regions are explored for the existence of periodic orbits and trajectories of interest that incorporate the solar sail model.

6.1 Augmented State Transition Matrix

The inclusion of the effects of photons on the acceleration of a solar sail based spacecraft increases the complexity associated with the system model. Thus, the evolution of a state over time is first analyzed in response to changes in the initial states that include the sail angles, that is, α and γ. Assume the following form for an eight-dimensional initial state, $\vec{X}(\tau_0)$,

$$\vec{X}(\tau_0) = \begin{Bmatrix} x_0 & y_0 & z_0 & \dot{x}_0 & \dot{y}_0 & \dot{z}_0 & \alpha_0 & \gamma_0 \end{Bmatrix}^T \tag{6.1}$$

Propagating the trajectory with the initial conditions in $\vec{X}(\tau_0)$ yields a baseline reference path for the augmented state transition matrix, Φ_{Aug}. Introducing a small perturbation, $\delta\vec{X}(\tau_0)$, produces the nearby initial conditions, $\vec{X}^*(\tau_0)$,

$$\delta\vec{X}(\tau_0) = \begin{Bmatrix} \delta x_0 & \delta y_0 & \delta z_0 & \delta\dot{x}_0 & \delta\dot{y}_0 & \delta\dot{z}_0 & \delta\alpha_0 & \delta\gamma_0 \end{Bmatrix}^T \tag{6.2}$$

$$\vec{X}^*(\tau_0) = \vec{X}(\tau_0) + \delta\vec{X}(\tau_0) \tag{6.3}$$

The updated initial state, $\vec{X}^*(\tau_0)$, is propagated and results in a new time-varying nearby arc. Note that the orientation of the sail, i.e., the sail angles, α_0 and γ_0, remain

fixed throughout this propagation relative to the Sun in the rotating frame. Thus, for assessing the dependencies, the sail angles are independent of the position and the velocity states over time, τ. The new state along the trajectory, in the vicinity of the baseline or the previous iteration, is approximated based on the linear mapping, that is, the augmented state transition matrix, STM_{Aug}. Thus, applying a first-order Taylor series expansion about the reference and neglecting the higher-order terms, the linear variational relationship is written in the form,

$$\dot{\delta\vec{X}} = \mathbf{A}_{Aug}(\tau)\delta\vec{X} \tag{6.4}$$

Note, in contrast to Equation (5.38), the $\mathbf{A}_{Aug}$ matrix is time-dependent. If the three second-order equations governing the motion of the sailcraft are expressed as six first-order scalar equations incorporating the effects of the sail angles, the partials relative to the initial position, velocity states and orientation angles, corresponding to the elements of the system matrix, are formulated such that

$$\left.\frac{\partial\vec{F}}{\partial\vec{X}}\right|_{\vec{X}_0} = \mathbf{A}_{Aug}(\tau) = \begin{bmatrix} \mathbf{N_{3,3}} & \mathbf{I_3} & \mathbf{N_{3,2}} \\ (\mathbf{\Omega_{i,j}}(\tau) + \mathbf{a_{Sail-i_j}}) & \mathbf{D} & \mathbf{C} \\ \mathbf{N_{2,3}} & \mathbf{N_{2,3}} & \mathbf{N_{2,2}} \end{bmatrix} \tag{6.5}$$

where $\mathbf{N_{p,q}}$ are the null matrices of size $p \times q$. Submatrices $\mathbf{I_3}$, $(\mathbf{\Omega_{i,j}}(\tau) + \mathbf{a_{Sail-i_j}})$, and $\mathbf{D}$ of matrix $\mathbf{A}$ are consistent with the terms defined in Equation (5.38). The inclusion of the solar sail introduces partials relative to the effect of solar sail angles, α and γ, on the scalar acceleration terms associated with the equations of motion. Information related to these partials is expressed within submatrix, $\mathbf{C}$.

$$\mathbf{C} = \begin{bmatrix} a_{Sail-x_\alpha} & a_{Sail-x_\gamma} \\ a_{Sail-y_\alpha} & a_{Sail-y_\gamma} \\ a_{Sail-z_\alpha} & a_{Sail-z_\gamma} \end{bmatrix} \tag{6.6}$$

The complete expressions for the partials of the scalar solar sail accelerations relative to the sail angles, α and γ , in the rotating frame are listed in Appendix B. Thus, the updated formulation for the general solution in linear vector form, is expressed as

$$\delta\vec{X}(\tau_f) = \Phi_{Aug}(\tau_f, \tau_0)\delta\vec{X}(\tau_0) \tag{6.7}$$

where $\Phi_{Aug}(\tau_f, \tau_0)$ is an 8×8 STM$_{Aug}$ that maps the change in initial state, $\delta\vec{X}(\tau_0)$, a 1×8 state vector, to the change in final state, $\delta\vec{X}(\tau_f)$, also a 1×8 final state vector. To determine the elements of the STM$_{Aug}$, the variational equations and the equations of motion corresponding to the solar sail model are numerically integrated simultaneously. The mathematical expression for the matrix variational equation is given as

$$\dot{\Phi}(\tau_f, \tau_0) = \mathbf{A}_{Aug}(\tau_f)\Phi_{Aug}(\tau_f, \tau_0) \tag{6.8}$$

Based on the eight initial scalar states, the elements of the 8×8 STM$_{Aug}$, that relate the final states to the initial eight states, are evaluated as partials, such that,

$$\Phi_{Aug}(\tau_f, \tau_0) = \begin{bmatrix} \frac{\partial x}{\partial x_0} & \frac{\partial x}{\partial y_0} & \frac{\partial x}{\partial z_0} & \frac{\partial x}{\partial \dot{x}_0} & \frac{\partial x}{\partial \dot{y}_0} & \frac{\partial x}{\partial \dot{z}_0} & \frac{\partial x}{\partial \alpha_0} & \frac{\partial x}{\partial \gamma_0} \\ \frac{\partial y}{\partial x_0} & \frac{\partial y}{\partial y_0} & \frac{\partial y}{\partial z_0} & \frac{\partial y}{\partial \dot{x}_0} & \frac{\partial y}{\partial \dot{y}_0} & \frac{\partial y}{\partial \dot{z}_0} & \frac{\partial y}{\partial \alpha_0} & \frac{\partial y}{\partial \gamma_0} \\ \frac{\partial z}{\partial x_0} & \frac{\partial z}{\partial y_0} & \frac{\partial z}{\partial z_0} & \frac{\partial z}{\partial \dot{x}_0} & \frac{\partial z}{\partial \dot{y}_0} & \frac{\partial z}{\partial \dot{z}_0} & \frac{\partial z}{\partial \alpha_0} & \frac{\partial z}{\partial \gamma_0} \\ \frac{\partial \dot{x}}{\partial x_0} & \frac{\partial \dot{x}}{\partial y_0} & \frac{\partial \dot{x}}{\partial z_0} & \frac{\partial \dot{x}}{\partial \dot{x}_0} & \frac{\partial \dot{x}}{\partial \dot{y}_0} & \frac{\partial \dot{x}}{\partial \dot{z}_0} & \frac{\partial \dot{x}}{\partial \alpha_0} & \frac{\partial \dot{x}}{\partial \gamma_0} \\ \frac{\partial \dot{y}}{\partial x_0} & \frac{\partial \dot{y}}{\partial y_0} & \frac{\partial \dot{y}}{\partial z_0} & \frac{\partial \dot{y}}{\partial \dot{x}_0} & \frac{\partial \dot{y}}{\partial \dot{y}_0} & \frac{\partial \dot{y}}{\partial \dot{z}_0} & \frac{\partial \dot{y}}{\partial \alpha_0} & \frac{\partial \dot{y}}{\partial \gamma_0} \\ \frac{\partial \dot{z}}{\partial x_0} & \frac{\partial \dot{z}}{\partial y_0} & \frac{\partial \dot{z}}{\partial z_0} & \frac{\partial \dot{z}}{\partial \dot{x}_0} & \frac{\partial \dot{z}}{\partial \dot{y}_0} & \frac{\partial \dot{z}}{\partial \dot{z}_0} & \frac{\partial \dot{z}}{\partial \alpha_0} & \frac{\partial \dot{z}}{\partial \gamma_0} \\ 0 & 0 & 0 & 0 & 0 & 0 & 1 & 0 \\ 0 & 0 & 0 & 0 & 0 & 0 & 0 & 1 \end{bmatrix} \tag{6.9}$$

The zeros in the last two rows of the 8×8 STM$_{Aug}$ matrix reflect the fact that the sail orientation angles are independent of the position and velocity states and remain constant over the integration arc. The remaining 48 time-varying elements of the STM$_{Aug}$ are evaluated by numerically integrating the matrix variational equations in Equation (6.8) along with the equations of motions, given the initial conditions, and,

$$\Phi(\tau_0, \tau_0) = I_{8\times 8} \tag{6.10}$$

where $\mathbf{I}_{8\times 8}$ is a 8×8 identity matrix. The augmented state transition matrix, STM$_{Aug}$ is now used in a corrections scheme to produce periodic orbits in the vicinity of displaced collinear Lagrangian points.

6.2 Differential Corrections Scheme based on Sail Orientation Angles

For trajectory design, a two-point boundary value problem can be solved using a differential corrections scheme and implementing solar sail angles as design parameters. The corrections scheme is formulated to iteratively modify the initial states based on the linear estimated information available from the STM_{Aug}; iterations continue until the desired final state is achieved to a specified tolerance level. The scheme is implemented with constraints and additional free-variables, i.e., the sail orientation angles. In the algorithm for the shooting scheme, the free-variables are the available controls. In the case of a solar sail, in addition to initial position and velocity states, the free variables include the orientation angles α and γ. Thus, for implementation of the corrections scheme, a vector $\vec{X}$ is formulated that includes the sail states, α and γ, acting as control parameters to achieve the vector constraints, $\vec{F}(\vec{X}) = \vec{0}$, associated with the trajectory. The corrections scheme is developed based on the same strategy as that applied in the classical CR3BP with a modified set of design variables.

6.2.1 Fixed-Time Single Shooting: Sail Angles as Design Variables

The inclusion of sail angles offers additional options for formulation of the shooting scheme. To analyze the targeting algorithm based on sail angles, assume that a spacecraft is located at a certain position and with some velocity. By adding to the available controls within the initial state vector, an 8×1 vector $\vec{X}(\tau_0)$, is defined,

$$\vec{X}(\tau_0) = \begin{Bmatrix} x_0 \\ y_0 \\ z_0 \\ \dot{x}_0 \\ \dot{y}_0 \\ \dot{z}_0 \\ \alpha_0 \\ \gamma_0 \end{Bmatrix} \tag{6.11}$$

Note that τ_0 represents the initial nondimensional time. The corrections scheme is formulated to target a desired six-dimensional final vector of scalar position and velocity states, $\vec{X}^*(\tau_f)$,

$$\vec{X}^*(\tau_f) = \begin{Bmatrix} \vec{r}^* \\ \\ \vec{v}^* \end{Bmatrix} \tag{6.12}$$

where $\vec{r}^*$ and $\vec{v}^*$ are the three-dimensional position and velocity state vectors, respectively. Thus, the TOF between the initial and the final state is defined as $\tau_f - \tau_0$. For this particular sample formulation, the TOF remains constant over the integration time between successive iterations. If the initial sail angles are formulated as the only available design variables, the $\vec{X}(\tau_0)$ vector is reduced to

$$\vec{X}(\tau_0) = \begin{bmatrix} \alpha_0 \\ \\ \gamma_0 \end{bmatrix} \tag{6.13}$$

Equation (6.13) implies that the initial position and velocity states are not updated – only the sail angles are allowed to vary. Given the number of design variables, to achieve a unique solution, only two final states can be targeted from the total six-dimensional desired state vector, $\vec{X}^*(\tau_f)$. This reduces the application of a fixed-time single shooting algorithm that only allows sail orientation angles, α and γ as the available design options.

6.2.2 Variable-Time Single Shooting: Sail Angles as Design Variables

Extending the analysis from a fixed-time single shooting scheme using solar sail angles, α and γ, to a variable-time approach can increase the total number of design variables to three. The new design variable vector, $\vec{X}(\tau_0)$, is

$$\vec{X}(\tau_0) = \begin{bmatrix} \alpha_0 \\ \\ \gamma_0 \\ \\ \tau \end{bmatrix} \tag{6.14}$$

where τ is the TOF, i.e., integration time between the initial and the final specified state. Thus, the corrections scheme is developed to target a maximum of three constraints. Though the number of possible solutions have increased in comparison to a fixed-time single shooting process using only sail orientation angles for control, the variable-time single shooting strategy with sail orientation angles plus time as the control variables also faces the limitations. The versatility of both fixed-time and variable-time single shooting schemes is increased by extending the basic strategy in a multiple shooting scheme. Multiple arcs introduce more control variables that are beneficial in meeting the final targeting constraints.

6.3 Multiple Shooting using Sail Orientation Angles

To generate a solution in a complex scenario, the differential corrections scheme is extended to a set of n discrete patch points. Any multiple-shooting scheme is based on a strategy that is similar to any single-shooting iteration process. In contrast, however, the trajectory is now decomposed into a set of arcs, identified in terms of n discrete points, thus, allowing more flexibility in the corrections process. Recall that these points are denoted 'patch-points'. The overall objective of a multiple shooting differential corrections algorithm is a complete trajectory that is continuous in position and velocity. To achieve such continuity, orientation angles associated with the solar sail are iteratively updated to result in a final converged path. A specific design scenario may or may not allow the TOF to vary along each segment between the patch points. Thus, two multiple shooting formulations based on solar sail angles is again formulated, i.e., fixed-time and variable-time multiple shooting algorithm using sail angles, α and γ, as design parameters.

6.3.1 Fixed-Time Multiple Shooting using Sail Orientation Angles

Under the assumption that the integration time, τ_i, remains fixed along each arc between the patch points, a fixed-time multiple shooting scheme is easily formulated.

The introduction of sail orientation angles, α and γ, within the design variable vector is now expressed in general form as

$$\vec{X} = \begin{Bmatrix} \vec{X}_1(\tau_{0_1}) \\ \vec{X}_2(\tau_{0_2}) \\ \vdots \\ \vec{X}_{n-1}(\tau_{0n-1}) \\ \vec{X}_n(\tau_{0_n}) \end{Bmatrix} \tag{6.15}$$

Note that, $\vec{X}_i$ is now an eight-dimensional vector (as defined in Equation (6.11).) comprised of three position states, three velocity states and two orientation angles. Recall that n indicates the number of patch points used to discretize the trajectory into $n-1$ segments. Thus, $\vec{X}$ is a $8n \times 1$ dimensional design variable vector for a fixed-time multiple shooting algorithm that incorporates sail angles along each segment. The constraint vector, $\vec{F}(\vec{X})$, is constructed to maintain continuity in both position and velocity states between the end states along any arc and the subsequent patch point, i.e.,

$$\vec{F}(\vec{X}) = \begin{Bmatrix} \vec{X}_1(\tau_{f_1})[1:6] - \vec{X}_2(\tau_{0_2})[1:6] \\ \vec{X}_2(\tau_{f_2})[1:6] - \vec{X}_3(\tau_{0_3})[1:6] \\ \vdots \\ \vec{X}_{n-2}(\tau_{f_{n-2}})[1:6] - \vec{X}_{n-1}(\tau_{0_{n-1}})[1:6] \\ \vec{X}_{n-1}(\tau_{f_{n-1}})[1:6] - \vec{X}_n(\tau_{0_n})[1:6] \end{Bmatrix} \tag{6.16}$$

Continuity is maintained only for the six position and velocity states between each arc as denoted by $[1:6]$. The sail angles are free to differ between two arcs to achieve position and velocity continuity between two segments. Thus, the length of the constraint vector is $6(n-1)$, that is, the number of arcs is one less than the number of patch points.

As a result of incorporating sail angles in the multiple shooting algorithm, the associated Jacobian matrix is modified. The partials relating the constraint vectors to variations in the design variables is contained in the Jacobian Matrix, $D\vec{F}(\vec{X})$,

$$D\vec{F}(\vec{X}) = \begin{bmatrix} (\frac{\partial \vec{X}_1(\tau_{f_1})}{\partial \vec{X}_1(\tau_{0_1})} - \frac{\partial \vec{X}_2(\tau_{0_2})}{\partial \vec{X}_1(\tau_{0_1})}) & (\frac{\partial \vec{X}_1(\tau_{f_1})}{\partial \vec{X}_2(\tau_{0_2})} - \frac{\partial \vec{X}_2(\tau_{0_2})}{\partial \vec{X}_2(\tau_{0_2})}) & & \\ \ddots & \ddots & & \\ & (\frac{\partial \vec{X}_{n-1}(\tau_{f_{n-1}})}{\partial \vec{X}_{n-1}(\tau_{0_{n-1}})} - \frac{\partial \vec{X}_n(\tau_{0_n})}{\partial \vec{X}_{n-1}(\tau_{0_{n-1}})}) & (\frac{\partial \vec{X}_{n-1}(\tau_{f_{n-1}})}{\partial \vec{X}_n(\tau_{0_n})} - \frac{\partial \vec{X}_n(\tau_{0_n})}{\partial \vec{X}_n(\tau_{0_n})}) \end{bmatrix} \tag{6.17}$$

where τ_{0_i} and τ_{f_i} denote the initial and the final time, respectively, on the i^{th} segment. The partials reflect the variations in the state at the final time along an arc relative to the eight-dimensional initial state vector, i.e., the position, the velocity and the orientation angles. The position and velocity states at the end of the reference arc i, $\vec{X}_i(\tau_{f_i})[1:6]$, are a function of the initial state along the segment, $\vec{X}_i(\tau_{0_i})$, one that includes the eight initial states, i.e., position, velocity and the orientation angles, α_{0_i} and γ_{0_i}. In this formulation, many terms within the $D\vec{F}(\vec{X})$ matrix are easily recognized as the terms in the augmented STM the $\phi_{Aug}[1:6,:]$. The subsequent patch point is not influenced by the selection of the previous initial patch point and, thus, $\frac{\partial \vec{X}_2(\tau_{0_2})}{\partial \vec{X}_1(\tau_{0_1})}$ is equal to $\vec{0}$. Likewise, the end state along the i^{th} reference arc, $\vec{X}_i(\tau_{f_i})$, is not a function of the subsequent patch point, $\vec{X}_{i+1}(\tau_{0_i})$, thus, $\frac{\partial \vec{X}_1(\tau_{f_1})}{\partial \vec{X}_2(\tau_{0_2})}$ is equal to $\vec{0}$. Lastly, the $\frac{\partial \vec{X}_i(\tau_{0_i})}{\partial \vec{X}_i(\tau_{0_i})}$ is equal to a rectangular diagonal matrix that is a 6×8 matrix with diagonal entries equal to one. In other words, the matrix can be also be written as

$$H_{6\times 8} = \frac{\partial \vec{X}_i(\tau_{0_i})}{\partial \vec{X}_i(\tau_{0_i})} = \begin{bmatrix} \mathbf{I_{6\times 6}} & \mathbf{N_{6\times 2}} \end{bmatrix} \tag{6.18}$$

where $\mathbf{I_{6\times 6}}$ is a 6×6 identity matrix and $\mathbf{N_{6\times 2}}$ is a null matrix of dimensions 6×2. Substituting this information, the $D\vec{F}(\vec{X})$ matrix is rewritten in the form

$$D\vec{F}(\vec{X}) = \begin{bmatrix} \phi_{Aug}(\tau_{f_1}, \tau_{0_1})[1:6,:] & -H_{6\times 8} & & \\ \ddots & \ddots & & \\ & & \phi_{Aug}(\tau_{f_n}, \tau_{0_n})[1:6,:] & -H_{6\times 8} \end{bmatrix} \tag{6.19}$$

This matrix is then employed in the update equation to iteratively converge the constraint vector, $\vec{F}(\vec{X}^*)$ to zero, i.e., $\vec{F}(\vec{X}^*) = \vec{0}$ within an acceptable level of tolerance.

6.3.2 Variable-Time Multiple Shooting Incorporating Sail Angles

Allowing the integration time, τ_i, to vary along any segment, further extends the capabilities of using sail angles in the multiple shooting scheme, thus, resulting in the formulation of variable-time multiple shooting algorithm. The updated design variable vector now includes additional variables, τ_i. Thus, the design variable vector is an $8n \times 1$ vector since there are $n-1$ integration times corresponding to $n-1$ arcs between n patch points, i.e.,

$$\vec{X} = \begin{Bmatrix} \vec{X}_1(8\times 1) \\ \vdots \\ \vec{X}_n(8\times 1) \\ \tau_1 \\ \vdots \\ \tau_{n-1} \end{Bmatrix} \tag{6.20}$$

The constraint vector, $\vec{F}(\vec{X})$ is the same as that defined for a fixed-time multiple shooting approach to maintain continuity in both position and velocity states,

$$\vec{F}(\vec{X}) = \begin{Bmatrix} \vec{X}_1(\tau_{f_1})[1:6] - \vec{X}_2(\tau_{0_2})[1:6] \\ \vec{X}_2(\tau_{f_2})[1:6] - \vec{X}_3(\tau_{0_3})[1:6] \\ \vdots \\ \vec{X}_{n-2}(\tau_{f_{n-2}})[1:6] - \vec{X}_{n-1}(\tau_{0_{n-1}})[1:6] \\ \vec{X}_{n-1}(\tau_{f_{n-1}})[1:6] - \vec{X}_n(\tau_{0_n})[1:6] \end{Bmatrix} \tag{6.21}$$

Recall that the $\vec{F}(\vec{X})$ matrix is of dimension $6(n-1)$. Since the reference state at the end of each arc, $\vec{X}_i(\tau_{f_i}[1:6]$ is a function of the integration time, τ_i, the updated $D\vec{F}(\vec{X})$ is rewritten as

$$D\vec{F}(\vec{X}) = \begin{bmatrix} (\frac{\partial \vec{X}_1(\tau_{f_1})}{\partial \vec{X}_1(\tau_{0_1})} - \frac{\partial \vec{X}_2(\tau_{0_2})}{\partial \vec{X}_1(\tau_{0_1})}) & (\frac{\partial \vec{X}_1(\tau_{f_1})}{\partial \vec{X}_2(\tau_{0_2})} - \frac{\partial \vec{X}_2(\tau_{0_2})}{\partial \vec{X}_2(\tau_{0_2})}) & \frac{\partial \vec{X}_1}{\partial \tau_1} \\ \ddots & \ddots & \ddots \\ (\frac{\partial \vec{X}_{n-1}(\tau_{f_{n-1}})}{\partial \vec{X}_{n-1}(\tau_{0_{n-1}})} - \frac{\partial \vec{X}_n(\tau_{0_n})}{\partial \vec{X}_{n-1}(\tau_{0_{n-1}})}) & (\frac{\partial \vec{X}_{n-1}(\tau_{f_{n-1}})}{\partial \vec{X}_n(\tau_{0_n})} - \frac{\partial \vec{X}_n(\tau_{0_n})}{\partial \vec{X}_n(\tau_{0_n})}) & \frac{\partial \vec{X}_{n-1}}{\partial \tau_{n-1}} \end{bmatrix} \tag{6.22}$$

Inclusion of integration times introduced a new set of terms along a diagonal, $\frac{\partial \vec{X}_i}{\partial \tau_i}$, that corresponds to the partial of each state at the end point along i^{th} reference segment with respect to the integration time for the i^{th} arc. Thus, rewriting Equation (6.22) in a form similar to Equation (6.19) to incorporate inclusion of time as design variable results in an expression

$$D\vec{F}(\vec{X}) = \begin{bmatrix} \phi_{Aug}(\tau_{f_i}, \tau_{0_i})[1:6,:] & -H_{6\times 8} & \dot{\vec{X}}_1[1:6] \\ \ddots & \ddots & \ddots \\ & \phi_{Aug}(\tau_{f_n}, \tau_{0_n})[1:6,:] \quad -H_{6\times 8} & \dot{\vec{X}}_{n-1}[1:6] \end{bmatrix} \tag{6.23}$$

where $\dot{\vec{X}}_i[1:6]$ represents the time derivatives corresponding to the position and velocity states at the end point along any reference segment, $\vec{X}_i[1:6]$. Recall that the orientation angles remain fixed relative to the rotating frame over the integration time between two patch points. Finally, the update requires a minimum norm solution since the Jacobian, $D\vec{F}(\vec{X})$, is an $8(n-1)\times 9n$ rectangular matrix. Thus, the iteration process with a good goal to satisfy the constraint vector relationship, $\vec{F}(\vec{X}^*) = \vec{0}$, proceeds. New position and velocity states are delivered along with the orientation angles, α_{0_i} and γ_{0_i}, as well as a new TOF, τ_i^*, between each subsequent patch point.

7. PERIODIC ORBITS AND TRAJECTORY DESIGN IN THE SS-CR3BP

The corrections algorithm incorporating the solar sail orientation angles is extended to construct periodic orbits in the vicinity of the artificial Lagrangian points. Previous missions have been designed to maintain a vehicle in the vicinity of the classical Lagrangian points. Incorporating the sail angles in search of new families of three-dimensional halo orbits or other periodic orbits increases the design space for trajectory design and, thus, potentially leads to new design scenarios for mission applications.

7.1 Construction of Sail-Based Periodic Orbits

For the analysis and construction of periodic orbits in the nonlinear SS-CR3BP model, it is insightful to first examine the response of initial states obtained from the linear model when the linear initial state is propagated in the nonlinear SS-CR3BP model. When the solar sail force is active, the trajectories generated by the initial state from Subsection 5.4.2 is plotted in Figure 7.1. Obviously, the trajectories for different sail parameters, β, are no longer periodic and the spacecraft quickly departs from the path predicted by the linear model. Also note that the trajectories are all in-plane. Thus, a corrections process is employed to determine new periodic solutions in the vicinity of the displaced collinear Lagrangian points using sail orientation angles. The in-plane initial state from the linear model is used as an initial guess for the corrections scheme. The initial guess for α and γ is of order 10^{-5} degrees. To search for periodic orbits, symmetry and perpendicular crossings are employed as constraints. A generic formulation for construction of both planar orbits and three-dimensional halo orbits facilitates this process.

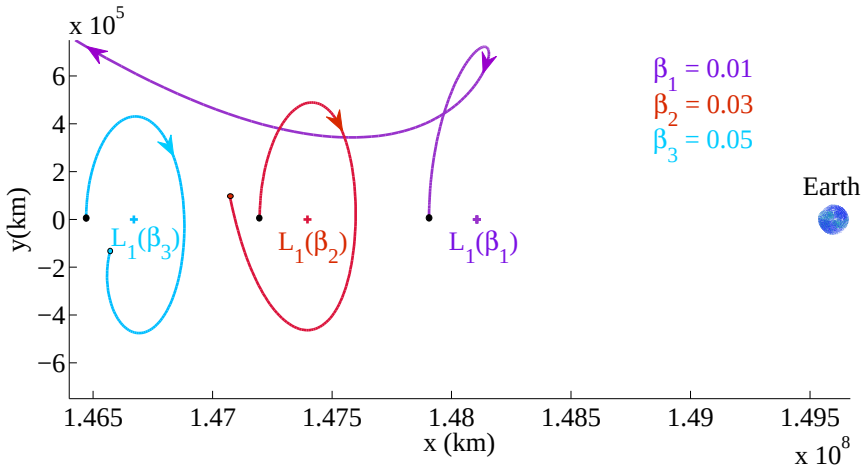

Figure 7.1. Linear Initial Guess Propagated in Nonlinear Model.

The algorithm, demonstrated in Subsection 3.4.1, for generating periodic orbits in the vicinity of the collinear Lagrangian points is further extended to incorporate a solar sail model. Let the initial state lie in the $\hat{x} - \hat{y}$ plane (z = 0) with an initial sail orientation of order 10^{-5} degrees, as given by sail angles, α_0 and γ_0, and the initial velocity be perpendicular to the $\hat{x} - \hat{z}$ plane, i.e., $\dot{z} = 0$. The in-plane initial position and velocity states are represented in Table 5.1. The formulation for an algorithm to obtain a periodic orbit is governed by allowing the sail angles, α_0, γ_0, and the trajectory propagation time, τ, to implicitly vary by integrating to the map, $\Sigma : y = 0$. Thus, a design vector is formulated, that is,

$$\vec{X}(\tau_0) = \begin{bmatrix} \alpha_0 \\ \gamma_0 \\ \tau \end{bmatrix} \tag{7.1}$$

The sail angles are iteratively varied until a perpendicular crossing is achieved while implicitly allowing the propagation time to vary, i.e., half a period for the particular orbit. Note that for the duration of iteration, both the initial and the final states lie on the $\hat{x} - \hat{z}$ plane. For the final state to be perpendicular to the plane, the final

velocities, $\dot{x}$ and $\dot{z}$ are constrained, such that, $\dot{x} = \dot{z} = 0$. Thus, the constraint vector is selected.

$$\vec{F}(\vec{X}) = \begin{bmatrix} y \\ \dot{x} \\ \dot{z} \end{bmatrix} = \vec{0} \tag{7.2}$$

The augmented $D\vec{F}(\vec{X})$ matrix of partials is formulated based on constraint vector, $\vec{F}(\vec{X})$, as well as the design vector, $\vec{X}$, that is,

$$D\vec{F}(\vec{X}) = \frac{\partial \vec{F}(\vec{X})}{\partial \vec{X}} = \begin{bmatrix} \frac{\partial y}{\partial \alpha_0} & \frac{\partial y}{\partial \gamma_0} & \frac{\partial y}{\partial \tau} \\ \frac{\partial \dot{x}}{\partial \alpha_0} & \frac{\partial \dot{x}}{\partial \gamma_0} & \frac{\partial \dot{x}}{\partial \tau_0} \\ \frac{\partial \dot{z}}{\partial \alpha_0} & \frac{\partial \dot{z}}{\partial \gamma_0} & \frac{\partial \dot{z}}{\partial \tau} \end{bmatrix} \tag{7.3}$$

The augmented $D\vec{F}(\vec{X})$ in Equation (7.3) is now expressed in terms of the elements of the STM and is augmented with the appropriate velocity and acceleration at the terminal time along the reference path.

$$D\vec{F}(\vec{X}) = \begin{bmatrix} \phi_{27} & \phi_{28} & \phi_{29} \\ \phi_{47} & \phi_{48} & \phi_{49} \\ \phi_{67} & \phi_{68} & \phi_{69} \end{bmatrix} \tag{7.4}$$

The equality between the number of available design variables and the number of constraints in this example results in a square $D\vec{F}(\vec{X})$ matrix. Subsequently, the predicted change in design variables, $\delta\alpha_0$, $\delta\gamma_0$ and $\delta\tau$ is evaluated as

$$\delta\vec{X}^j = \begin{bmatrix} \delta\alpha_0^j \\ \delta\gamma_0^j \\ \delta\tau^j \end{bmatrix} = -D\vec{F}(\vec{X}^j)^{-1}\vec{F}(\vec{X}^j) \tag{7.5}$$

Note that, since the integration proceeds to map, $\Sigma : y = 0$, a variable time implicit formulation leads to explicitly updating only the sails orientation angles, α_0 and γ_0, and not the integration time, τ,

$$\vec{X}^{j+1} = \begin{bmatrix} \alpha_0^{j+1} \\ \\ \gamma_0^{j+1} \end{bmatrix} = \vec{X}^j + \delta\vec{X}^j = \begin{bmatrix} \alpha_0^j \\ \\ \gamma_0^j \end{bmatrix} + \begin{bmatrix} \delta\alpha_0^j \\ \\ \delta\gamma_0^j \end{bmatrix} \tag{7.6}$$

The integration time is changed appropriately. An iterative process is applied to meet the final constraints, $\dot{x} = \dot{z} = 0$, that is, a perpendicular crossing of the map, $\Sigma : y = 0$, by updating the design variables, α_0 and γ_0. The initial position and velocity states are fixed and only the sail orientation are allowed to vary in this formulation.

Once the perpendicular crossing is delivered with an implicit variable-time scheme, the sail orientation angles at $\Sigma : y = 0$ are again iteratively corrected to ultimately achieve a periodic, continuous trajectory. The correction scheme is applied to the trajectories that appear in Figure 7.1. Thus, a set of orientation angles is iteratively calculated for each perpendicular crossing, i.e., at half the period (τ) and at one full period (2τ) The orientation angles, α_0 and γ_0, for the periodic orbits plotted in Figure 7.2 are represented in Table 7.1. Recall that the maximum attitude orientation rate

Table 7.1 Sail Orientation Angles for Periodic Solution shown in Figure 7.2

β_i	$\alpha_0(0 \to 2\tau)$	$\gamma_0(0 \to \tau)$	$\gamma_0(\tau \to 2\tau)$	TOF (days)
$\beta_1 = 0.01$	11.09^o	90^o	-90^o	≈181
$\beta_2 = 0.03$	0.02^o	-90^o	90^o	≈249
$\beta_3 = 0.05$	0.016^o	90^o	-90^o	≈290

is 0.02^o/s. Several observations of Table 7.1 are notable: (1) The values in the table in successive time block sometimes appear to shift by large amount. The value of γ, for example, does not pass through an actual reorientation of 180^o. Recall Figure 5.1, where γ is the angle between the reference direction vector, $\hat{k}$, and the projection of

the sail normal unit vector onto a plane. By changing α from a negative to a positive value, the sail angle, γ switches from 90^o to -90^o without any actual rotation of 180^o. (2) To reorient the sail, the change in projection is equivalent to a change from 11.09^o to -11.09^o. The total change of 22.18^o requires approximately 18.5 minutes. On the time scale of an orbital period that is 181 days, 18.5 minutes, the interval to shift the orientation of the sail is less than 0.007% of the period. Thus, for preliminary analysis, the assumption of an instantaneous change in the sail angle is reasonable. (3) It is also vital to point out that, even though the orientation of sail as defined by angles α and γ may remain constant relative to the Sun in the rotating frame over one half-period or along an arc, the orientation gradually changes relative to the inertial frame. That is, the hardware must reorient the sail with respect to the inertial frame to maintain constant orientation in relative to the rotating frame. To maintain the orientation relative to the inertial frame, the sail must reorient at approximately one degree per day for an orbit with an estimated period of 180 days.

As a result of the implicit variable time formulation, the period of each orbit differs from that listed in Table 5.1. Observe that the period of the orbit increases and the size of the orbit decreases as the artificial Lagrangian point, L_1, shifts towards the Sun as a result of an increase in the sail lightness parameter, β. The initial x-offset in position of the particle, P_3, from the location of the artificial Lagrangian point is held constant at 200,000 km. The converged planar solution exists and appears in Figures 7.2 for all three values of sail lightness parameter, β. The initial linear two-dimensional guess produced trajectories that departed the vicinity of the artificial Lagrangian point when propagated in the nonlinear model. Orientation angles, α_0 and γ_0 were iteratively corrected to determine a periodic solution with no restriction on limiting the solution to two-dimensional orbit. The solution converged to a planar, periodic trajectory that demonstrates an excursion of 22408 km in the z-direction.

The single shooting variable-time formulation is limited in its applicability because only three design variables are available, α_0, γ_0 and τ. Thus, the constraint vector is limited to a maximum size that is 3×1, which in previous section was limited to

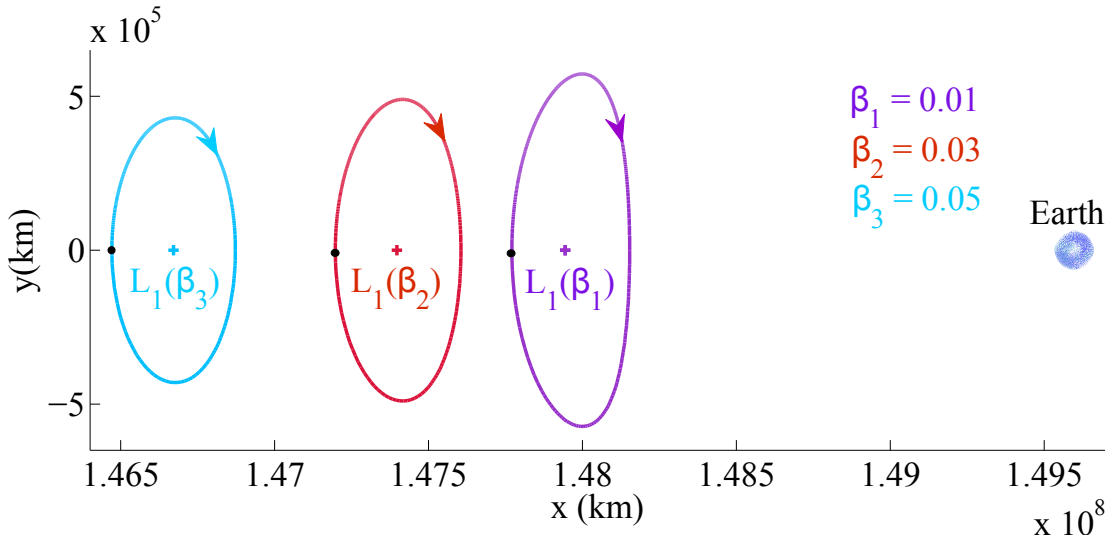

Figure 7.2. Periodic Orbits about Artificial Lagrangian Point, L_1

the final position in y and the final velocity components in x and z direction, $\dot{x}$ and $\dot{z}$ respectively. To find a solution for a more complex scenario or for the option of additional types of constraints, the concept of differential corrections, with sail angles as the available design variables, is further extended to develop a targeting scheme for a set of n discrete points. The baseline trajectory is decomposed into segments that originate from a sequence of patch points. The overall objective is convergence to a path continuous in position and velocity. Such a result is accomplished by varying the orientation angles, α and *gamma*, at each patch point such that the end position and velocity states originating from the $(n-1)^{th}$ patch point merges with the initial position and velocity states along the next segment, i.e., the n^{th} patch point.

7.2 Application for Trajectory Design about Artificial L_1 using Sail Orientation Angles

Reflection of photons from the Sun imparts momentum to the solar sail in an orbit about artificial Lagrangian point. The transfer of momentum result in drifting the spacecraft away from its nominal periodic trajectory and as a consequence, solar

sail spacecraft will depart from the vicinity of the artificial Lagrangian Point. Unless otherwise desired, this departure may result in mission failure and loss of vehicle. Thus, sail orientation is changed to maintain the spacecraft in its periodic or quasi-periodic trajectory about the artificial Lagrangian Point.

As an example, Figure 7.3 shows an orbit about the artificial Lagrangian point L_1 where multiple shooting algorithm is employed to iteratively find a periodic trajectory in the vicinity of L_1. The planar solution for sail parameter, $\beta = 0.05$ is used as an initial guess along with an initial z amplitude of 200,000 km. The number of patch points in this example are six as marked by black dots in Figure 7.3. Note that, the patch points are free to move. In the example presented in Figure 7.3, solar sail angles are allowed to iteratively vary at each patch point to maintain continuity in both position and velocity as demonstrated by the light blue orbit. The period of the corrected orbit in blue is approximately 290 days with an approximate z-amplitude of 46,000 km. The specific sail orientation angles required for a periodic orbit are listed in Table 7.2. Note that, though the angles appear to be small, the sail is completely on when $\alpha = 0^0$. Each set of orientation angle correspond to the orientation at a

Table 7.2 Sail Orientation Angles for Periodic Solution using Multiple Shooting Algorithm

Arc No.	α	γ	Time ($\approx$ days)
Arc 1	0.042^o	0.006^o	6.74
Arc 2	-0.040^o	0.002^o	52.88
Arc 3	0.007^o	0.015^o	60.13
Arc 4	0.102^o	-0.002^o	60.13
Arc 5	-0.005^o	-0.003^o	60.13
Arc 6	-0.032^o	0.007^o	50.56

patch point and remains constant relative to the sun in the rotating frame until the trajectory reaches the subsequent patch point. The example demonstrates that the

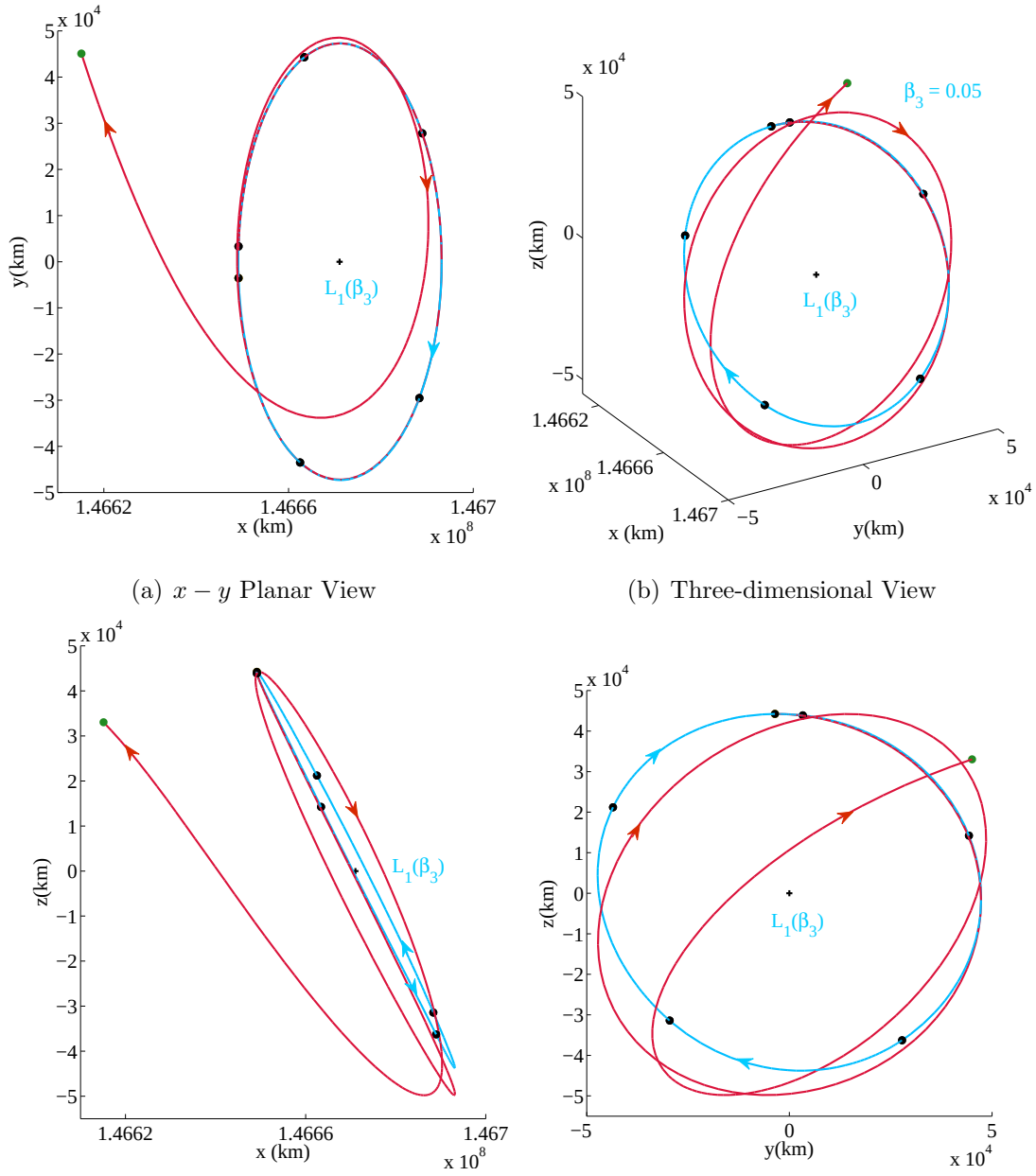

(a) $x - y$ Planar View

(b) Three-dimensional View

(c) $x - z$ Planar View

(d) $y - z$ Planar View

Figure 7.3. Solar Sail Spacecraft Departure from the Vicinity of Artificial L_1.

spacecraft will depart from its periodic trajectory without any additional algorithm for performing trajectory design maneuvers. The departure trajectory is shown in red.

In Section 7.1, periodicity was maintained by applying variable-time single shooting algorithm to achieve a desired orbit. Spacecrafts equipped with solar sail can further utilize sail angles to perform maneuvers over number of revolutions, which otherwise would require thrusters, and thus propellant to perform the adequate maneuver. As, an example, Figure 7.4 shows the application of multiple shooting scheme to maintain a spacecraft for three revolutions. Such an orbit about an artificial Lagrangian point does not exist in the classical CR3BP. The objective of trajectory design, as demonstrated in this example, is to maintain the spacecraft in the vicinity of the artificial Lagrange point, L_1, for a specific duration of time based on mission specifications. A three-dimensional non-periodic trajectory with initial states and solar sail angles (from the planar solution for $\beta = 0.05$ and a z-amplitude of 100,000 km) is provided as an initial guess for the corrections scheme. The corrections algorithm algorithm was used to maintain a nearby trajectory and periodicity, i.e., the initial position and velocity state should be the same as the final position and velocity state after the completion of three revolutions. The sail orientation angles for each patch point are given in Appendix The total time for trajectory is approximately 873 days and completes one revolution in about 291 days. As can be seen from Figure 7.4, the approximate y and z amplitude of the orbit is 50,000 km.

7.3 Offset Periodic Orbits in the Vicinity of Artificial L_1

To extend the application of solar sails, new regions for the existence of periodic orbits is explored. Sail orientation angles can be exploited to produce periodic orbits and to maintain the spacecraft in the vicinity of that orbit by performing orientation maneuvers for trajectory design. The differential corrections scheme applied is specific to maintain continuity in both position and velocity states.

In the example presented in Figure 7.5, multiple shooting scheme is employed to maintain continuity after three revolutions. To check the validity of the multiple shooter, for this example, the number of patch points are two per revolution, thus, a

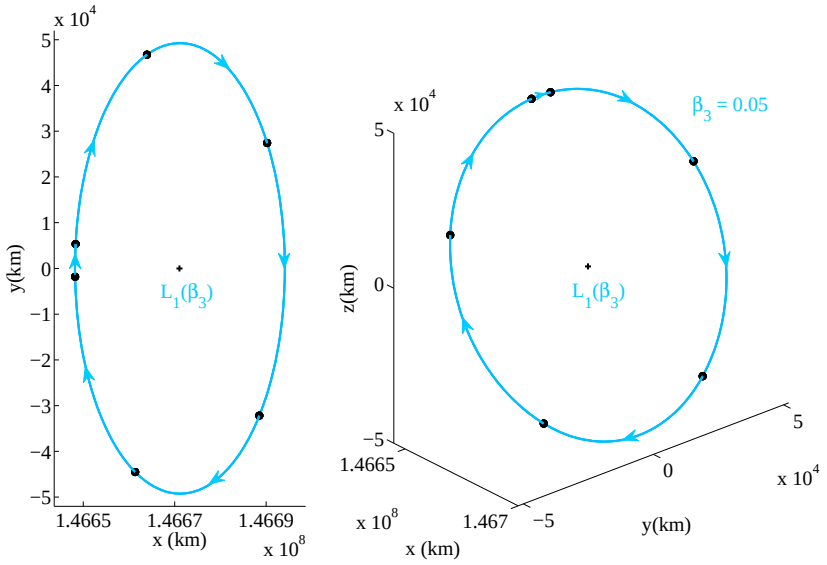

(a) $x - y$ Planar View (b) Three-dimensional View

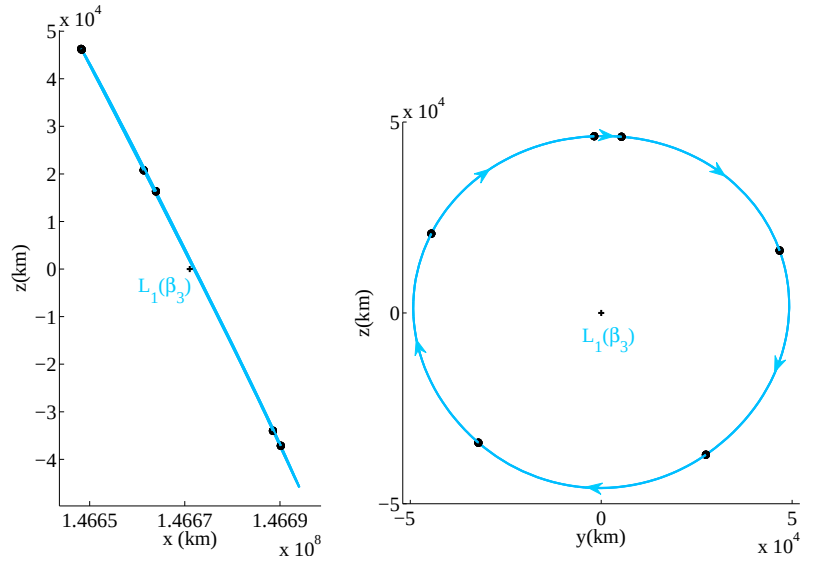

(c) $x - z$ Planar View (d) $y - z$ Planar View

Figure 7.4. Trajectory Design with Sailcraft in the Vicinity of Artificial L_1 for Three Revolutions

total of six for three revolutions. A three-dimensional non-periodic trajectory with a small z-amplitude is used as an initial guess with sail completely turned on, i.e., $\alpha = \gamma \cong 0^o$. Interesting features are displayed by the converged trajectory shown in Figure 7.5. Note that, the black dots indicate the location of patch point and the red dot is

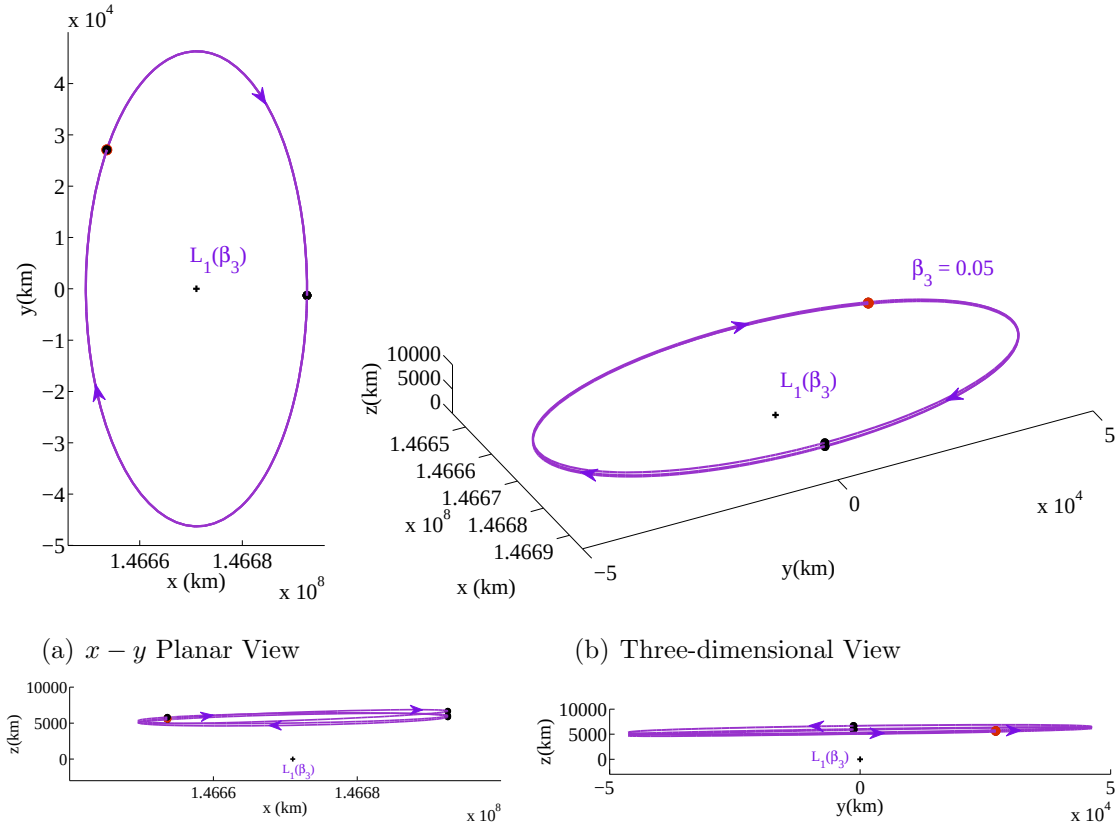

(a) $x - y$ Planar View

(b) Three-dimensional View

(c) $x - z$ Planar View

(d) $y - z$ Planar View

Figure 7.5. Off-Axis Trajectory Design in the Vicinity of Artificial L_1.

the converged initial and final state. A total of six patch points were used over three revolutions to converge the trajectory. Thus, the orientation angle history for the duration of each arc is shown is Table 7.3. The orientation is held constant relative to the Sun in the rotating frame until the next patch point. Upon close examination of Figure 7.5, it s also apparent that the converged patch points are not the same but are relatively close to each other. In this formulation, though the patch points were free to move, the integration time between the patch point is fixed. Thus, fixed-time multiple shooting algorithm was employed to achieve a periodic solution.

The planar $x-y$ view does not provide much insight into the unique nature of the trajectory but further understanding is gained by observing $x - z$ and $y - z$ planar views that exhibit distinct characteristics associated with the trajectory. The three

Table 7.3 Sail Orientation Angles for Offset Periodic Solution

Arc No.	α	γ	Time ($\approx$ days)
Arc 1	0.061^o	0.014^o	117.68
Arc 2	0.061^o	-0.006^o	172.91
Arc 3	0.056^o	0.014^o	117.68
Arc 4	0.060^o	-0.006^o	172.91
Arc 5	0.057^o	0.014^o	117.68
Arc 6	0.058^o	-0.006^o	172.91

period orbit appear to exist about 5,000 km above the $x-y$ plane. The z excursion is approximately 5,000 km where as the y-amplitude is approximately 47,000 km. It is also vital to note that though the trajectory exhibit periodic nature, further propagation without adequate maneuvers will result in departure from the vicinity of the trajectory shown in Figure 7.5.

7.4 Trajectory Design Using Sail Orientation Angles

Solar sails open new regimes for exploring periodic orbits in the vicinity of the collinear Lagrangian points. Solar sail angles are altered to demonstrate the capabilities of a sail and achieve desirable trajectory characteristics. With solar sail technology still in the developmental stages, analyzing the behavior of solar sails with low sail lightness parameters may be more useful in the near term.

7.4.1 y-Amplitude Adjustment of a Trajectory in the Vicinity of L_1

The application of solar sails and the use of orientation angles as design variables is extended to modify the trajectory of planar orbits. Assume that the sail lightness parameter value of $\beta = 0.01$ is selected to model the behavior of a sail in the vicinity of traditional Lagrange point. In Figure 7.6, y-amplitude adjustment of the trajectories

in the vicinity of traditional Lagrange point, L_1 are shown. In certain mission design scenarios, it might be desired to increase the y-amplitude of a planar orbit to meet a specific goal. Such a modification to a Lagrangian point orbit can be achieved simply by reorienting the sail. The orientation angle history for Figure 7.6 is summarized in

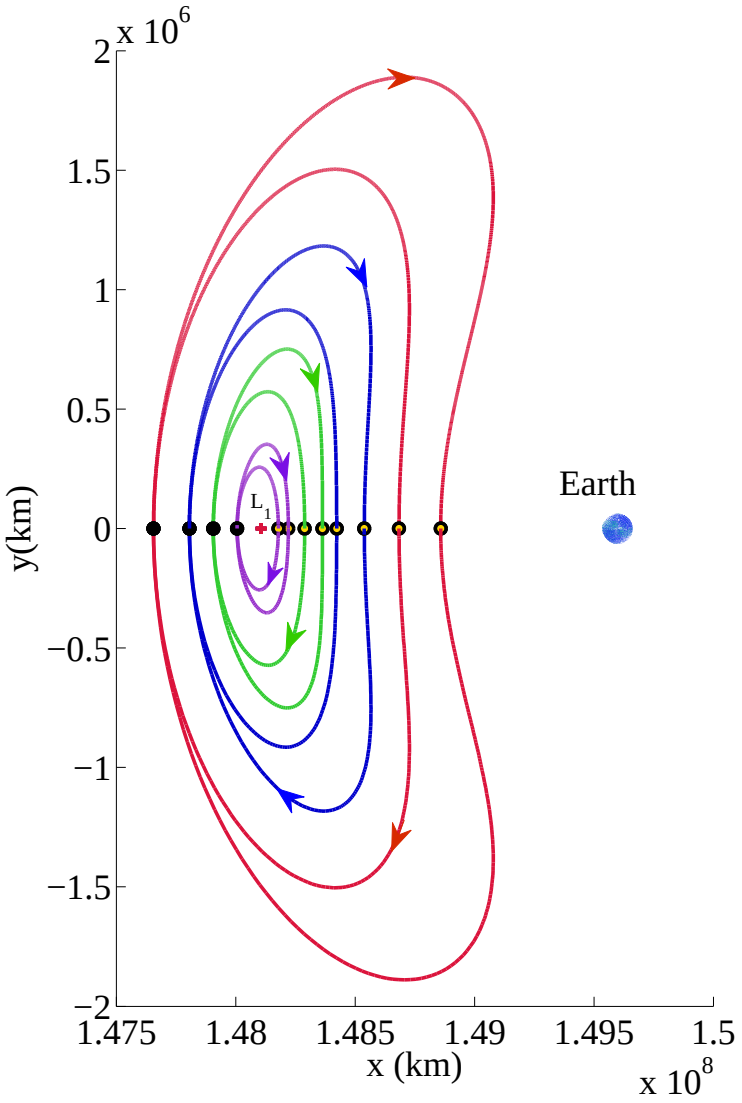

Figure 7.6. y-Amplitude Adjustment of the Trajectories

Table 7.4.

Each color correspond to a trajectory continuous in both the position and the velocity. The black dots denote the initial state and the point for a pair of orbits

Table 7.4 Sail Orientation Angles for y-Amplitude Adjustment

Orbit No.	ξ_0 (km)	$\alpha_0(0 \to 2\tau)$	$\gamma_0(0 \to \tau)$	$\gamma_0(\tau \to 2\tau)$	Period (days)
Purple a	100,000	61.08^o	90^o	-90^o	148.06
Purple b	100,000	76.86^o	-90^o	90^o	183.72
Green a	200,000	54.44^o	90^o	-90^o	160.38
Green b	200,000	66.22^o	-90^o	90^o	191.83
Blue a	300,000	48.54^o	90^o	-90^o	169.28
Blue b	300,000	58.08^o	-90^o	90^o	202.09
Red a	450,000	53.81^o	90^o	-90^o	186.49
Red b	450,000	43.40^o	-90^o	90^o	226.25

where a change in the orientation angles result in a change in the trajectory, i.e., new orbit. Whereas the yellow dots with black circle correspond to the intermediate correction in orientation angle for perpendicular crossing of $\Sigma : y = 0$. Recall, the Earth is magnified ten times its actual size for visualization. Each color shows a long period and short period trajectories which are labeled as orbit a and b respectively in Table 7.4. The integration time corresponding to a half-orbit is τ. As an example, the red trajectory starts from the initial state marked by a solid black dot. The spacecraft starts by moving along the smaller orbit with sail orientation shown in Table 7.4 for orbit number: Red a. After completing one revolution, the sail reorients to alter its path and move along the larger orbit. The orientation of the sail is given by orbit number: Red b as shown in Table 7.4. Varying the sail angles, the vehicle can either be maneuvered from one orbit to another by changing the orientation angle of the sail or can be maintained along the same trajectory. It is also important to note that the change in angle results in a change in time (see Table 7.4) it takes for the trajectory to return to the same initial position and velocity state. The importance of time and location is evident from the perspective of a rendezvous problem. If the spacecraft that is incoming for docking experiences a delay, the docking station, equipped with

solar sails, can alter its trajectory by changing the sail orientation and take a longer route to account for the delay in approach of the incoming spacecraft.

7.4.2 L_1-Earth Cycling Trajectory

Prior to launching a solar sail spacecraft away from the Earth about the artificial Lagrangian points, it is important to test its maneuvering capabilities in Earth's vicinity and in an orbit about the classical Lagrangian points, specifically, L_1. The sample trajectory proposed in this subsection corrects the path of a sail to orbit Lagrangian point, L_1, transition to a trajectory towards the Earth, complete two revolutions about the Earth, and then fly back to same orbit about the Lagrangian point, L_1. The trajectory shown in Figure 7.7 demonstrates the capability of a solar sail to achieve such a path by solely changing the orientation angles of a sail. Specific to this trajectory design, the maneuvers, i.e., changes in sail orientation angles, are performed at the crossing of map $\Sigma : y = 0$.

The initial and the final state, represented by a green dot in Figure 7.7, is located between the Sun and L_1 at a distance of 250,000 km away from L_1 along the Sun-Earth line. The black dots correspond to the intermediate locations of maneuvers that are performed to achieve the designed trajectory. The sequence in which each path is flown is marked by the Leg #. Based on the mission specification, the trajectory can be manipulated using a sail to meet specific mission goals. The proposed trajectory starts from the initial state represented by a green dot and moves along Leg 1 for 101.05 days. After performing a sail orientation maneuver, the spacecraft continues on its path towards the Earth as shown by Leg 2 of the trajectory. Subsequently, after a third sail orientation maneuver, Leg 3 is traversed, completing one revolution about the Earth. After performing additional orientation changes, the spacecraft travels along Leg 4 and Leg 5 before a final reorientation that results in the Leg 6 of the trajectory that brings the spacecraft back to the initial state. Note, that the Earth is magnified 10 times its actual size for visualization purpose. The nearest

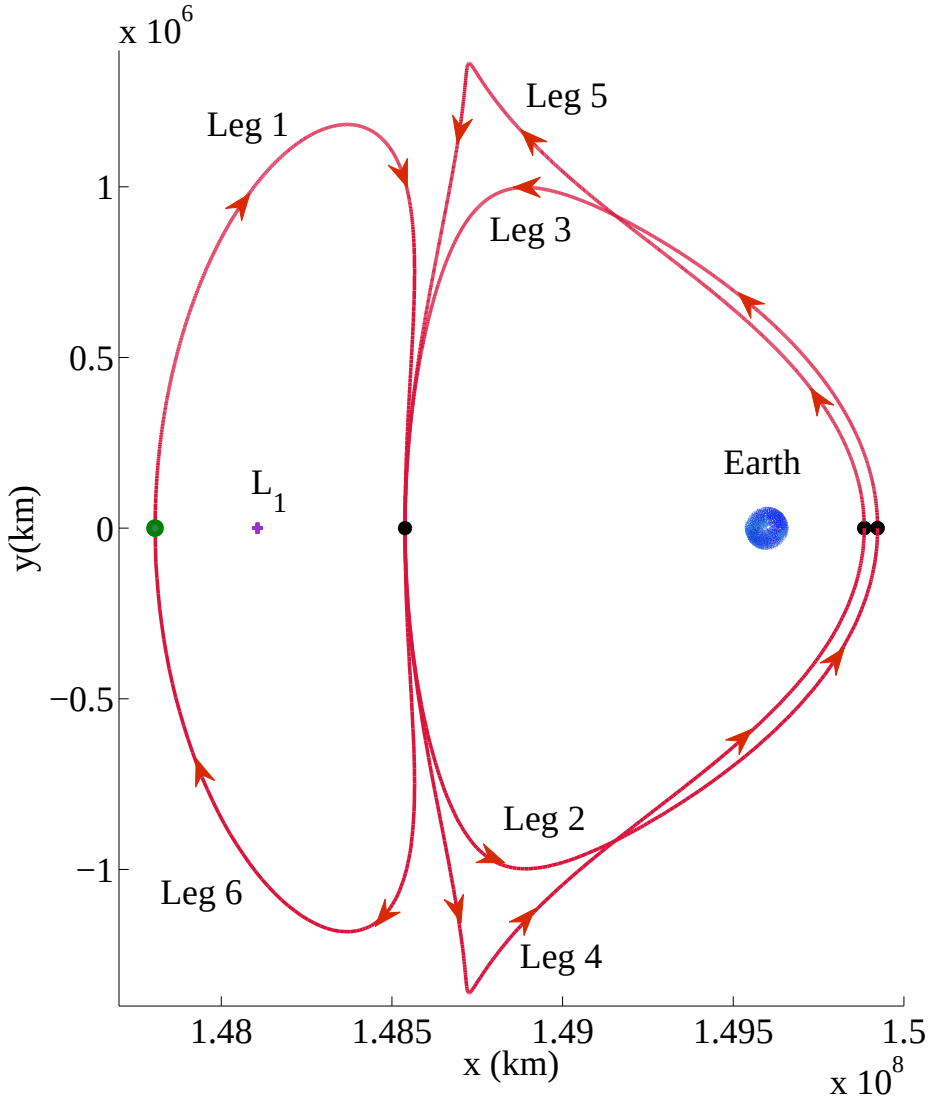

Figure 7.7. L_1-Earth Cycling Trajectory

approach of the trajectory is approximately 279,868 km away from the surface of the Earth. The approach is at a distance that is closer than the Moon's mean orbital radius, thus, a higher fidelity model may be necessary for further analysis to account for the gravitational influence of the moon. The orientation history for the sail angles and the time of flight for each leg is shown in table 7.5.

The total time of flight to complete one cycle, i.e., returning back to the initial state as shown in Figure 7.7, is 563.35 days. The algorithm for the proposed trajectory

Table 7.5 Sail Orientation Angles for L_1-Earth Cycling Trajectory

Leg No.	α	γ	TOF (days)
Leg 1	58.08^o	-90^o	101.05
Leg 2	29.58^o	-90^o	71.63
Leg 3	29.58^o	90^o	71.63
Leg 4	23.15^o	90^o	108.99
Leg 5	23.15^o	-90^o	108.99
Leg 6	58.08^o	-90^o	101.05

is currently designed to perform two revolutions of the Earth and return back to the initial state in an orbit about the L_1. Upon returning, the trajectory continues to follow the same path with the same orientation angle sequence as outlined in the Table 7.5. The algorithm is capable of increasing the number of revolutions either about the L_1 or in an orbit about the Earth and still return to its initial state after the completion of trajectory excursions. The proposed trajectory verifies the application of a solar sail for designing a trajectory that is capable of maintaining a spacecraft in a certain orbit or evolving a trajectory specific to a mission. Such a trajectory demonstrates the capability of a sailcraft to alter the periapsis or provide contingency options for a spacecraft to return back to the Earth in case of an emergency while enroute to an orbit about the L_1.

7.4.3 Earth-L_1 Halo-Earth Return Trajectory with Solar Sail

Halo orbits in the vicinity of L_1 Lagrangian point are of significant scientific interest. In the proposed example, the spacecraft, equipped with solar sail, departs along the trajectory outlined by the SS-CR3BP dynamics and arrive in a low inclination halo orbit. A sample departure from the vicinity of Earth is shown in Figure 7.8. In the illustration presented, the spacecraft leaves the vicinity of the Earth from a

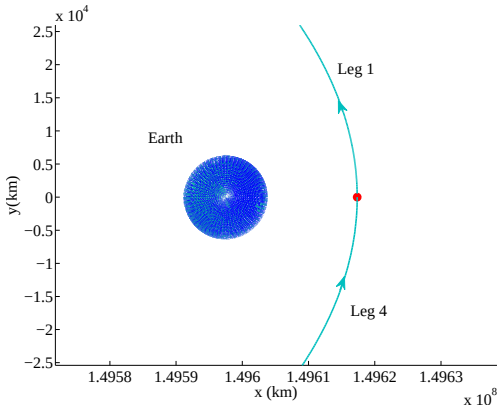

Figure 7.8. Departure from Earth's Orbit

medium earth orbit (MEO) at an altitude of approximately 13,525 km in the x direction and -117 km in z direction. The red dot indicates the departure location from the vicinity of the Earth in the direction as indicated in Figure 7.8. The orbital speed at an altitude of 13524 km is approximately 4.48 km/s. Thus, to depart along the indicated trajectory, an initial boost of 1.79 km/s is required to raise the velocity of the sailcraft to 6.24 km/s and continue along the trajectory outlined by Leg 1.

Complete trajectory for departure and arrival at a halo orbit is shown in Figure 7.9. On arrival, there is no cost associated with the insertion into the halo orbit. Sail orientation angles are changed in order to accomplish the desired insertion and follow a periodic trajectory about the L_1.

The orientation history for the sail angles is shown in Table 7.6 It is evident from Figure 7.9(b) that the halo orbit demonstrates a small excursion in the z-direction. During the transition phase between Leg 2 and Leg 3, the sail reorients itself such that the angle γ switches from 74.68^o to -74.68^o. Once again, this is a change in the projection of the sail normal vector, $\hat{n}$ and not an actual reorientation by 149.36^o. An equivalent change in α is of 130.72^o. Based on the maximum turn rate of $0.02^o/s$, the sail would take approximately 109 minutes to reorient itself. Comparing the time to reorient with the time of flight for that particular segment (Leg 3), the orientation time is less than 0.08% of the segment flight time. Thus, it is appropriate to assume

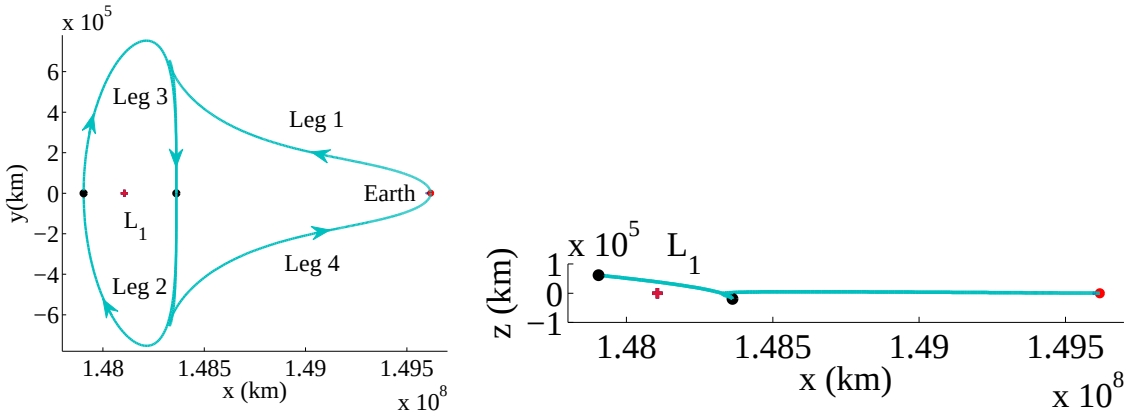

(a) $x - y$ Planar View

(b) $x - z$ Planar View

Figure 7.9. Projections for Three-Dimensional Trajectory about L_1

Table 7.6 Earth to L_1 Halo Return Trajectory with Solar Sail

Leg No.	α	γ	TOF (days)
Leg 1	66.30^o	100.00^o	89.79
Leg 2	65.36^o	74.68^o	96.18
Leg 3	65.36^o	-74.68^o	96.18
Leg 4	66.30^o	-100.00^o	89.79

that the change in orientation is instantaneous. Based on the mission specification, the orientation angles are selected to either maintain the solar sail in an orbit about the Lagrangian point, L_1, or perform a number of revolutions about the L_1 and eventually return back to the vicinity of the Earth. The sample mission design shown in Figure 7.9 leaves the vicinity of the Earth, performs one revolution about the L_1, and then departs along Leg 4 back to the vicinity of the Earth. Such a trajectory also demonstrates the capability of a sailcraft to be able to depart from various altitudes and enter a halo orbit of different sizes. It also provides contingency options for a spacecraft to return back to the Earth in case of an emergency while enroute to an orbit about the L_1. The orientation angles and the time of flight for each leg is

indicated in Table 7.6. Thus, the total time of flight to complete the sample mission is 371.94 days.

7.4.4 Three-Dimensional Trajectory Design about L_1 Lagrangian Point: z-Amplitude Adjustment

To expand the trajectory design tool kit using sail angles, it is desirable to look into three-dimensional trajectories. As an example, a mission may require a trajectory to have a variable z-amplitude to meet specific objective. To compute a three-dimensional trajectory, an initial state is selected between the Sun and L_1 at a distance of 200,000 km away from L_1. A z-amplitude of 10,000 km is added to the initial state. A linear guess for velocity is generated and a corrections scheme is applied. Initial and final state of the trajectory are marked by a green dot as shown in Figure 7.10. The converged trajectory follows a path that resembles the trajectory of three different halo orbits. In Figure 7.10, the black dots correspond to the locations where orientation angles are changed prior to the following Leg. As the sail-based spacecraft moves along a particular Leg, the orientation angles remain fixed relative to the Sun in the rotating frame until the trajectory reaches the subsequent maneuver location. Planar projections of the traversed trajectory are shown in Figure 7.11. The orientation angles and the time of flight for each Leg of the trajectory is given in Table 7.7.

Though it may appear that the sail angle, γ, reorients itself from -169.74^o to 169.74^o, this is simply a change in the projection. In other words, angle α reorients by 62.2^0. Thus, the time to reorient the spacecraft is 52 minutes for α. Compared to the time of flight for Leg 5, the reorientation time is only 0.02% of the total time for that Leg. Thus, it is appropriate to assume instantaneous change in sail angle for the preliminary analysis presented in this work. The total time of flight to complete one cycle, i.e. traverse the trajectory shown by three halos, is approximately 563 days. If the algorithm is propagated for longer duration of time, the spacecraft will traverse

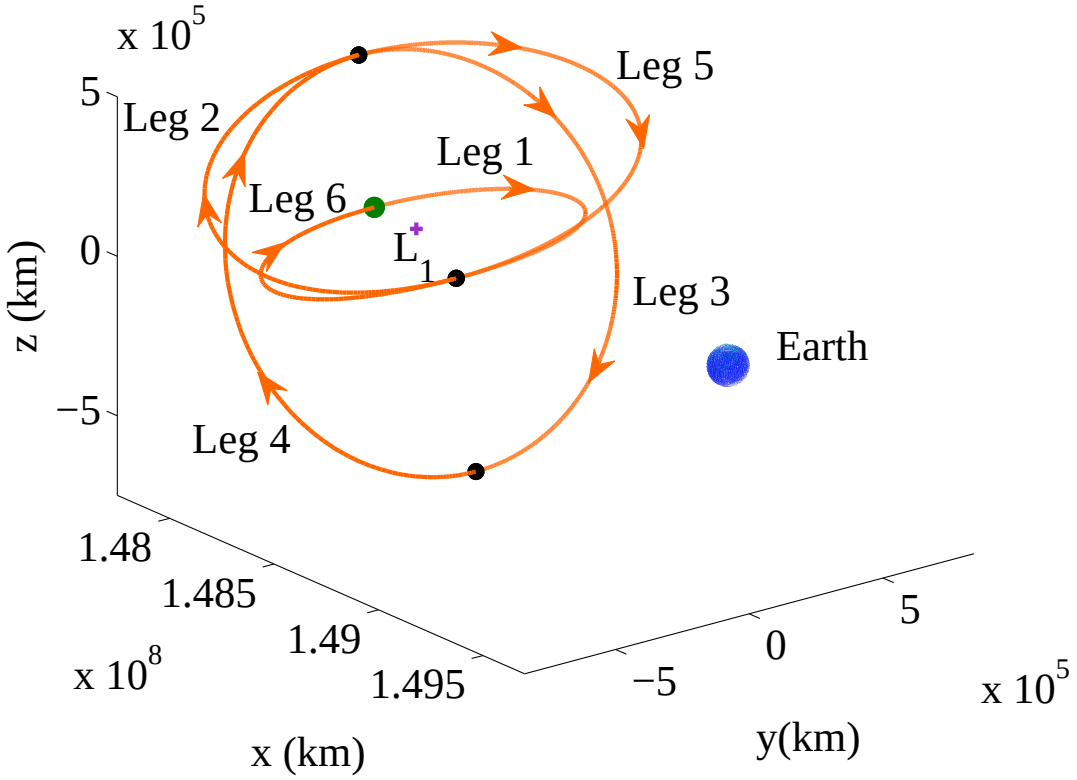

Figure 7.10. Three-Dimensional y-Amplitude Adjustment about L_1

Table 7.7 Sail Orientation Angles for y-Amplitude Adjustment in the Vicinity of L_1

Leg No.	α	γ	TOF (days)
Leg 1	55.18^o	118.85^o	81.48
Leg 2	34.54^o	27.81^o	93.78
Leg 3	31.10^o	-169.74^o	106.1
Leg 4	31.10^o	169.74^o	106.1
Leg 5	34.54^o	-27.81^o	93.78
Leg 6	55.18^o	-118.85^o	81.48

the same trajectory with the same orientation angle history. The proposed trajectory provides flexibility to either remain in a low z-amplitude orbit or transition to a higher amplitude orbit, or traverse the whole trajectory multiple times. Thus, based

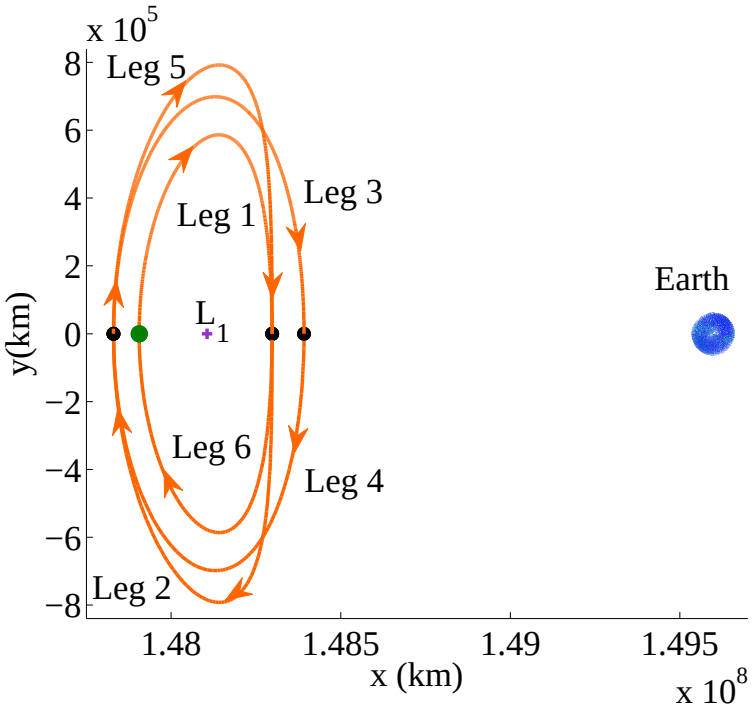

(a) $x - y$ Planar View

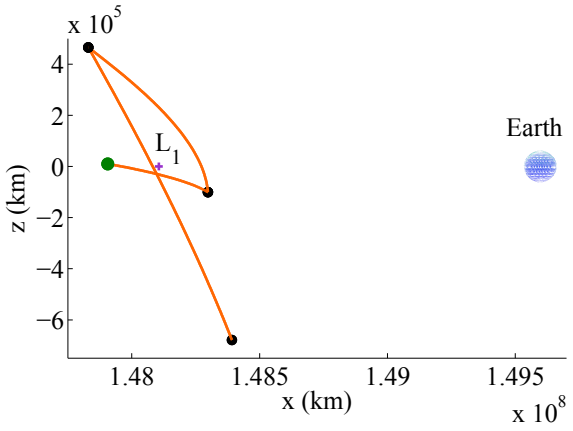

(b) $x - z$ Planar View

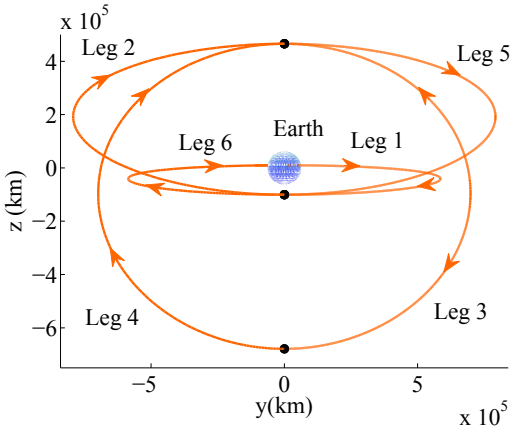

(c) $x - z$ Planar View

Figure 7.11. Projections for Three-Dimensional Trajectory y-Amplitude Adjustment about L_1

on mission specification and the orientation history provided in Table 7.7, the sail angle maneuvers can be scheduled to reorient at the maneuver locations and achieve the desired Leg.

Based on the results, it is evident that the use of solar sail provides the spacecraft with certain abilities that lie beyond the reach of the spacecraft within classical CR3BP. The examples provided in this section demonstrate new design capabilities with solar sail for planar as well as three-dimensional trajectories. Further research and development in the field of solar sail technology can assist in an efficient trajectory design to meet mission goal, thus, realizing the true potential of solar sails.

8. SUMMARY AND RECOMMENDATIONS

This chapter summarizes the findings and results of a preliminary investigation of the effects of incorporating a solar sail force model into the circular restricted three-body problem. Concluding remarks are made on the results of this investigation, and recommendations are provided to further extend the scope and validity of this work.

8.1 Summary

In this investigation, the motion of a spacecraft equipped with solar sail is examined under the gravitational as well as solar radiation influence. As a result of incorporating the solar sail model, the locations of the collinear artificial Lagrangian points are variable within the limits on the sail lightness parameter available with the current technology. The size and location of a periodic orbit in the vicinity of the collinear Lagrangian point, L_1, is varied, with possible mission application allowing observation of the Sun from a closer distance than the classical L_1 point. The closer location for observing solar weather would facilitate the early detection of potentially hazardous solar flares and solar winds. Preliminary analysis is carried out to analyze the solar sail acceleration that can be achieved based on the sail lightness parameter the total mass of spacecraft. A decrease in the efficiency of the sail led to a higher requirement for the total sail area to achieve the same level of acceleration. If the total sail area is kept constant, the total amount of load that the sail can carry decreases or the acceleration due to the radiation pressure decreases.

Stability information corresponding to the displaced collinear Lagrangian points is derived based on the linear model of the Solar Sail Circular Restricted THREE-Body Problem (SS-CR3BP). Analysis of the quintic root revealed that the linear solar sail model exhibits the same stability characteristics that of a classical CR3BP

model. Thus, linear initial conditions are generated that correspond to the linearized periodic orbits in the vicinity of the collinear Lagrangian point, L_1. An augmented state transition matrix is introduced that describes variations in the position and velocity states as a result of changes in the initial state including the initial sail orientation angles. Differential corrections schemes are developed that utilize the solar sail orientation angles s the available controls to target a trajectory with the desired characteristics.

Initial conditions from the linear SS-CR3BP model are located and are employed as the initial guess for a differential corrections process to locate periodic orbits. Changes in the sail lightness parameter are explored, and yields a change in both the size and the period of an orbit in the vicinity of an artificial Lagrangian point, L_1. Sail orientation angles are employed for trajectory design to maintain a spacecraft in the vicinity of the artificial L_1 Lagrangian point for an extended duration. Using this technique, a sample offset three-dimensional, unsymmetric trajectory is located that hovers above the artificial Lagrangian point. The existence of this orbit is a result of incorporating the solar sail model and cannot be achieved within the scope of classical CR3BP.

The solar sail orientation angles prove to be important design tools in the SS-CR3BP model. Incorporating the solar sail model reveals orbit transformations between planar orbits in the vicinity of L_1. By varying the solar sail orientation angles, a spacecraft is capable of transitioning between orbits of different y-amplitude and varying periodicity. A cycling trajectory between the Earth and L_1 is proposed for preliminary analysis to understand and exploit the advantages of solar sails. The proposed mission transitions from an orbit about the L_1 equilibrium point to an orbit about the Earth, where two revolutions are made before going back into an orbit about L_1. This behavior is repeated and the number of revolutions are controlled based on mission specifications.

The sail orientation angles are used as design variables for the purpose of demonstrating the capability of a sail for a three-dimensional trajectory design. Thus, the

ability to transition between the halo orbits of varying z-amplitude is also shown. Finally, a sample transfer from a medium Earth orbit (MEO) is presented that exploits the solar sail capabilities to transfer from a MEO, enter into a low inclination halo orbit about the L_1 and returns back to the same MEO about the Earth. The behavior is repeatable and the number of revolutions in the orbit about L_1 are controlled by the orientation angles. After completing the desired number of revolutions, the sail is reoriented to enter a Leg that delivers the spacecraft back to the vicinity of the Earth.

8.2 Recommendations for Future Work

This investigation is a preliminary analysis on the inclusion of a solar sail model into the circular restricted three-body problem. The purpose of this work is to lay the foundation to further research in solar sail technology.

The proposed trajectories in this investigation are in the vicinity of Earth and the Lagrangian point L_1 prior to extending the investigation to artificial Lagrangian points. It is assumed that the sail angle orientation can be changed instantaneously as the relative time frame of the Sun-Earth system is large when compared to the time to reorient a sail. Including the time for rotation into the dynamical model can given a more realistic feel for trajectory and, thus, provide a better approximation. Further investigation of the off-axis Lagrangian points will provide insight into the types of orbits that exist in these regions. It is also of interest to place a solar sail spacecraft at an artificial Lagrangian point L_3 to provide complete coverage of the variations in the solar atmosphere at all time. Positing a sail at L_3 can aid in the prediction of solar flares, and in monitoring solar weather phenomenon that may pose as a potential hazard to Earth.

To date, only one spacecraft, IKAROS by JAXA, was successfully able to harness solar radiation pressure (SRP) as a means of propulsion. Though the acceleration due to SRP is of the order 10^{-6} m/s^2 for the current available technology, the ac-

celeration can provide velocity accumulation required for deep space missions. Solar sail technology can be applied to visit the inner plants, such as IKAROS, or to move closer to the Sun for scientific observation, or to facilitate a mission to the asteroids.

Replacing the CR3BP with an ephemeris model will increase the accuracy of the model and provide new solutions. Further research in the development of solar sail technology is recommended to improve on the sail lightness parameter. An improved sail lightness parameter will open up even more regimes and shift the Lagrangian point closer to the Sun which can prove to be of greater importance for much earlier and accurate detection of solar weather.

A catalog of available solutions for a variety of sail parameter values would be useful to determine an appropriate sail for a specific mission. Further study of the sail lightness parameter could help motivate the development of a sail possessing variable sail lightness parameter to enhance the dynamical regimes in which the sail can function. Variable lightness parameter sail also require the development of a differential corrections algorithm employing β as a control variable. Much more research and development of solar sail technology is required, and such efforts are motivated by propulsion needs of missions that are prohibitively expensive in terms of fuel. Thus, solar sail technology is a technology of the future, applicable to both near and far missions that is capable of attaining great velocities over time and lower the cost associated with the mission.

8.3 Conclusions

The solar sail model provides the capability to successfully harness the solar radiation pressure. The applications of solar sails are investigated from a mission design perspective. New artificial Lagrangian points are found, periodic trajectories in their vicinity are located and investigated. Solar sail prove an effective tool for trajectory design and the computation of the offset periodic orbits from the $x-y$ plane. The sail orientation angles provide the capability to transfer between orbits of different size

and period. Transfer from the vicinity of the Earth to a halo orbit about the artificial L_1 point further demonstrated the application of a solar sail. Further research and investigation will yield new ideas for the application of solar sails that can assist in taking the concept of human space exploration to a new level.

LIST OF REFERENCES

LIST OF REFERENCES

[1] I. Newton, *The Principia: The Mathematical Principles of Natural Philosophy (1687)*. Berkeley, California: University of California Press, 1999. Translation by I. B. Cohen and A. Whitman.

[2] B. T. Barden and K. C. Howell, "Fundamental Motions Near Collinear Libration Points and Their Transitions," *The Journal of the Astronautical Sciences*, vol. 46, no. 4, pp. 361–378, 1998.

[3] K. Howell, *Three-Dimensional, Periodic 'Halo' Orbits in the Restricted Three-Body Problem*. Department of Aeronautics and Astronautics, Stanford University, Stanford, California: Ph.D. Dissertation, 1983.

[4] J. Benford and G. Benford, "Near-Term Beamed Sail Propulsion Mission: Cosmos-1 and Sun-Diver," *American Institute of Physics Conference Proceedings*, vol. 664, no. 1, pp. 358–368, 2003.

[5] V. Szebehely, *Theory of Orbits: The Restricted Problem of Three Bodies*. New York: Academic Press, 1967.

[6] C. G. J. Jacobi, "Sur le Mouvement d'un Point et sur un cas Particulier du Problème des Trois Corps," *Comptes Rendus de l'Acadmie des Sciences de Paris*, vol. 3, pp. 59–61, 1836.

[7] D. L. Richardson, "Analytic Construction of the Periodic Orbits About the Collinear Points," *Celestial Mechanics*, vol. 22, pp. 241–253, 1980.

[8] K. C. Howell and J. Breakwell, "Almost Rectilinear Halo Orbits," *Celestial Mechanics*, vol. 32, pp. 29–52, 1984.

[9] K. C. Howell, "Three-Dimensional, Periodic, 'Halo' Orbits," *Celestial Mechanics*, vol. 32, pp. 53–72, 1984.

[10] R. W. Farquhar, D. P. Muhonen, and D. L. Richardson, "Mission Design for a Halo Orbiter of the Earth," *Journal of Spacecraft and Rockets*, vol. 14, pp. 170–177, 1977.

[11] National Aeronautics and Space Administration, "NSSDC Master Catalog Search: Spacecraft Query." `http://nssdc.gsfc.nasa.gov/nmc/SpacecraftQuery.jsp`. Online: accessed 19-July-2012.

[12] National Aeronautics and Space Administration, "Comprehensive Solar Wind Laboratory for Long-Term Solar Wind Measurements." `http://wind.nasa.gov/`, 1994. Online: accessed 19-July-2012.

[13] C. McInnes, *Solar Sailing, : Technology, Dynamics and Mission Applications*. Chichester, United Kingdom: Springer - Praxis, 1999.

[14] P. Lebedew, "The Physical Causes of the Deviation from Newton's Law of Gravitation," *Astrophysical Journal*, vol. 10, pp. 155–161, 1902.

[15] F. A. Tsander, *From a Scientific Heritage, NASA Technical Translation TTF-541, 1967, A Translation of Iz Nauchnogo Naslediya*. Moscow: Nauca Press, 1924.

[16] J. Wright, "Solar Sailing: Evaluation of Concept and Potential," Tech. Rep. BMI-NLVP-TM-74-3, Battelle Memorial Institute Report, 1974.

[17] D. Coulter, "A Brief History of Solar Sails." `http://wind.nasa.gov/`, 2008. Online: accessed 07-August-2012.

[18] M. Kaplan, "Planetary Society to Sail Again with LightSail." `http://www.planetary.org/press-room/releases/2009/1109_Planetary_Society_to_Sail_Again_with.html`, 2009. Online: accessed 06-February-2012.

[19] O. Mori, Y. Tsuda, H. Sawada, R. Funase, T. Yamamoto, T. Saiki, K. Yonekura, H. Hoshino, H. Minamino, T. Endo, and J. Kawaguchi, "World's First Demonstration of Solar Power Sailing by IKAROS," proceedings of the second International Symposium on Solar Sailing (ISSS 2010), The New York City College of Technology of the City University of New York, New York, 2010.

[20] B. Wie, *Space Vehicle Dynamics and Control*. Reston, Virginia: American Institute of Aeronautics and Astronautics, Inc., 1998.

[21] J. Barrow-Green, "Poincaré and the Three Body Problem," *History of Mathematics, American Mathematical Society*, vol. 11, 1997.

[22] D. A. Vallado, *Fundamentals of Astrodynamics and Applications*. New York: Springer-Verlag, 2007.

[23] G. Gómez, J. Llibre, R. Martínez, and C. Simó, *Dynamics and Mission Design Near Libration Points, Vol. I Fundamental: The Case of Collinear Libration Points*. Singapore: World Scientific, 2001.

[24] V. G. Szebehely, "Theory and Application of Motion Around Equilibrium Positions," *Progress in Astronautics and Aeronautics*, vol. 17, pp. 3–30, 1966.

[25] A. M. Lyaponov, *The General Problem of the Stability of Motion (1892)*. London: Taylor and Francis, 1994. Translation by A. T. Fuller.

[26] W. S. Levine, *The Control Handbook*. Boca Raton, Florida: CRC Press, 1996.

[27] K. Howell, *Advanced Orbital Dynamics*. 2010.

[28] K. E. Tsiolkovsky, *Extension of Man into Outer Space, 1921 [Also, Konstantin E. Tsiolkovsky, K. E. Symposium Jet Propulsion, No. 2]*. Moscow: United Scientific and Technical Presses, 1936.

[29] C. Wiley, "Clipper Ships of Space," *Astounding Science Fiction*, p. 135, 1951. [Pseudonym: Russell Sanders].

[30] R. L. Garwin, "Solar Sailing - A Practical Method of Propulsion within the Solar System," *Jet Propulsion*, vol. 28, pp. 188–190, 1958.

[31] W. Seboldt, M. Leipold, M. Rezazad, L. Herbeck, W. Unkenbold, D. Kassing, and M. Eiden, "Ground-Based Demonstration of Solar Sail Technology," Proceedings of 51st International Astronautical Congress IAF-00-S.6.11, Rio de Janeiro, 2000.

[32] M. Leipold, C. Sickinger, and H. Runge, "Large SAR Membrane Antennas with Lightweight Deployable Booms," *28th ESA Antenna Workshop on Space Antenna Systems and Technologies, ESA/ESTEC*, 2005.

[33] F. Lura, U. Geppert, B. Biering, and R. Reinhard, "The Three-Step Gossamer Road Map to Solar Sailing," proceedings of the second International Symposium on Solar Sailing (ISSS 2010), The New York City College of Technology of the City University of New York, New York, 2010.

[34] D. Lichodziejewski, J. West, R. Reinert, K. Belvin, R. Pappa, and B. Derbes, "Bringing an Effective Solar Sail Design Towards TRL 6," Tech. Rep. AIAA 2003-4659, 2003. AIAA Joint Propulsion Conference.

[35] Japan Aerospace Exploration Agency (JAXA), "IKAROS: International Astronautical Congress (IAC)." `http://upload.wikimedia.org/wikipedia/commons/1/17/IKAROS_IAC_2010.jpg`, 2010. Online: accessed 30-September-2011.

[36] Japan Aerospace Exploration Agency (JAXA), "The Worlds First Successful Shootings of the Solar Power Sail Deployment!." `http://www.jspec.jaxa.jp/ikaros_channel/e/bn006.html`, 2010. Online: accessed 30-September-2011.

[37] D. Higginbotham, "National Aeronautics and Space Administration." `http://www.nasa.gov/mission_pages/smallsats/nsd_bluesail.html`, 2008. Online: accessed 01-November-2011.

[38] Bruce Betts, "LightSail Presented at Aerospace Mechanisms Symposium." `http://www.planetary.org/blogs/bruce-betts/20120531-LightSail-Biddy-Presentation.html`, 2012. Online: accessed 06-November-2012.

[39] O. Mori, Y. Shirasawa, Y. Miyazaki, H. Sakamoto, M. Hasome, N. Okuizumi, H. Sawada, H. Furuya, S. Matunaga, M. Natori, Y. Natori, T. Saiki, R. Funase, Y. Mimasu, and J. Kawaguchi, "Deployment and Steering Dynamics of Spinning Solar Sail "IKAROS"," tech. rep., Japan Aerospace Exploration Agency, Kanagawa, Japan, 2010.

[40] J. S. Nuss, *The Use of Solar Sails in the Circular Restricted Problem of Three Bodies*. School of Aeronautics and Astronautics, Purdue University, West Lafayette, Indiana: M. S. Thesis, 1998.

[41] A. I. S. McInnes, *Strategies for Solar Sail Mission Design in the Circular Restricted Three-Body Problem*. School of Aeronautics and Astronautics, Purdue University, West Lafayette, Indiana: M. S. Thesis, 2000.

[42] B. Wei, "Solar Sail Attitude Control and Dynamics, Part 2," *Journal of Guidance, Control, and Dynamics*, vol. 27, no. 4, pp. 536–544, 2004.

APPENDICES

Appendix A: Partial Derivatives of Solar Sail Acceleration Relative to the Position Coordinates

The partial derivatives of the scalar solar sail acceleration components relative to the position coordinates in the Sun-Earth rotating frame are listed below. The a_{Sail-i_j} terms correspond to the partial derivatives of the scalar solar sail acceleration components in the i^{th} unit direction vector of the rotating frame with respect to the j^{th} position coordinate in the rotating frame. The angles associated with the solar sail, i.e., α and γ, are assumed to be independent of the position coordinates.

$$a_{Sail-x_x} = \beta\frac{(1-\mu)}{d^2}Cos^2\alpha\left\{-2\frac{(x+\mu)}{d^2}n_x + Cos\alpha\frac{(y^2+z^2)}{d^3}\right.$$
$$\left. -Sin\alpha Cos\gamma\frac{y(x+\mu)}{|(\vec{d}\times\hat{z})|^3} + Sin\alpha Cos\gamma\frac{z((x+\mu)^4 - y^2z^2 - y^2)}{|(\vec{d}\times\hat{z})\times\vec{d}|^3}\right\} \quad (A.1)$$

$$a_{Sail-x_y} = \beta\frac{(1-\mu)}{d^2}Cos^2\alpha\left\{-2\frac{y}{d^2}n_x - Cos\alpha\frac{(x+\mu)y}{d^3} + Sin\alpha Cos\gamma\frac{(x+\mu)^2}{|(\vec{d}\times\hat{z})|^3}\right.$$
$$\left. +Sin\alpha Cos\gamma\frac{(x+\mu)yz(2(x+\mu)^2+2y^2+z^2)}{|(\vec{d}\times\hat{z})\times\vec{d}|^3}\right\} \quad (A.2)$$

$$a_{Sail-x_z} = \beta\frac{(1-\mu)}{d^2}Cos^2\alpha\left\{-2\frac{z}{d^2}n_x - Cos\alpha\frac{(x+\mu)z}{d^3}\right.$$
$$\left. -Sin\alpha Cos\gamma\frac{(x+\mu)((x+\mu)^2+y^2)^2}{|(\vec{d}\times\hat{z})\times\vec{d}|^3}\right\} \quad (A.3)$$

$$a_{Sail-y_x} = \beta\frac{(1-\mu)}{d^2}Cos^2\alpha\left\{-2\frac{(x+\mu)}{d^2}n_y - Cos\alpha\frac{(x+\mu)y}{d^3} - Sin\alpha Cos\gamma\frac{y^2}{|(\vec{d}\times\hat{z})|^3}\right.$$
$$\left. +Sin\alpha Cos\gamma\frac{(x+\mu)yz(2(x+\mu)^2+2y^2+z^2)}{|(\vec{d}\times\hat{z})\times\vec{d}|^3}\right\} \quad (A.4)$$

$$a_{Sail-y_y} = \beta\frac{(1-\mu)}{d^2}Cos^2\alpha\left\{-2\frac{y}{d^2}n_y + Cos\alpha\frac{((x+\mu)^2+z^2)}{d^3} + Sin\alpha Sin\gamma\frac{(x+\mu)y}{|(\vec{d}\times\hat{z})|^3}\right. \tag{A.5}$$

$$\left. + Sin\alpha Cos\gamma\frac{z(((x+\mu)^2(z^2+(x+\mu)^2-y^4))}{|(\vec{d}\times\hat{z})\times\vec{d}|^3}\right\} \tag{A.6}$$

$$a_{Sail-y_z} = \beta\frac{(1-\mu)}{d^2}Cos^2\alpha\left\{-2\frac{z}{d^2}n_y - Cos\alpha\frac{yz}{d^3} - Sin\alpha Cos\gamma\frac{y((x+\mu)^2+y^2)^2}{|(\vec{d}\times\hat{z})\times\vec{d}|^3}\right\}$$

$$a_{Sail-z_x} = \beta\frac{(1-\mu)}{d^2}Cos^2\alpha\left\{-2\frac{(x+\mu)}{d^2}n_z - Cos\alpha\frac{(x+\mu)z}{d^3}\right.$$

$$\left. + Sin\alpha Cos\gamma\frac{(x+\mu)((x+\mu)^2+y^2)z^2}{|(\vec{d}\times\hat{z})\times\vec{d}|^3}\right\} \tag{A.7}$$

$$a_{Sail-z_y} = \beta\frac{(1-\mu)}{d^2}Cos^2\alpha\left\{-2\frac{y}{d^2}n_z - Cos\alpha\frac{yz}{d^3} + Sin\alpha Cos\gamma\frac{((x+\mu)^2+y^2)yz^2}{|(\vec{d}\times\hat{z})\times\vec{d}|^3}\right\} \tag{A.8}$$

$$a_{Sail-z_z} = \beta\frac{(1-\mu)}{d^2}Cos^2\alpha\left\{-2\frac{z}{d^2}n_z + Cos\alpha\frac{((x+\mu)^2+y^2)}{d^3}\right.$$

$$\left. - Sin\alpha Cos\gamma\frac{((x+\mu)^2+y^2)^2z}{|(\vec{d}\times\hat{z})\times\vec{d}|^3}\right\} \tag{A.9}$$

Appendix B: Partial Derivatives of Solar Sail Acceleration Relative to the Sail Angles, α and γ

The partial derivatives of the scalar solar sail acceleration components relative to the sail angles, α and γ, in the Sun-Earth rotating frame are listed below. The a_{Sail-i_j} terms correspond to the partial derivatives of the scalar solar sail acceleration components in the i^{th} unit direction vector of the rotating frame with respect to the j^{th} angle corresponding to the solar sail angles, α and γ, in the rotating frame.

$$a_{Sail-x_\alpha} = \beta\frac{(1-\mu)}{d^2}Cos\alpha\left\{-3Cos\alpha Sin\alpha\frac{(x+\mu)}{d^2} + (1-3Sin^2\alpha)Sin\gamma\frac{y}{|(\vec{d}\times\hat{z})|^3}\right.$$
$$\left. -(1-3Sin^2\alpha)Cos\gamma\frac{(x+\mu)z}{|(\vec{d}\times\hat{z})\times\vec{d}|^3}\right\} \tag{B.1}$$

$$a_{Sail-y_\alpha} = \beta\frac{(1-\mu)}{d^2}Cos\alpha\left\{-3Cos\alpha Sin\alpha\frac{y}{d^2} - (1-3Sin^2\alpha)Sin\gamma\frac{(x+\mu)}{|(\vec{d}\times\hat{z})|^3}\right.$$
$$\left. -(1-3Sin^2\alpha)Cos\gamma\frac{yz}{|(\vec{d}\times\hat{z})\times\vec{d}|^3}\right\} \tag{B.2}$$

$$a_{Sail-z_\alpha} = \beta\frac{(1-\mu)}{d^2}Cos\alpha\left\{-3Cos\alpha Sin\alpha\frac{z}{d^2} + (1-3Sin^2\alpha)Cos\gamma\frac{(y^2+(x+\mu)^2)}{|(\vec{d}\times\hat{z})\times\vec{d}|^3}\right\} \tag{B.3}$$

$$a_{Sail-x_\gamma} = \beta\frac{(1-\mu)}{d^2}Cos^2\alpha\left\{Sin\alpha Cos\gamma\frac{y}{|(\vec{d}\times\hat{z})|^3} + Sin\alpha Sin\gamma\frac{(x+\mu)z}{|(\vec{d}\times\hat{z})\times\vec{d}|^3}\right\} \tag{B.4}$$

$$a_{Sail-y_\gamma} = \beta\frac{(1-\mu)}{d^2}Cos^2\alpha\left\{-Sin\alpha Cos\gamma\frac{(x+\mu)}{|(\vec{d}\times\hat{z})|^3} + Sin\alpha Sin\gamma\frac{yz}{|(\vec{d}\times\hat{z})\times\vec{d}|^3}\right\} \tag{B.5}$$

$$a_{Sail-z_\gamma} = \beta\frac{(1-\mu)}{d^2}Cos^2\alpha\left\{-Sin\alpha Sin\gamma\frac{(y^2+(x+\mu)^2)}{|(\vec{d}\times\hat{z})\times\vec{d}|^3}\right\} \tag{B.6}$$

Appendix C: Solar Sail Orientation Angles at Successive Patch Point for Trajectory Shown in Figure 7.4

In Table C.1, the Sail Orientation history is provided for each successive patch point for the periodic trajectory. The trajectory is about an artificial Lagrangian Point, L_1 and is being maintained in an orbit by using corrections algorithm employing solar sail angles for trajectory design. These angles correspond to preliminary analysis. It is assumed that spacecraft orientation can be made to 0.001^0 precision.

Table C.1 Sail Orientation Angle History for Figure 7.4

Arc No.	α	γ
Arc 1	0.042^o	0.006^o
Arc 2	-0.040^o	0.002^o
Arc 3	0.007^o	0.015^o
Arc 4	0.102^o	-0.002^o
Arc 5	-0.005^o	-0.003^o
Arc 6	-0.032^o	0.007^o
Arc 7	0.042^o	0.006^o
Arc 8	-0.040^o	0.002^o
Arc 9	0.008^o	0.015^o
Arc 10	0.103^o	-0.002^o
Arc 11	-0.005^o	-0.003^o
Arc 12	-0.032^o	0.007^o
Arc 13	0.042^o	0.006^o
Arc 14	-0.041^o	0.002^o
Arc 15	0.008^o	0.015^o
Arc 16	0.104^o	-0.002^o
Arc 17	-0.005^o	-0.003^o
Arc 18	-0.032^o	0.007^o